Universität Hamburg
DER FORSCHUNG | DER LEHRE | DER BILDUNG

DESY.

In-operando studies of piezoelectric $HfZrO_2$ film on InAs nanowires

Dissertation
zur Erlangung des Doktorgrades
an der Fakultät für Mathematik, Informatik und Naturwissenschaften
Fachbereich Physik
der Universität Hamburg

Vorgelegt von

Shweta Singh

Hamburg

2024

Gutachter/innen der Dissertation:	Prof. Dr. Andreas Stierle Dr. Ivan Vartaniants
Zusammensetzung der Prüfungskommission:	Prof. Dr. E. Weckert Dr. Ivan Vartaniants Prof. Anders Mikkelsen Prof. Dr. Andreas Stierle Prof. Dr. Daniela Pfannkuche
Vorsitzende/r der Prüfungskommission:	Prof. Dr. Daniela Pfannkuche
Datum der Disputation:	14.10.2024
Vorsitzender des Fach-Promotionsausschusses PHYSIK:	Prof. Dr. Markus Drescher
Leiter des Fachbereichs PHYSIK:	Prof. Dr. Wolfgang J. Parak
Dekan der Fakultät MIN:	Prof. Dr.-Ing. Norbert Ritter

Zusammenfassung

Der Einsatz von Bildgebungsinstrumenten ist für unser Verständnis des Universums von entscheidender Bedeutung. Bildgebende Systeme liefern wichtige wissenschaftliche Daten über alles, von Galaxien und Sternen, die mit riesigen Teleskopen untersucht werden, bis hin zu Mikro- und Nanostrukturen, die mit Mikroskopen untersucht werden. Eine ideale Sonde für die zerstörungsfreie Bildgebung ist die Röntgenstrahlung, wenn das untersuchte Objekt etwa 100 Nanometer groß ist. Im Vergleich zu optischen Abbildungslinsen ist der Prozess der Herstellung von Röntgenabbildungslinsen wesentlich komplexer. Daher wurden „linsenlose“ Methoden entwickelt, die auf den kohärenten Eigenschaften der Strahlung beruhen. Mit der dritten Generation von Synchrotronquellen wurden leistungsstarke und hochkohärente Röntgenstrahlen allgemein verfügbar. Neue bildgebende Verfahren wie die kohärente Röntgendiffraktion (CXDI) nutzen sie.

Die moderne Nanotechnologie eröffnet eine Vielzahl von Anwendungsmöglichkeiten in verschiedenen Bereichen der Physik, Chemie, Biologie und Technik. Im Vergleich zu Massenmaterial im Makromaßstab weist Materie im Nanomaßstab andere physikalische und chemische Eigenschaften auf. Der anhaltende Trend der Halbleiterindustrie zur Reduzierung funktionaler Komponenten stellt neue Probleme für die Wachstums- und Charakterisierungstechniken dar. Diese Arbeit gliedert sich in zwei große Analysen. Ein Teil der Arbeit befasst sich mit der Entdeckung des piezoelektrischen Effekts von Hafnium-Zirkonium-Oxid (HZO) auf einzelnen Halbleiter-Nanodrähten (NWs). Ihre effektiven Dehnungsrelaxationseigenschaften haben in den letzten Jahrzehnten viel Aufmerksamkeit auf sie gelenkt.

Da die Dehnung einen wesentlichen Einfluss auf das Verhalten von NW hat, kann man die durch die angelegten Spannungen induzierte Dehnungswirkung anhand der Veränderungen in den entsprechenden Beugungsmustern sichtbar machen. Darüber hinaus werden im Rahmen dieser Arbeit dreidimensionale Computergestützte Technik (CAE)-Modellierungen und simulationsbasierte Studien mittels COMSOL Multiphysics der mehrschichtigen Probenstruktur durchgeführt, um die ideale Reaktion des piezoelektrischen Materials unter verschiedenen Spannungszyklen für verschiedene physikalische Konfigurationen zu verstehen.

Der zweite Teil zielt auf die Implementierung der Winkel-Röntgen-Kreuzkorrelationsanalyse (AXCCA) zur Bestimmung und zum Verständnis der Mesokristallstrukturen über die

Korrelation zwischen den Intensitäten der experimentell gewonnenen Beugungspeaks an ihren entsprechenden Transfervektoren. Dies ermöglichte uns die Analyse der Winkelanisotropie der untersuchten Strukturen sowie das Verständnis der strukturellen Orientierungsordnung. Die mathematische Validierung der Korrelationspeaks ergab die strukturellen Details, die schließlich mit den tatsächlichen Kristallstrukturen verglichen wurden, was die Anwendung und Genauigkeit dieser AXCCA-Methode bestätigte.

Die Arbeit an diesen beiden Projekten ist Teil meiner Forschung am Forschungszentrum DESY. Die P23- und P10-Strahlrohre des PETRA III-Synchrotrons sowie das NanoMax-Strahlrohr von MAXIV in Lund, Schweden, wurden für experimentelle Studien genutzt.

Abstract

The use of imaging tools is critical to our Comprehension of the Universe. Imaging systems offer vital scientific data on anything from galaxies and stars, examined by massive Telescopes, to micro- and nanostructures, examined by Microscopes. An ideal probe for non-destructive imaging is an X-ray when the object being studied is roughly 100 nanometers in size. Compared to optical image-forming lenses, the process of producing X-ray image-forming lenses is far more complex. As a result, "lensless" methods that depend on radiation's coherent qualities were created. The third generation of synchrotron sources made powerful and highly coherent X-ray beams widely available. New imaging techniques like coherent X-ray diffractive imaging (CXDI) employ them.

A vast range of potential applications in several fields of physics, chemistry, biology, and engineering are made conceivable by modern nanotechnology. Compared to bulk material at the macroscale, matter exhibits distinct physical and chemical characteristics at the nanoscale. The semiconductor industry's ongoing trend of functional component reduction presents new growth and characterization technique problems. This thesis is divided into two broad analyses. One part of the thesis focused on revealing the piezoelectric effect of Hafnium Zirconium Oxide (HZO) on single semiconductor nanowires (NWs). Their effective strain relaxation qualities have drawn a lot of attention to them over the past few decades.

Furthermore, since strain has a substantial impact on NW response, one can visualize the induced strain effect from the applied voltages via the changes in the corresponding diffraction patterns. Moreover, 3-dimensional Computer-aided engineering (CAE) modeling and simulation-based studies via COMSOL Multiphysics of the multi-layer sample structure are performed as a part of the thesis in order to understand the ideal response of the piezoelectric material under different voltage cycles for various physical configurations.

The second part targets the implementation of the Angular X-ray Cross Correlation Analysis (AXCCA) for the determination and understanding of the mesocrystal structures via the correlation between the intensities of the experimentally retrieved diffraction peaks at their corresponding transfer vectors. This allowed us to analyze the angular anisotropy of the structures under investigation along with the understanding of structural orientation order. The mathematical validation of the

correlation peaks revealed the structural details, which were finally compared with the actual crystal structures, confirming the application and accuracy of this AXCCA method.

The work is conducted on these two projects as a part of my research at the DESY research center. The PETRA III synchrotron's P23 and P10 beamlines as well as MAXIV's NanoMax beamline in Lund, Sweden, were used for conducting experimental studies.

Declaration of Oath

I hereby declare and affirm that this doctoral dissertation is my own work and that I have not used any aids and sources other than those indicated.

If electronic resources based on generative artificial intelligence (gAI) were used in the course of writing this dissertation, I confirm that my own work was the main and value-adding contribution and that complete documentation of all resources used is available in accordance with good scientific practice. I am responsible for any erroneous or distorted content, incorrect references, violations of data protection and copyright law or plagiarism that may have been generated by the gAI.

14.10.2024 , Shweta Singh

Contents

1 Introduction **1**

2 X-rays and Synchrotron Sources **6**

2.1 Historical Perspective 6
2.2 Conventional X-ray tube 8
2.3 Synchrotron sources 12
2.3.1 Facilities for first-generation storage rings 12
2.3.2 Storage rings of the second generation. Sources of synchrotron radiation specifically 14
2.3.3 Facilities for third-generation storage rings 16
2.3.4 Facilities of the fourth generation 19
2.4 Free-electron lasers for X-rays 23
2.4.1 The XFEL machine's fundamental idea 24

3 X-Ray Matter Interaction **31**

3.1 One electron 31
3.2 One atom 34
3.3 One molecule 36
3.4 X-ray diffraction by crystals: a kinetic hypothesis 37
3.5 Principles of X-ray Diffraction: 42
3.6 X-rays through a material 44

4 Semiconductor nanowires **48**

4.1 Introduction 48
4.2 Development of nanowires (NW) 50
4.2.1 Growth of MBE using Au-catalyst 51
4.2.2 Growth of catalyst-free MOVPE 52
4.2.3 Crystal composition of NW's 53
4.2.4 Measurements of strain in NW's 53

5 A Synopsis of Piezoelectric Technology 56
5.1 Introduction . . . 56
5.2 A quick overview of history: Piezoelectricity . . . 57
5.3 Piezoelectric effect . . . 59
5.3.1 Direct and Indirect impacts . . . 59
5.3.2 Contribution of Ferroelectric Properties to Piezoelectricity. . . . 61
5.3.3 Piezoelectric Studies of $HfZrO_2$ in Nanostructured Devices . 65
5.3.4 Finite Element Method (FEM) . . . 67

6 Experimental Results 71
6.1 Overwiew . . . 71
6.2 Experimental studies at NanoMax . . . 73
6.3 Experimental studies at PETRA III . . . 76
6.4 Sample Design and Modeling . . . 81
6.5 Analysis 1: 4 layer sample structure with only applied voltage . . . 85
6.6 Analysis 2: 4 layer sample structure with applied voltage and misfit strain . . . 88
6.7 Analysis 3: NW sample structure with applied voltage only . . . 90
6.7.1 Analysis 4: NW sample structure with applied voltage and Misfit Strain . . . 92
6.8 Conclusion . . . 96

7 Angular X-ray cross-correlation analysis (AXCCA) 97
7.1 Basics of AXCCA . . . 97
7.2 Analysis of structural parameters of Au mesocrystals using angular X-ray cross-correlation analysis . . . 104
7.2.1 Sample and Experimentation . . . 104
7.2.2 Analytical methodology . . . 106

8 Appendix 112
8.1 Piezoelectric Supplementary Relations . . . 112

9 Conclusions and outlook 115

1 Introduction

Condensed matter

The beginning of the serious study of solid-state physics was marked by the discovery of X-ray diffraction by crystals and the publication of several basic calculations of crystal characteristics and electron properties in crystals [1]. Building on this foundational knowledge, solid-state physics has emerged as a field that largely focuses on the characteristics of solids, especially at the atomic and molecular levels. As a vital component within condensed matter physics, this field examines the physical characteristics of condensed phases of matter and is thus considered an essential subject of research [2]. In solid-state physics, the primary focus is on how atoms and molecules behave when in close proximity to one another. This line of study extends to understanding how an object's atomic-scale characteristics influence its larger-scale properties [3]. Key to these investigations is the understanding of lattice patterns, symmetry, and crystal defects, which are integral to the arrangement of atoms in crystalline solids [4]. Additionally, solid-state physics involves the analysis of the electronic structure of solids. This analysis is crucial for explaining how charges are propagated within metals, semiconductors, and insulators, dealing with complex concepts like electronic states, band gaps, and energy bands. This field also encompasses the investigation of lattice dynamics, which includes thermal conductivity, heat capacity, and phonons—quantized modes of lattice vibrations [5].

Magnetism and piezoelectricity

In parallel, the examination of magnetism in materials forms a significant part of solid-state physics, covering aspects such as ferromagnetism, antiferromagnetic, and superparamagnetic properties [6, 7]. The field also delves into the investigation of materials exhibiting superconductivity, where materials demonstrate zero electrical resistance and the expulsion of magnetic fields when cooled below a certain critical

temperature. Complementing these studies is the examination of how materials interact with electromagnetic radiation, a field that includes phenomena such as absorption, reflection, and photoluminescence [7]. Furthermore, solid-state physics explores the physics of substances and structures at the nanoscale, where the influence of quantum mechanics becomes notably evident [7]. This exploration is pivotal for the creation of novel materials and technologies, with applications spanning semiconductors, solar cells, and magnetic storage media, all rooted in the principles of solid-state physics [1].

Solid-state physics

The fields of materials science, chemistry, electrical engineering, and nanotechnology are all included in the realm of solid-state physics. This interconnection allows the concepts of this to be applied across a wide spectrum of technical advancements and real-world challenges, ranging from the development of renewable energy technologies to the intricacies of electronic gadgets [8]. At the heart of solid-state physics lie a few fundamental physical concepts that are crucial for a deep understanding of the field. These concepts include lattice vibrations, electronic band theory, and crystal formations. In the world of crystals, atoms are arranged in a highly ordered, repeating pattern known as a crystal lattice. This lattice structure is characterized by different geometries and symmetries, leading to various lattice types such as cubic, tetragonal, orthorhombic, hexagonal, and trigonal, which are among the most common. The unit cell, the smallest repeating unit in a crystal lattice, plays a vital role in defining the overall symmetry and structure of the crystal. However, real crystals are not perfect and often contain defects such as dislocations, interstitials, and vacancies, which significantly impact the physical properties of the materials [9]. It is essential to investigate at the atomic level to understand their structural arrangement, analyze their lattice structure, study the deformations at the atomic scale, and investigate their anisotropic nature. X-ray-based non-destructive techniques allowed us to perform such analysis across different sample types with precision and accuracy. Observing changes across the diffraction patterns due to the variations in the properties/structure of these crystals is an efficient method for in-depth investigation.

In the realm of this, electron energy levels in solids are spread out into bands. These energy bands are pivotal in determining the electrical properties of a material.

The conduction band, being the lowest unoccupied energy band, and the valence band, the highest occupied energy band, play key roles in influencing a material's electrical conductivity. The nature of these bands, and particularly the energy gap between them known as the band gap, dictates whether a material behaves as an insulator, a conductor, or a semiconductor. In metals, the bands overlap, while in semiconductors, the band gaps are relatively small, and in insulators, these gaps are significantly larger [5]. The electrical properties of semiconductors can be notably altered by doping, which introduces impurities that create new energy levels within the band gap [9]. Further delving into the intricacies of solid-state, lattice vibrations within solids are quantified as phonons. These phonons, conceptualized as quasi-particles, represent collective excitations within the atomic lattice and are central to understanding many thermal properties of solids. They significantly contribute to the heat capacity of materials, and the study of this aspect at low temperatures has been foundational in developing the quantum theory of solids. The thermal conductivity of a material is also greatly influenced by these lattice vibrations. In most semiconductors and insulators, phonons act as the primary carriers of heat. However, as temperatures increase, the simple harmonic approximation of lattice vibrations becomes inadequate, leading to more complex anharmonic phenomena such as thermal expansion [10].

Thesis outline

This present thesis is divided into two broad aspects. The chapters are also presented in accordance with the research areas. The first research segment focuses on piezoelectric properties and the induced strain response from the applied voltage cycles, while the second research segment focuses on the analysis of the crystal structure using the Angular X-ray Cross-Correlation Analysis (AXCCA) technique. The thesis begins with an introductory chapter that sets the stage for the subsequent discussions. It provides a broad overview of the study's objectives and significance, laying the groundwork for a thorough examination of various scientific phenomena. Chapter 2, 'X-rays and Synchrotron Sources' delves into the topic of X-rays and their sources. Beginning with a historical overview, it follows the evolution of X-ray technology, from traditional X-ray tubes to advanced synchrotron sources. The discussion covers the evolution of synchrotron facilities through various generations, highlighting their distinct capabilities and contributions to scientific research. It also delves into the fundamental principles of free-electron lasers for X-rays, shed-

ding light on the innovative concepts that drive their functionality. A significant portion of the thesis is devoted to investigating the complex interactions of X-rays and matter, which is covered in Chapter 3, 'X-Ray Matter Interaction'. It starts by elucidating the interactions between individual electrons before progressing to more complex systems involving atoms and molecules. The chapter also looks at phenomena like X-ray diffraction by crystals and the fundamental principles that govern X-ray diffraction processes. It also studies the behavior of X-rays as they pass through different materials, providing insights into their interaction mechanisms. Transitioning to semiconductor nanowires, the thesis delves into their development and growth methods in Chapter 4,' Semiconductor nanowires'. An in-depth discussion of semiconductor nanowire growth and fabrication processes is provided in this chapter, which dives into the complexities of these materials. This chapter offers insights into nanowire crystal composition, ranging from the use of catalysts such as Au in Molecular Beam Epitaxy (MBE) to the novel catalyst-free Metalorganic Vapor Phase Epitaxy (MOVPE). It also carefully looks at methods used to detect strain in these nanostructures, providing insight into the dynamic relationship between structure and function in semiconductor materials. As we go on to Chapter 5, the focus shifts to piezoelectric technology and its historical development and underlying theories. A thorough introduction to the piezoelectric effect is provided in this chapter, with a distinction made between its direct and indirect effects. Moreover, it investigates the complex roles that ferroelectric characteristics play in piezoelectricity, going into detail in particular research that sheds light on its uses in nanostructured devices. The final section of the chapter delves into more sophisticated techniques like the Finite Element Method (FEM), adding to the discussion of computational methods in piezoelectric research, which is later adopted in the thesis. In Chapter 6, conducted studies and their outcomes are thoroughly described, drawing readers into the experimental results. This chapter provides a comprehensive view of the research process, covering everything from sample design and modeling to experimental methods at the NanoMax beamline at MAXIV and PETRA III. Conclusions are obtained by carefully synthesizing a variety of simulations and evaluations on sample structures with applied voltage and misfit strain to nanowire samples under comparable conditions using COMSOL Multiphysics. By combining simulation frameworks, the chapter promotes a deeper comprehension of the sample investigations that are the subject of the study. Chapter 7 includes with a discussion of Angular X-ray Cross-Correlation Analysis (AXCCA), including its theoretical foundations and its experimental utilization for the analysis of meso-crystal structures. This section provides information about the experimental setups, methods, and lattice structure of

the analyzed samples. It also provides insight into the analytical approaches used in structural characterization along with the mathematical modeling so as to determine the structural parameters of the samples. The chapter improves our knowledge of material properties at the nanoscale by examining the structural parameters of materials using AXCCA, opening the door for developments in a variety of scientific fields. The 'appendix' contains supplemental material that enhances the primary discussion by providing further context and perspectives for the research that is discussed throughout the thesis. These chapters work together to create a continuous understanding that deepens our comprehension of a range of scientific phenomena and how they may affect current and upcoming studies as well as technological advancement.

2 X-rays and Synchrotron Sources

2.1 Historical Perspective

This chapter is adapted from [11]. From the naked eye, it is impossible to locate the position of the atoms in the unit cell of the crystals. However, it is crucial to determine the structure of the crystals and their lattice parameters to dictate what kind of property the material is going to have. Therefore, we need some kind of agent that can pass through the crystal and give critical structural information from within the crystal. One can fulfill this requirement by using X-rays as the potential agent to penetrate through the sample. The X-rays were discovered by German physicist W.C. Röntgen in 1895. He discovered a novel type of rays, bearing striking similarities to conventional light, particularly in electromagnetic radiations. However, there are some essential differences between X-rays and ordinary light. X-rays are much more penetrating than ordinary light and these X-ray waves are much shorter wavelengths than the light rays. [11]

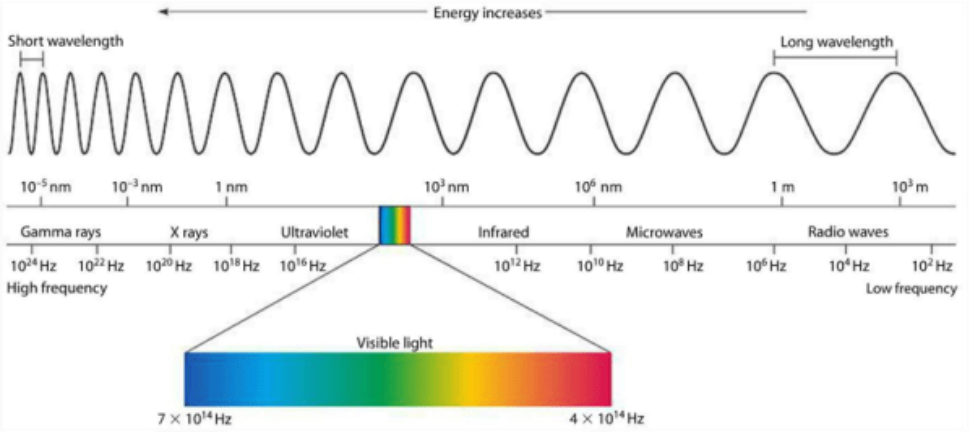

Figure 2.1: The electromagnetic spectrum. Adapted from [12]

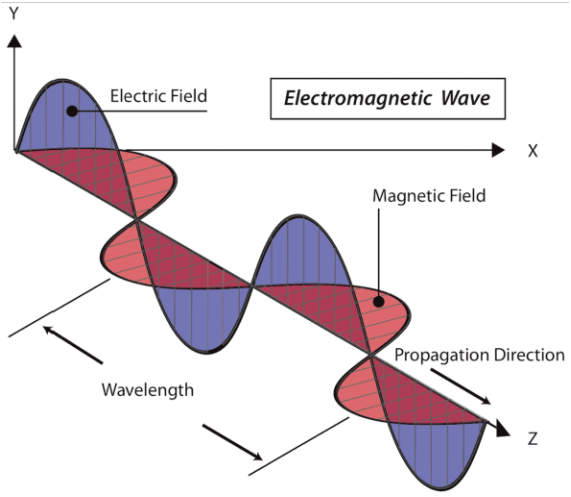

Figure 2.2: An electromagnetic wave consisting of electric and magnetic oscillating fields. Adapted from [13]

Figure 2.1 highlights the electromagnetic spectrum, which shows the possible types of radiations along with their wavelength values. Normally, the wavelength of the X-rays we use in the study of the crystals is about 0.5 to 2.5 Å. On the other hand, the wavelength of visible light is about 6000 Å. Consequently, due to their significantly greater penetrative ability compared to visible light, X-rays have become an essential tool for studying the structure of crystals.

X-rays are electromagnetic waves, which means they are associated with both electrical and magnetic fields. For instance, if the direction of propagation of X-rays is in the x-direction, then in the y-direction we can have the electric field component, and the magnetic field would then be associated along the z-direction. In the study of crystal structures using X-rays, the primary interest lies in how the electric component of the electromagnetic waves interacts with the electrons in the crystal lattice. In an assumed X-ray wave propagating along the x-direction, the electric and magnetic fields are oriented perpendicular to each other within the yz-plane. For the wave to be considered unpolarized, the electric field's orientation could vary randomly within this plane. However, if the electric field consistently lies within a specific direction in the yz-plane, the wave is described as polarized. [14]

2.2 Conventional X-ray tube

Reliability of the X-ray tube Röntgen utilized was a challenging task. Thus, when W.D. Coolidge of the General Electric Research Laboratories in New York created a new tube in 1912 that generated electrons from a burning filament and then accelerated them toward a metal anode that was cooled by water, it was a huge practical advancement (see Fig. 2.3). Now, the high voltage and the current could be adjusted separately, and the cooling efficiency was the sole factor limiting the intensity. It turns out that this kind of equipment has a maximum output of about 1 kW. While there were only minor technological advancements, the Coolidge tube remained the industry standard for X-ray tubes for many years. It was discovered early, that heat could be dispersed over a much larger volume by spinning the anode than in a standard tube, increasing the total power accordingly, but it wasn't until the 1960s that so-called rotating anode generators were made commercially available. The challenge of creating a high-vacuum seal on the spinning shaft—which requires the cooling water to go in and out—was one of the technical obstacles to be solved. [15]

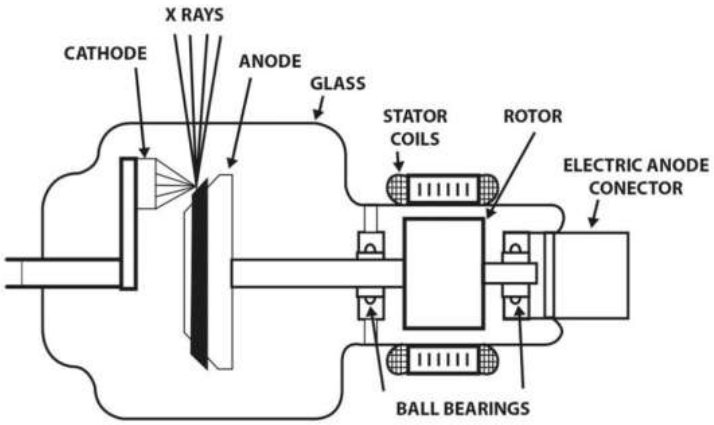

Figure 2.3: Major components of an X-ray tube assembly. Adapted with changes from [16]

Two separate components make up the X-ray spectrum produced when electrons impinge on a metal anode. Since the electrons in the metal are slowing down and finally stopping, there is a continuous portion. As a result, this radiation is called bremsstrahlung radiation (from the German word bremsen, which means brake), and the high voltage that is given to the tube determines its maximum energy. A brittle line spectrum is superimposed on this enormous spectrum. A vacancy can

also be created in an atom by the incident electron removing an atomic electron from one of the inner shells during a collision. The energy differential between the two shells may be represented by an X-ray that is created when an electron relaxes from an outer shell into the void. This radiation is fluorescent. When doing studies that need a monochromatic beam, the Kα line—which is many orders of magnitude more intense than the bremsstrahlung spectrum—is frequently used (refer to Fig. 2.4). Only a very tiny portion of the photons released into the solid angle of 4π, however, may be used in a beam that needs a few squared milliradians of angular divergence. Furthermore, because the line source cannot be constantly tuned, it is not possible to select or scan the ideal wavelength for the experiment. As we will see in the upcoming sections, X-rays produced by synchrotron sources are far more brilliant than those from the conventional laboratory sources and do not have these disadvantages [17].

X-rays are normally produced by allowing a beam of highly energetic electrons to strike a metal target. In the synchrotron, electrons are accelerated to almost the speed of light and their kinetic energy is converted into electromagnetic radiation to create X-rays. The general steps in the procedure are as follows:

- Electrons are given high energy and speed when they are accelerated in a linear accelerator, also known as linac.
- The synchrotron ring is where the accelerated electrons are then introduced and retained on a circular path by the use of induced magnetic fields.
- The magnets known as wigglers or undulators that the electrons pass through as they round the ring distort their trajectory and push them to proceed in a nearly sinusoidal fashion.
- As the electrons are bent along their path by these magnetic fields, they emit synchrotron radiation, which is a broad spectrum of electromagnetic radiation that indeed includes X-rays.
- The X-ray radiation generated is then filtered and collimated to produce a high-intensity, high-quality beam.

Overall, the synchrotron is an effective instrument for producing X-rays with great control and accuracy, allowing researchers to examine the atomic and molecular structure of matter in unprecedented depth. Additionally, due to the impact of

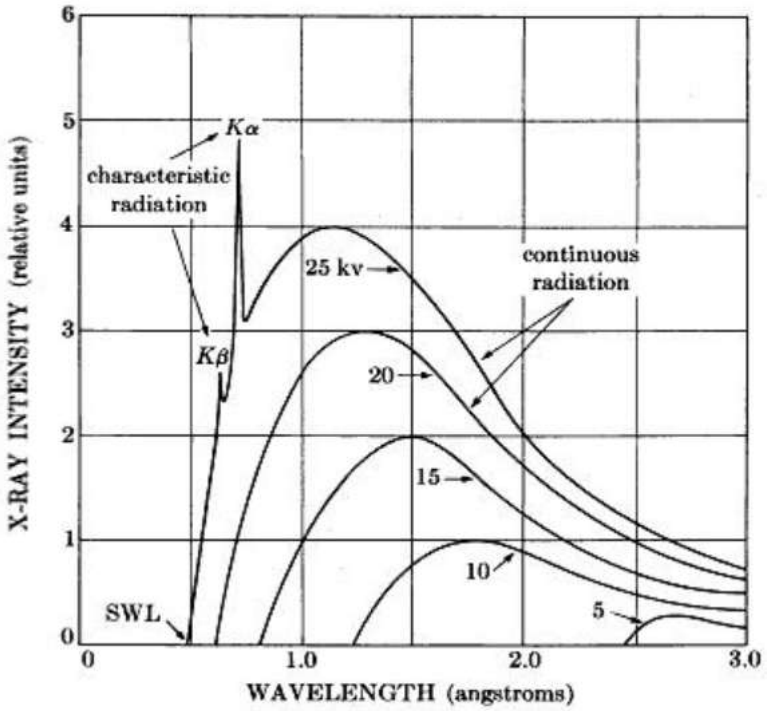

Figure 2.4: A general representation of X-ray intensity vs wavelength plot, to highlight the characteristic intensity peaks. Adapted with changes from [18]

the electrons on the target, the same can undergo a considerable level of heating. Therefore, it must be kept cool down to avoid the melting of the material by passing liquid nitrogen through the target. The recently developed synchrotron sources are designed to deliver X-rays with high quality properties, often characterized by high brightness, small angular divergence and small source size. One can quantify the quality of X-ray by the commonly used quantity 'brilliance', which is mathematically given as

$$brilliance = \frac{(photons/second)}{((solid\ \ angle(m\,rad^2)))(source\ \ area(mm^2))(0.1\%\ \ bandwidth))} \tag{2.1}$$

Quantitatively, the higher the brilliance of the beam, the greater the number of photons one has for imaging. In an X-ray intensity vs. wavelength plot, white radiation appears as a continuous distribution of intensities across a broad range of wavelengths. This is in contrast to the characteristic X-ray radiation produced when the electrons in an atom are excited and then release energy in the form of X-rays with specific wavelengths. The characteristic X-ray radiation appears as sharp

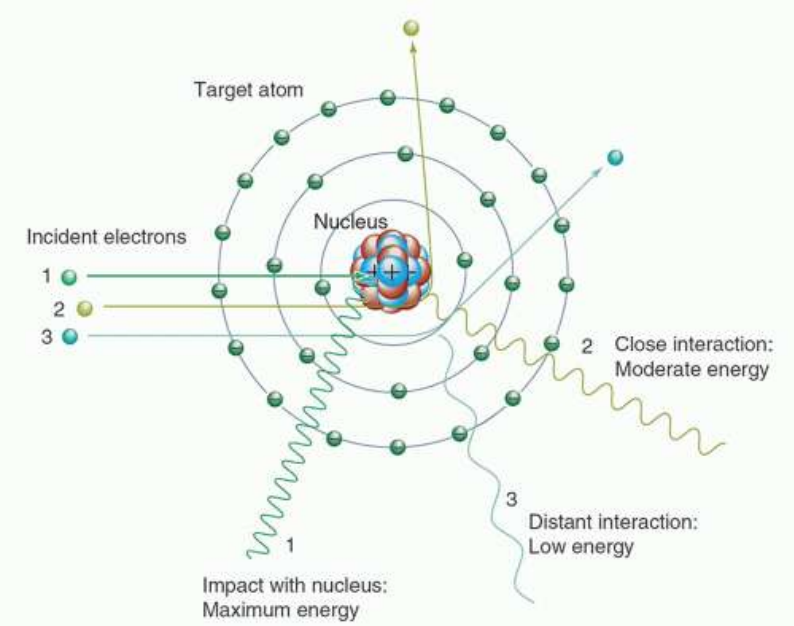

Figure 2.5: Energetic electron interactions with the target material's atomic nucleus produce bremsstrahlung radiation. Adapted from [19]

lines or peaks in the intensity vs. wavelength plot. It is characteristic of the target that has been used for the experiment. Therefore, characteristic radiations change according to the target. It is different for different target materials. In Fig.2.4, a short, sharp peak is called the Kβ wavelength, and the high-intensity peak is known as the Kα wavelength. The kα line represents the transition of an electron from the second-lowest energy shell (L shell) to the lowest energy shell (K shell), while the Kβ line represents a transition from a higher energy shell (typically the M shell) to the K shell. [20]

The short wavelength limit (SWL) in X-ray intensity vs. wavelength is determined by the characteristic energy of the X-ray photons being emitted. X-rays with shorter wavelengths have higher energies and, correspondingly, higher frequencies. The shortest-wavelength X-rays that can be produced are typically generated by highly energetic processes such as nuclear transitions or interactions between high-energy particles and matter. These X-rays have energies in the range of several kilo electron volts (keV) to several mega electron volts (MeV). The specific short wavelength limit in X-ray intensity vs. wavelength depends on the particular X-ray source and the experimental conditions used to generate and detect the X-rays. In general, X-ray wavelengths shorter than about 0.1 nanometers (nm) are considered to be in the "hard X-ray", while X-rays with longer wavelengths are considered to be the "soft

X-rays".

2.3 Synchrotron sources

2.3.1 Facilities for first-generation storage rings

This chapter is adapted from [21]. At present, the principal sources of intense X-ray radiation are the storage rings. The synchrotron's X-rays are not only very brilliant, but also extremely stable in terms of energy, intensity, size, and beam location. Photon energy ranges across a broad range, from infrared to hard X-rays. Beams from storage rings are typically linearly polarized in the ring plane, while elliptically polarized beams can also be produced by including additional devices. [22]

In the 1940s, synchrotron radiation was initially detected as a parasitic radiation in particle accelerators intended for high-energy physics investigations. The observation was conducted in three distinct research laboratories: Cornell Electron Synchrotron, USA; Lebedev Institute, Russia; and General Electric Research Laboratory, USA. Bending magnets (Fig. 2.6) were used in these studies to retain the particles in the accelerating ring and control their trajectory. The energy of the particle E_γ in the storage ring is one of the many variables that affect the parameters of synchrotron radiation

$$E\gamma = \gamma mc^2, \tag{2.2}$$

where γ is the Lorentz factor and mc^2 is the particle's rest mass energy

$$\gamma = \frac{1}{\sqrt{1-(\frac{v}{c})^2}} = \frac{1}{\sqrt{1-{\beta_v}^2}}, \tag{2.3}$$

where $\beta_v = v/c$, v is the particle speed, and c is the vacuum speed of light.

Up to 1 GeV, the first accelerators, which appeared in the 1930s, kept the beam energy relatively modest. Over the course of the following three decades, the particle beam energy threshold was raised to 100 GeV.

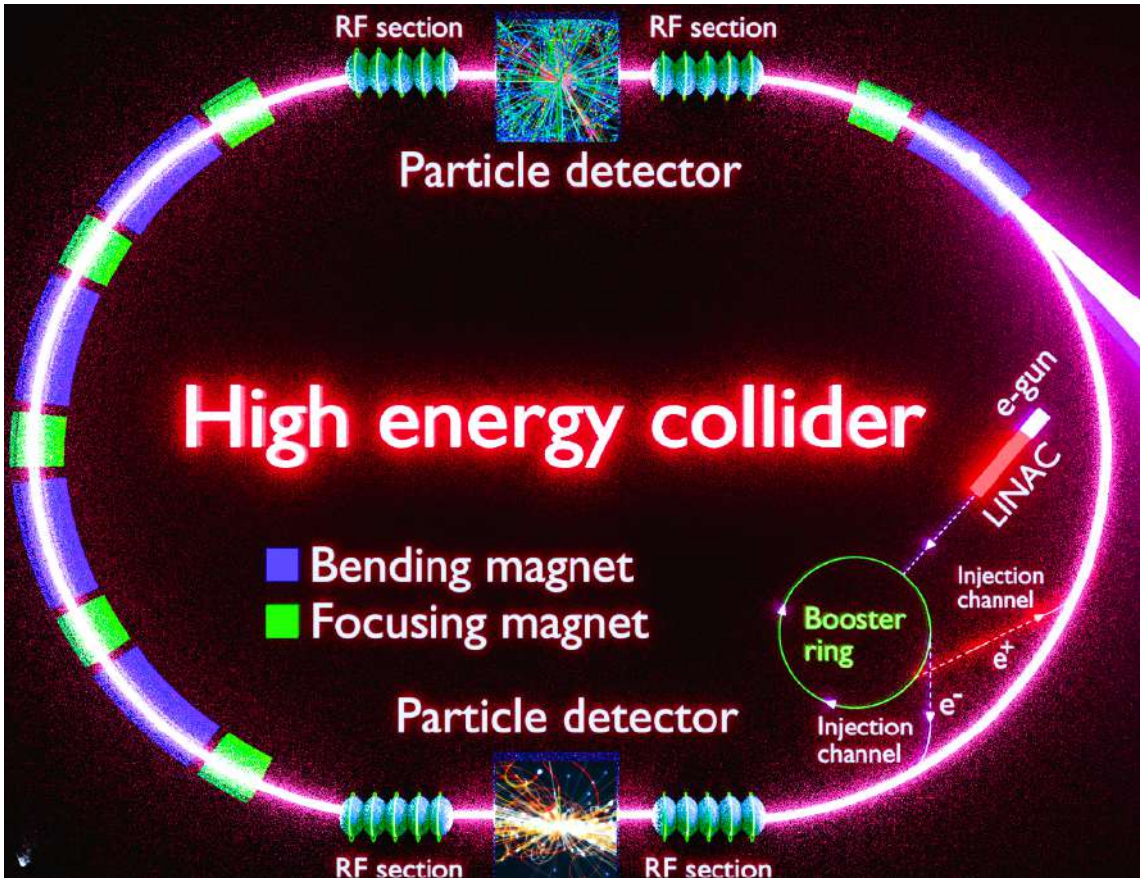

Figure 2.6: High energy collider schematic view. Adapted with changes from [21]

The Large Hadron Collider (LHC) is one of the modern particle colliders that can sustain electron beam energies up to enormous energies of 6.5 TeV and collision energies of 13.6 TeV. Nevertheless, synchrotron accelerators, which run in typical regimes with electron beam energies up to 8 GeV, are devoted to the study of condensed matter, biology, and chemistry. Since the average Lorentz factor in this instance is seen at synchrotron accelerators and falls between $2 \cdot 10^3 < \gamma < 16 \cdot 10^3$, the electron beam is regarded as ultra-relativistic. When relativistic particles accelerate or are periodically accelerated in a magnetic field, synchrotron radiation is produced [23]. Particles at synchrotron accelerators lose energy and release electromagnetic waves as a result of centripetal acceleration. Radiation is released in a narrow cone perpendicular to the particle's path if it is traveling at relativistic speeds $\theta \propto \frac{1}{\gamma}$.

The experiments may make use of this synchrotron radiation, which is already generated in a particle accelerator [24, 25]. The creation of the first-generation facilities was the next significant advancement, even if the number of synchrotrons was increasing. The invention specifically affected the electron storage ring, the foundation of all synchrotron sources in use nowadays (refer to Fig. 2.13).

2.3.2 Storage rings of the second generation. Sources of synchrotron radiation specifically

The second-generation facilities are synchrotron radiation sources that are specifically designed to maintain the viability of the particles and produce a stable X-ray radiation beam. These facilities consist of several main components, including an electron gun, LINAC (linear accelerator), a booster ring, a storage ring, a radio frequency section, bending magnets, and beamlines [26].

The source of electrons, which are often produced by thermionic emission from a hot filament, is the electron gun. Since an electron supply must be consistent, the electron gun operates in a continuous regime. A linear accelerator (LINAC) is used to accelerate the electrons to around 100 MeV. It is possible for electrons to be lost in the machine as a result of collisions with gas particles in the storage ring that are still there after creating a vacuum. Following its acquisition, the electron current is sent from the LINAC to a booster ring in order to accelerate it even more (Fig. 2.7). The electrons in the primary storage can continue to accelerate until they reach the

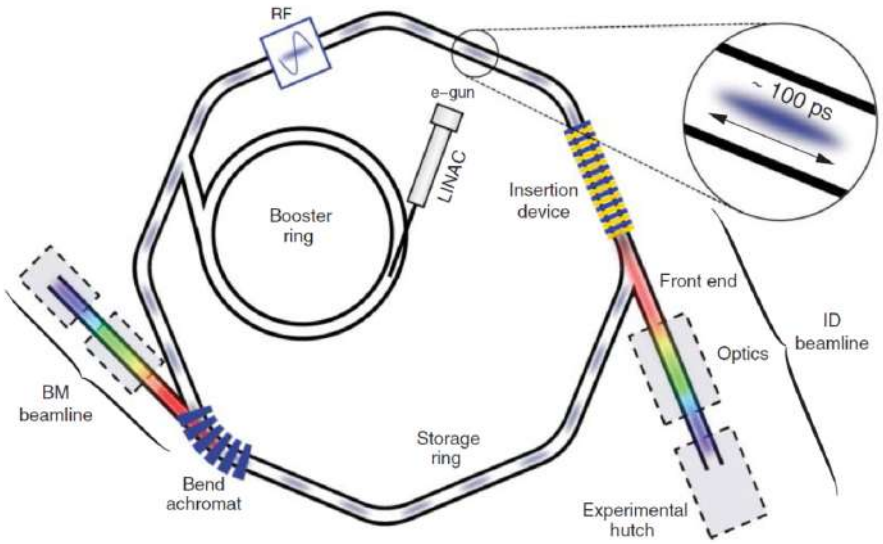

Figure 2.7: A schematic depiction of the storage ring showing the location of the accelerator, the radio frequency (RF) system, the insertion device (ID), the beamline, and the bending magnet (BM) [27].

required energy. To maintain the designated storage ring current, the booster ring occasionally injects itself into the storage ring.

The majority of synchrotron sources are storage rings, as shown in Fig. 2.7, where particles produce X-ray beams each time they pass through sections equipped with magnetic devices. The identical electron bunches are used by several experimental sites, spread out throughout the synchrotron ring. Radiofrequency (RF) accelerators control the spacing between the electronic bunches. Furthermore, the electron energy used for synchrotron radiation is recovered using RF accelerators. The time interval between consecutive X-ray pulses in RF accelerators can be as short as 1 ns due to the frequency of field oscillations, which ranges from several MHz to 1 GHz.

An array of magnets [27] along the ring provides the electrons with a confined channel and a stable trajectory. Commonly used magnet types include quadrupole magnets (which focus the electron beam and compensate for Coulomb repulsion between the electrons), bending magnets (which cause the electrons to change their path and eventually maintain a circular orbit), and sextupole magnets (which correct for chromatic aberrations that arise from the focusing by the quadrupoles). Second-generation facilities frequently included bending magnets, which resulted in a curved electron beam trajectory and a wide radiation cone surrounding the bend.

Nevertheless, if the electrons deviate from the optimal reference orbit, dipole-bending magnets by themselves (Fig.2.7) are unable to keep the electrons in a closed orbit. Since then, the optimum orbit has been returned by concentrating a pair of vertical and horizontal quadrupole magnets. The magnetic lattice is the configuration of many types of magnets.

The synchrotron facility's primary elements are being completed by the beamline. The beamline's beam-defining apertures are positioned at the start to determine the angular acceptance of the synchrotron radiation. In this way, radiation removes the synchrotron radiation spectrum's low-energy tail, which is highly absorbed by matter and potentially harmful to optical components.

Before the beam is made available to researchers at the experimental hutch, it is first monochromatized (if needed) and focused in the optics hutch. Electron bunch energy was maintained between 0.7 and 5 GeV in second-generation facilities. Specialized synchrotron facilities include the following: Photon Factory at the KEK (Ko Energy-kasokuki Kenkyukiko) laboratory, Japan; BESSY (Berlin Electron Storage Ring Society for Synchrotron Radiation); Stanford Synchrotron Radiation Laboratory at SLAC (Stanford Linear Accelerator Center), USA; National Synchrotron Light Source at the Brookhaven National Laboratory, USA; Tantalus, University of Wisconsin-Madison, USA; and HASYLAB (Hamburger Synchrotronstrahlungslabor) at DESY, Germany. By creating specialized synchrotron sources, brilliance might be raised to 10^{15}.

2.3.3 Facilities for third-generation storage rings

The next stage of the modernization process for third-generation synchrotron facilities focused on improving the brightness and coherence of the source. The following facilities are examples of third-generation storage rings: APS (Advanced Photon Source) in Chicago, USA; ESRF (European Synchrotron Radiation Facility) in Grenoble, France; SPRING-8 in Japan; and PETRA III in Hamburg, Germany. The photon beam's coherent properties and brilliance were significantly enhanced with the addition of specialized equipment, including wigglers and undulators. The production of wiggler radiation occurs when a magnetic structure is periodically positioned in a high magnetic field. The particle travels through the structure at this kind of radiation source, experiencing a harmonic oscillation with a high oscillation

amplitude and, thus, a wider spectrum. Due to the wider radiation cone, even if one acquires more power from such a source, the brilliance will be reduced. Fig. 2.8 also illustrates the production of undulator radiation in the case of a magnetic field. Because of the reduced magnetic field near this kind of radiation source, the particle undergoes a harmonic oscillation with a small undulation amplitude. The radiation cone will be substantially smaller in this instance. By adding such a structure to the electron storage ring, higher intensity and tiny angular divergence synchrotron radiation might be produced.

The brightness of third-generation synchrotrons, which generally depend on undulators, may reach up to 10^{21}. Additionally, the X-ray radiation's coherence qualities are enhanced. Only 1% of the beam, meanwhile, is coherent enough to be applied in coherence-based applications. Therefore, in order to fully benefit from the X-ray beam without the need for extensive spatial radiation filtering, sources with a greater degree of coherence are urgently required [28].

Undulator radiation

Figure 2.8: Radiation from insertion device: an undulator.

This chapter is adapted from [15]. Using a synchrotron to create X-ray beams is far more effective than having the electrons circle in a strictly circular arc. A standard storage ring is composed of straight portions that are separated by circular arc segments. A mechanism that compels an electron to oscillate in the horizontal plane as it moves through any one of these straight portions can be set up. To achieve this, a series of magnets form an array that alternates from top to bottom in a field. An insertion device can be built so that the radiation from one oscillation's electrons is in phase with the radiation from the subsequent oscillations. This suggests that in order to calculate the intensity, the radiated wave amplitudes are added first, and the total is then squared. An undulator is an insertion device that functions in this manner; Fig. 2.8 shows a schematic of one such device.

The execution of small angular oscillations on a scale determined by $1/\gamma$ by electrons passing an undulator is a prerequisite for the coherent addition of amplitudes. Because an undulator has a finite number of periods, the coherent addition of amplitudes implies a quasi-monochromatic spectrum (with harmonics). The variations in the maximum angles of the electron oscillations in the horizontal plane—K is around 20 for a wiggler and 1 for an undulator—cause variations in these devices' performances. As a result, the radiation cone of an undulator is compressed with respect to the natural opening angle of synchrotron radiation, $1/\gamma$, by a factor of around $1/\sqrt{N}$, where N is the number of periods, usually in the range of 100.

The undulator parameters

The undulator spatial period, λ_u, and γ are the fundamental parameters for undulator radiation. Furthermore, a means of characterizing the oscillations' amplitude is required. The maximum angular divergence from the undulator axis turns out to be more convenient to utilize, though the amplitude itself could be the cause. This maximum angle is equal to the natural opening angle for synchrotron radiation, 1γ, times a dimensionless number, of order unity, represented by the symbol K. Therefore, to characterize the undulator, we will also utilize the parameter K created in this manner, in addition to λ_u, and γ. In terms of the maximal magnetic field B_0 in the undulator, K is easily found as follows:

$$K = \frac{eB_0}{mck_u} \tag{2.4}$$

where $k_u = \frac{2 \cdot \pi}{\lambda_u}$

The fundamental wavelength, λ_1

Here we now construct an equation for the fundamental wavelength λ_1 in the undulator spectrum. Determining the relationship between λ_1 and the undulator period λ_u is a simple one.

Point A is where the electron is at emitter time $t' = 0$. At $t' = T'$, the electron is one undulation downstream. Then, the signal from A is at location cT', and $cT' - \lambda_u$ must be one wavelength λ_1 (or a multiple of that) in order to be coherent. $T' = S\lambda_u/v$ or $cT' = (S/\beta_e)\lambda_u$ is the result of the electron path length between A

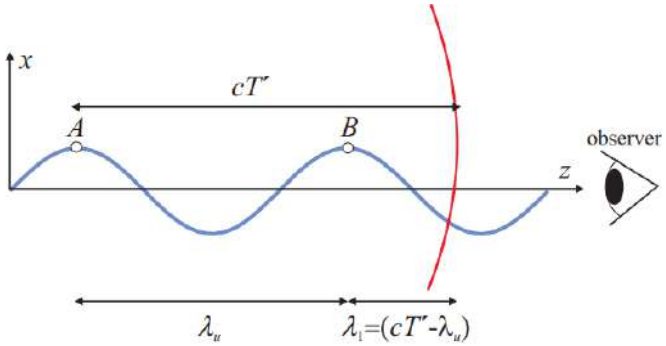

Figure 2.9: When the wavefront that the electron emits at A is one wavelength λ1 ahead of the wavefront that the electron emits at B, constructive interference takes place. Thus, this is the basic wavelength that the undulator emits. Adapted with changes from [17]

and B being a factor S greater than the period λ_u.

$$\lambda_1(\theta = 0) = \lambda_u(\frac{S}{\beta_e} - 1) = \frac{\lambda_u}{2\gamma^2}(1 + \frac{K^2}{2}) \tag{2.5}$$

where $S = \frac{1+\gamma^{-2}K^2}{4}$

$$\lambda_1(\theta = 0) = \lambda_u(\frac{S}{\beta_e} - cos\theta) = \frac{\lambda_u}{2\gamma^2}(1 + \frac{K^2}{2} + \gamma\theta^2) \tag{2.6}$$

It's also crucial to remember that the first-order wavelength λ_1, which is radiated, may be tuned by modifying the magnetic field through adjustments to the space between the poles.

2.3.4 Facilities of the fourth generation

These days, fourth-generation facilities are built, with several straight sections that are specifically designed to create high-brilliance undulator radiation (see examples in Fig. 2.10).

The next generation of X-ray storage rings can have two to three orders of magnitude higher brightness thanks to a novel conceptual approach, which is the construction of a multi-bend achromat lattice of the synchrotron storage ring (see in Fig. 2.11) [30, 31].

Figure 2.10: Synchrotron sources of the fourth generation that meet the given specifications. Adapted with changes from [21]

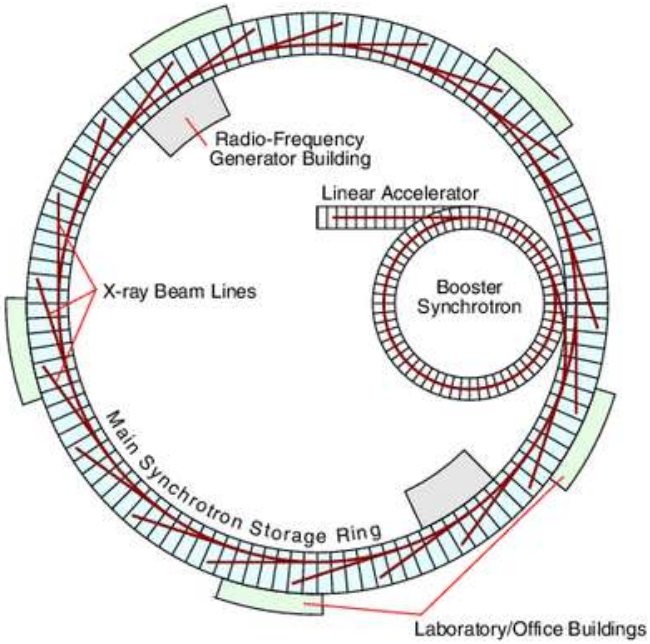

Figure 2.11: Diagram illustrates how the pathways taken by the brown lines determine the synchrotron radiation released as electrons go through the magnets. Adapted from [29].

One further characteristic that sets apart these 4th generation facilities is the extremely tiny size of the primary X-ray source (an electron bunch), which results in extremely coherent X-ray emission (up to 90% [32]). The characteristics that correspond to the dimensions parameters of the source are the electron beam emittance in the horizontal direction $\epsilon_{e,x}$ and the vertical direction $\epsilon_{e,x}$, respectively. The typical electron beam emittance values at 4th generation storage rings are less than 350 pm rad in both spatial and horizontal directions.

The 3 GeV synchrotron source MAX IV (Lund, Sweden) was the first storage ring built employing multi-bend achromat technology. It recently achieved its intended specifications of horizontal emittance of around 200–330 pm rad (depending on insertion device gap settings) [36]. The horizontal emittance of the Brazilian SIRIUS 3 GeV project, which is now in the operation stage, is anticipated to be between 150 and 250 pm rad [36]. The EBS ESRF facility, which has attained a horizontal emittance of 133 pm rad, has completed the upgrading of the high-energy ESRF 6 GeV storage ring. Other facilities throughout the world, such as APS-U, SPring-8, ALS, Soleil, Diamond, and others, are either in the planning or building stages.

The high-energy 6 GeV storage ring PETRA III at DESY in Hamburg is scheduled to be upgraded to PETRA IV (Fig. 2.10). This storage ring is intended to achieve the lowest emittance in the world for hard X-rays, which is around 20 pm rad in the horizontal direction [35]. Furthermore, this facility will retain the very high brightness of the source. The investigation of multifunctional hybrid materials, electronic transport phenomena, and electrochemical processes in charge storage materials under working conditions, as well as materials under extreme conditions of pressure and temperature with highest resolution and sensitivity, could be greatly aided by next-generation synchrotron sources, particularly the PETRA IV facility [37]. A further benefit of this synchrotron facility is the short pulse length and tightly defined temporal structure. As demonstrated in recent years using nuclear resonance scattering, X-ray photon correlation spectroscopy, pump-probe X-ray spectroscopy and diffraction, and time-of-flight spectroscopy of electrons and ions, such pulsed synchrotron radiation sources are ideal facilities for performing time-resolved experiments.

The whole beam can theoretically be captured and concentrated because the X-ray source will be extremely coherent up to 10 keV; the only factor limiting performance

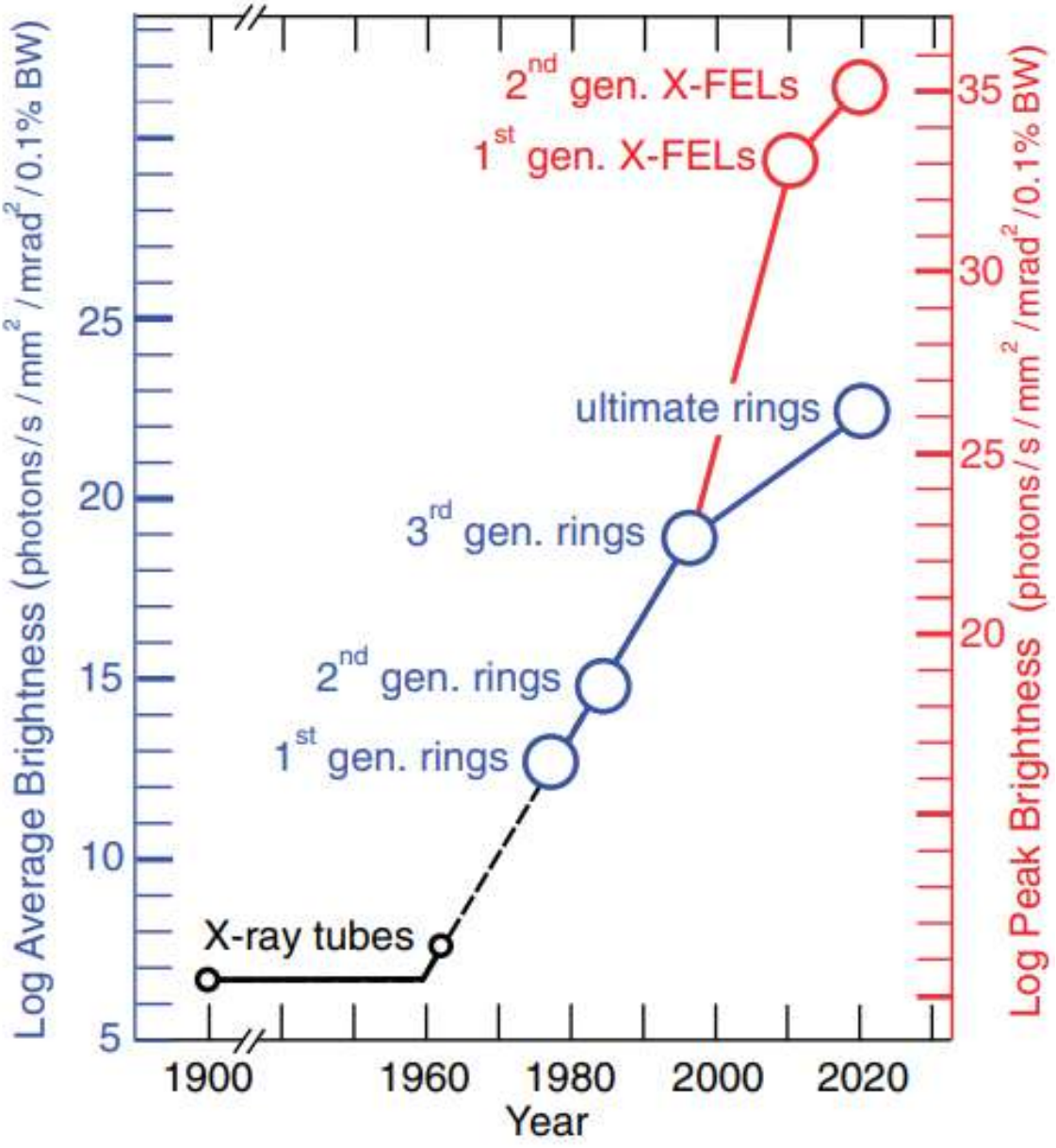

Figure 2.12: Peak brightness of XFELs (red) and average brightness of storage rings (blue) have increased historically and are expected to do so in the future. Adapted with changes from [33]

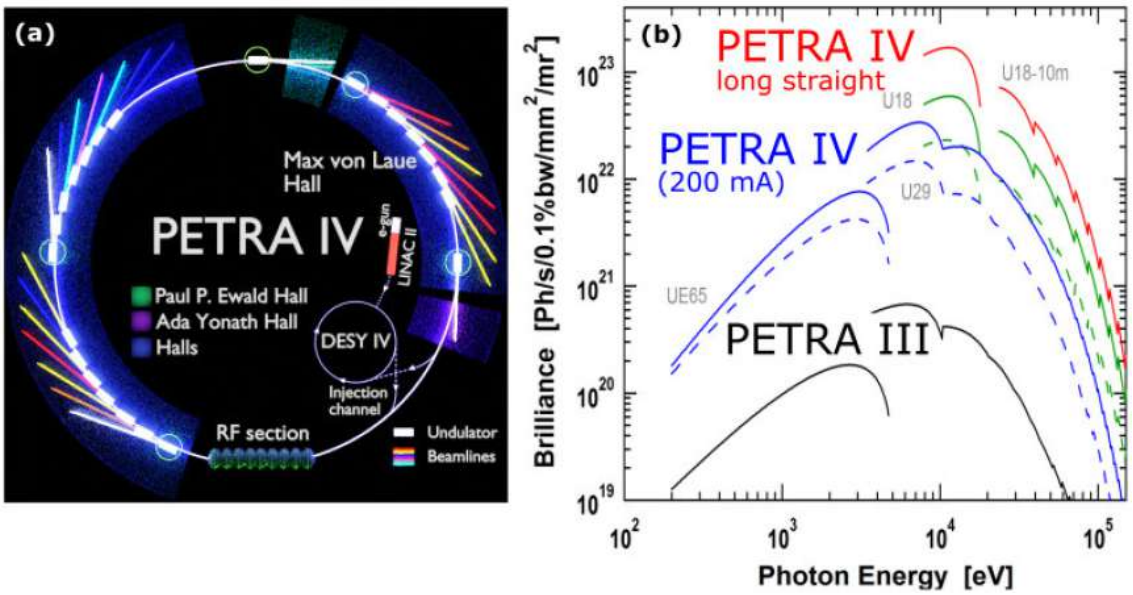

Figure 2.13: (a) Diagrammatic representation of the fourth generation synchrotron radiation source [34] (b) Comparison of PETRA IV (blue, green, and red curves) with PETRA III (black curves) storage rings' luminosities. The reference [35] was used to create this figure.

is optic quality. These brightness enhancements will also be seen in experiments with high energy resolution or at higher X-ray energies. Optics must be able to withstand increased X-ray intensities, be made smaller to better accommodate aberrations, and be able to fully use the potential of 4th generation sources. The greatest benefit from the record emittance and spectrum brightness of 4th generation synchrotron sources will go to X-ray microscopy methods. All X-ray analytical techniques will be greatly impacted by diffraction-limited focusing of the complete undulator beam since all of them may then be effectively exploited as contrast mechanisms in scanning microscopy. This will provide quantitative access to the local structure and characteristics of the materials under study on a nanoscale through the use of an "X-ray microscope."

2.4 Free-electron lasers for X-rays

Femtosecond lasers that function in the visible and near-infrared have been accessible for a number of years. They made it possible to study several phenomena, such as the creation of excitons or the vibration of molecules, that have characteristic periods less than a picosecond. However, the strength of a laser is determined by the wavelengths it uses, and its spatial resolution is restricted to a few hundred

nanometers. Conversely, structural data obtained using X-ray technology is at the atomic level. However, it is difficult to produce concentrated, strong, and perfectly coherent X-ray pulses from synchrotron storage facilities that have short durations (few femtoseconds). The development of the so-called X-ray free-electron laser (XFEL), which can function in both X-ray and far ultraviolet modes, has solved this problem.

With the development of XFELs, coherence could be increased to 95%, and peak brightness could be increased by ten times, reaching 10^{35}. LCLS at SLAC (1962) [38], which operated in hard X-rays, were the first FELs to demonstrate the SASE concept, and FLASH (2005) at Hamburg [39], which operated in the extreme ultraviolet photon range. Numerous more SASE XFELs quickly began operating, including SACLA (SPring-8 Angstrom Compact free electron LAser, 2011) [40], PAL-XFEL (Pohang Accelerator Laboratory,2016) [41], Swiss FEL (2016) [42], and European XFEL (2017) [43].

XFELs, which generate incredibly brilliant and brief X-ray radiation pulses, are based on a completely novel idea that Madey first proposed in 1971 [44]. The operational source was shown in the infrared spectrum in 1977 [45]. Building FELs in the X-ray range that provide incredibly short pulse durations is now possible thanks to the improved Self-Amplified Spontaneous Emission (SASE) process, which was proposed in 1980 [46] and in 1984 [47, 48] . The fundamental idea [44], [46] relies on the fact that an initial radiation field is amplified when an electron beam passes through a long undulator magnet.

2.4.1 The XFEL machine's fundamental idea

Electron beam

Since XFEL machines need high-quality injection electron beams with a low emittance to optimize FEL production, photocathode RF guns are often utilized. The shot noise signal generated by the photo-injector is represented by the electron beam of the starting condition. The resultant electron signal has quantum random fluctuations (Poisson process) as a result of extraction by a laser beam. The random variations observed in the beam current are indicative of simultaneous intensity modulation of the beam current at all frequencies, including the frequency set in

Figure 2.14: Examples of free-electron lasers with a specified electron beam energy parameter that produce soft and hard X-rays. A comparison of the peak brightness of the FELs is displayed in the bottom right plot. Adapted with changes from [15].

the undulator. The process of radiation begins when the electron beam reaches the undulator due to the existence of beam modulation at frequencies around the resonance frequency. Given that every potential harmonic appears in the shot noise beam, it is assumed that the input current has a homogenous spectral distribution. Transversely coherent fraction of radiation (XFEL) typically has an amplification bandwidth of around 0.1% because its spectrum is concentrated inside the narrow band, $\Delta\lambda$.

Afterwards extraction, the bunch is guided into the linac and accelerates by use of an electron radio frequency (RF) guns. The linac, which consists of a lengthy series of superconducting accelerating modules, beam-focusing magnets, and diagnostic apparatus, accelerates electrons to energies ranging from a few to tens of GeV. After going through the undulators, electron bunches flowed down to the beamlines. [21]

Research at XFELs

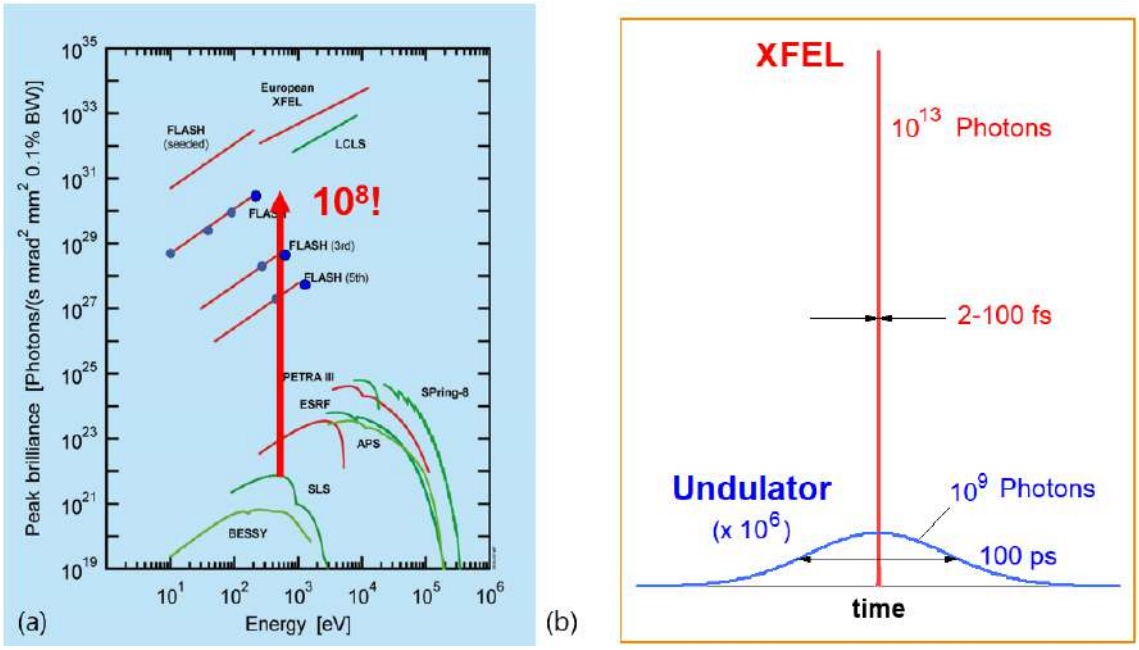

Figure 2.15: Comparison of Pulse Duration and Light Source Brilliance: (a) shows the peak brilliance from various light sources, with FELs such as FLASH showing noticeably higher brilliance. (b) Comparison of the duration of pulses and displays XFELs that have shorter pulses and produce more photons than conventional undulator sources. Adapted from [49].

XFELs were built with the primary objectives of imaging single molecules and getting molecular movies in mind. Preserving diffraction patterns before the samples are destroyed by a Coulomb explosion is the foundation of the imaging idea at the FEL. The main components that allow for single-particle X-ray diffractive imaging are the high pulse rate, the short duration of the pulse itself, and its transverse coherence [50]. This technique involves averaging the weak diffraction signal from individual biological particles throughout several observations. Hundreds of thousands of coherent X-ray pulses contact with replicas of the target sample that are orientated differently in these specialized imaging studies conducted at XFEL sources to establish the target sample's three-dimensional structure with the utmost resolution.

Another use for the ultrashort XFEL pulses is in the conduct of pump-probe experiments, in which a sample is first pumped by a standard infrared laser, and then the dynamics are evaluated by the probe pulse after a little delay. The dynamics of plasma-matter interactions, ultrafast phase transitions, and laser-induced molecular dynamics are all shown by these kinds of experiments [51, 52]. It is possible to study topological phases of matter (like skyrmions) or extremely non-trivial configurations of the electronic or spin system using time-resolved small-angle x-ray scattering in pump probe experiments at XFELs. These configurations frequently result in exotic and previously unimaginable material properties [53].

By utilizing higher-order photon correlation techniques to utilize intentionally damaged incoherent X-ray radiation at FELs, it is possible to determine the incoherent source or irradiated sample [54–56]. Simultaneously, statistical features of the XFEL beams may be examined by using higher-order photon correlation methods [54,57–59]. The results of these investigations open the way for utilizing the better coherence properties, brief pulse duration, and repetition rate of XFELs.

Research at European XFELs

The European XFEL stimulates new physics research that hasn't been done previously. It is challenging to investigate experimentally the dynamics and kinetics that take place on sub-microsecond and ultrafast timescales. These investigations were made possible by the creation of European XFEL, which allowed for the collection of diffraction pattern series at repetition rates of up to several MHz. With the high repetition rate of the EuXFEL pulsed source, it is possible to film chemical reactions,

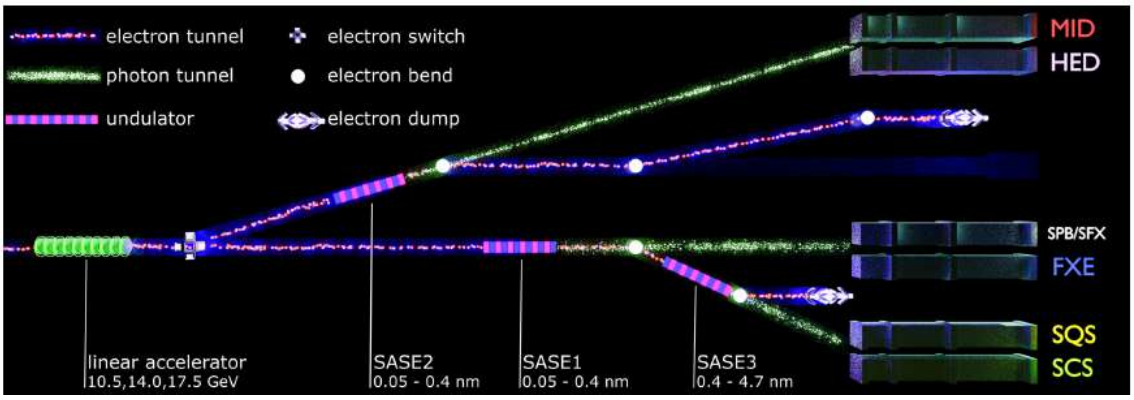

Figure 2.16: Diagram showing the instrumentation for EuXFEL. Adapted from [49].

investigate the properties of extreme states of matter, take three-dimensional images of nanoscale objects, trace ultrafast energy transfers within molecules, and determine the atomic structure of viruses.

The European XFEL facility has three distinct light sources (undulators SASE1–SASE3) that provide X-ray radiation with the greatest qualities directed towards the equipment in the facility's experiment hall, opening up potential for novel experiments (refer to Fig. 2.16). Advanced techniques like pump-probe can be used to conduct research at a variety of sophisticated experiment stations in the hard X-ray range (HED-2017, MID-2019, SPB, SFX, FXE) or soft X-rays (SQS, SCS) [60].

The High Energy Density Science (HED) and Materials Imaging Dynamics (MID) end stations' radiation source is represented by the configuration of SASE1 undulators. The MID beamline [61] employs X-ray scattering, imaging [62], and pump-probe methods to study soft and biological material (colloids, cells, and viruses), as well as condensed matter physics (glass formation and magnetism studies). Using X-ray photon correlation spectroscopy (XPCS), recent research using the MID instrument revealed abnormal dynamics and intriguing behavior in soft matter [63–65]. They also identified the heat diffusion transition regime caused by the ultrafast laser contact with solids [66]. Pump-probe techniques made accessible at EuXFEL at the MID station allowed for the possibility of these experiments.

With the capacity to create matter under severe pressure, temperature, or electric field conditions, together with harsh X-ray FEL radiation, the HED instrument at the EuXFEL offers a unique platform for investigations [67]. Under in-situ investigations

and experiments at the beamline, which is outfitted with a high-precision X-ray diffraction apparatus [68], offer insights into the structural phase transitions of complex solids under high magnetic fields, as well as novel extreme-pressure phases and solid-density plasmas. Recent investigations using the HED beamline have demonstrated structural alterations in silicate melts at extremely high pressures [69], the synthesis of novel materials at high pressures [69], and an unexpected cubic symmetry in Si materials [70]. High-power XFEL facilities are beginning to enable such material research under severe pressure and temperature conditions.

Conversely, within the soft X-ray division of the EuXFEL, scientific goals encompass comprehending and managing complicated materials, exploring ultrafast magnetization processes at the nanoscale, and observing chemical reactions in liquids in real-time through the utilization of Resonant X-ray Emission Spectroscopy (XES), CDI, and XPS. In ultrafast timeframes, phase transitions and unexpected transient states of matter can be induced when combined with femtosecond laser pulses. The kinetics of topological switching in the skyrmion phase were recorded in real-time by recent research conducted at the SCS (Spectroscopy and Coherent Scattering) using a single-shot infrared pump–X-ray probe [71]. The short X-ray pulse length and reciprocal-space resolution provided with the SCS device allow for an unusual sensitivity to the process.

The main uses of the SPB/SFX (Single Particles, Clusters and Biomolecules and Serial Femtosecond Crystallography Instrument) devices are diffractive imaging and atomic or near-atomic resolution structure determination of micrometer-scale and smaller objects. The device suggests studying viruses, macromolecule crystals, biological items, organelles, and cells. The main focus of the FXE (Femtosecond X-ray experiments) instrument's research is on dynamic analyses of chemical and biological interactions occurring in liquids. Femtosecond time resolution investigations using several techniques (X-ray diffuse scattering, wide-angle X-ray scattering, X-ray emission, and absorption spectroscopies) are possible with an enabling laser pump source.

As a function of photon energy, the left graph of Fig. 2.15 displays the peak brightness of a variety of light sources, such as synchrotron light sources (SLS) and free electron lasers (FELs) like FLASH and XFEL. The FLASH FEL shows a notable rise in brightness, as indicated by 10^8. With XFELs offering extremely short pulse

durations (2–100 femtoseconds) and a high number of photons (10^{13} photons per pulse), undulator sources provide longer pulse durations (100 picoseconds) with fewer photons (10^{9} photons per pulse). The right graph compares these two types of sources in terms of both pulse duration and photon count.

3 X-Ray Matter Interaction

This chapter is adapted from [17]. The interaction of the electromagnetic field with charged particles is the basis for the scattering of X-rays from matter. The material's electrons contribute significantly to the scattering process. This section introduces wave propagation through a thin slab of material and summarizes the key physical processes of x-ray-matter interaction.

3.1 One electron

One free electron will be the most basic scattering object to discuss. We will determine the scattering length, which is a measure of an electron's capacity to scatter an X-ray. A schematic of a general scattering experiment is presented in Figure 3.1. Under such an experiment, the differential scattering cross-section ($\mathrm{d}\sigma/\mathrm{d}\Omega$), which is defined by

$$\frac{d\sigma}{d\Omega} = \frac{I_{SC}}{\Phi_0 \Delta\Omega} \tag{3.1}$$

The flux, Φ_0, or simply the number of photons that travel through the unit area per second, determines the strength of the incident beam. The incident beam is dispersed after interacting with the scattering material. The number of scattered photons recorded in a detector per second, I_{SC}, is determined by placing the detector R distances away from the object and subtending a solid angle $\Delta\Omega$. Therefore, once the experiment's specifics, such as the input beam's flux and the detector's size, have been normalized, the differential cross-section serves as a measure of the scattering process's efficiency.

An equation for Φ_0 may be found in terms of the incident beam's electric field E_{in} in the specific scenario of electromagnetic wave scattering. The flux Φ_0 is defined as density multiplied by the speed of light, c, and the density of photons is proportional

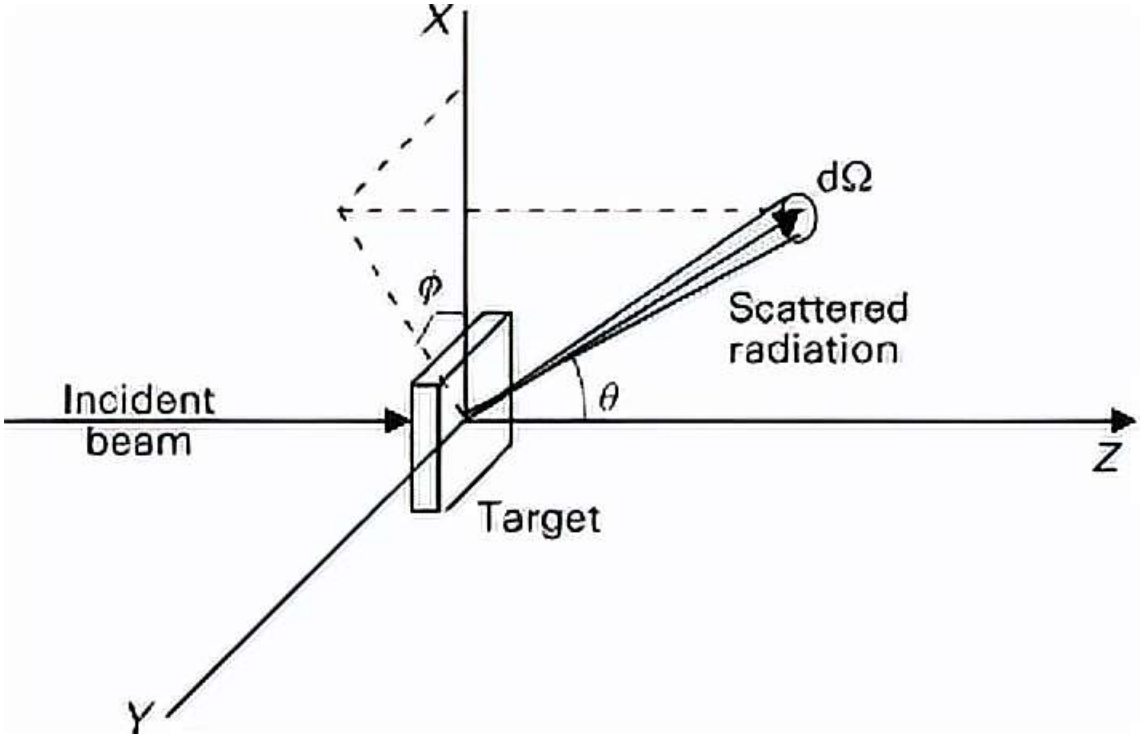

Figure 3.1: Diagrammatic representation of the differential cross-section from a general scattering experiment.

to $|E_{in}|^2/\hbar\omega$ since the energy density is proportional to $|E_{in}|^2$. The scattered beam's intensity, I_{SC}, is subject to a similar argument. In this instance, the modulus squared of the radiated electric field, $|E_{rad}|^2$, determines the density. To get an equation for I_{sc}, this number must be multiplied by the detector's area, $R^2\Delta\Omega$, and c. Taking these factors into account, the differential cross-section is provided by

$$\frac{d\sigma}{d\Omega} = \frac{|E_{rad}|^2 R^2}{|E_{in}|^2} \tag{3.2}$$

An electron put in the electric field of an incoming X-ray beam will be driven to oscillate in a classical description of the scattering process. A source is a vibrating electron that emits a spherical $E_{rad} \propto \varepsilon' \mathbf{e^{ikR}}/\mathbf{R}$ wave.

Because of the limited speed at which the radiation propagates, the radiated field is proportional to the electron's charge, e, and to the acceleration, $a_X(t')$, measured at a time earlier (t') than the observation time (t). Thus, it is anticipated that the

radiated field will have the form

$$E_{rad}(R,t) \propto \frac{-e}{R} a_X(t^{'}) sin\Psi \tag{3.3}$$

where, $(t^{'} = t - R/c)$. The energy density, proportional to $|E_{rad}|^2$, multiplied by the surface area, proportional to R^2, determines the total energy flow through a spherical shell of radius R; so, as $|E_{rad}| \propto R^{-1}$ increases, the total energy flow becomes independent of R. An additional element of $sin\Psi$ has been incorporated to accommodate the acceleration's fluctuation with the observation angle. In order to continue, we calculate the total acceleration by dividing the force acting on the electron by its mass, which provides

$$a_X(t^{'}) = \frac{-eE_0 e^{i\omega t^{'}}}{m} = \frac{-e}{m} E_{in} e^{i\omega(R/c)} = \frac{-e}{m} E_{in} e^{ikR} \tag{3.4}$$

where E_{in} is the electric field of the incident wave, $E_{in} = E_0 e^{i\omega t}$. Therefore, Eq. (3.3) becomes

$$\frac{E_{rad}(R,t)}{E_{in}} \propto (\frac{e^2}{m}) \frac{e^{ikR}}{R} sin\Psi \tag{3.5}$$

It is necessary to review the factor of $sin\Psi$ for an observation point at every angle with regard to the polarization of the incident beam. Based on Fig. 3.1, if ε **represents the polarization of the incident field and** $\varepsilon^{'}$ **that of the radiated field, then** $\varepsilon \cdot \varepsilon^{'} = cos(90^\circ + \Psi) = sin(\Psi)$**. This method of expressing the apparent acceleration's trigonometric component has the benefit of being applicable to all conceivable observation angles. It is evident that the electric field ratio provided in Eq. (3.5) doesn't have dimension. The correct length may be determined by observing that the Coulomb energy, expressed in SI units, at a distance of r from a point charge** e **is equal to** $e^2/(4\pi\epsilon_0 r$**. Furthermore, the energy has a dimensional form of** mc^2**. The fundamental length scale may be expressed as follows by equating these two formulas for energy:**

$$r_0 = \frac{e^2}{4\pi\epsilon_0 mc^2} = 2.82 \times 10^{-5} \mathring{A} \tag{3.6}$$

This is known as the electron's classical radius, or Thomson scattering length. Actually, $-r_0|\varepsilon \cdot \varepsilon^{'}|$ is the scattering amplitude from a single electron. The fact that

there is a 180◦ phase shift between the incident and dispersed waves is physically represented by the factor of 1. Consequently, the radiated to incident electric field ratio is

$$\frac{E_{rad}(R,t)}{E_{in}} = -r_0 \frac{e^{ikR}}{R} |\varepsilon \cdot \varepsilon^{'}| \tag{3.7}$$

and Eq.3.7 can be written as follows and Thomson differential scattering cross-section of an electromagnetic wave by a free electron is expressed by this equation

$$\frac{d\sigma}{d\Omega} = r_0^2 |\varepsilon \cdot \varepsilon^{'}|^{\mathbf{2}}. \tag{3.8}$$

3.2 One atom

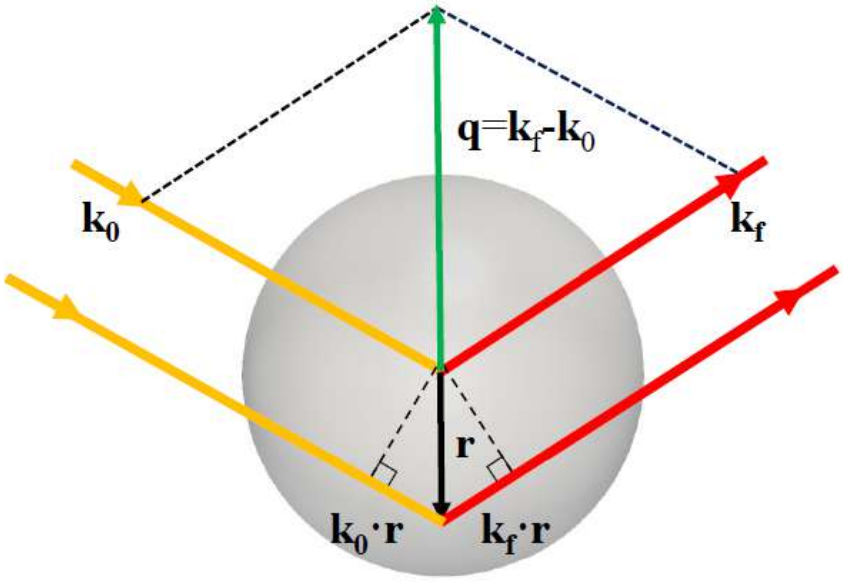

Figure 3.2: Scattering by an atom. The incident and dispersed wave wavevectors are represented by the symbols $\mathbf{k_0}$ and $\mathbf{k_f}$. A wave scattered at the origin and one at a point r have different phases, and this phase difference is represented by $\mathbf{k_0} \cdot \mathbf{r} - \mathbf{k_f} \cdot \mathbf{r}$. Adapted from [72].

This chapter is adapted from [17]. Initially, a purely classical description will be employed, whereby a number density, $\rho(r)$, specifies the electron distribution. The contributions from various volume constituents of this charge distribution are superimposed to form the scattered radiation field. As seen in Fig. 3.2, one must

monitor the incident wave's phase as it interacts with the volume elements at the origin and point r in order to assess this superposition.

Two consecutive crests have a phase difference of 2π. When projected onto the incident direction and wavelength, the phase difference between the two volume components is equal to 2π multiplied by the ratio of r. All involved here is the scalar product of vectors **k** and **r**. One of the main benefits of using the wavevector k to characterize the incident wave is its simple way of representation. Between a scattered wave from a volume element around the origin and one near r, there is a phase difference of $-\mathbf{k_f} \cdot \mathbf{r}$. The phase difference is

$$\Delta\phi(\mathbf{r}) = \mathbf{k_0} \cdot \mathbf{r} - \mathbf{k_f} \cdot \mathbf{r} = -\mathbf{q} \cdot \mathbf{r}, \tag{3.9}$$

where the incident and scattered fields' wavevectors are denoted by $\mathbf{k_0}$ and $\mathbf{k_f}$, respectively, and the scattering vector $\mathbf{q} = \mathbf{k_f} - \mathbf{k_0}$ is referred to as the wavevector transfer. Given that the scattering events seen in Fig. 3.2 are elastic and that $|\mathbf{k_0}| = |\mathbf{k_f}|$, we may calculate $|q| = 2|k|sin\theta = (4\pi/\lambda)$ sinϑ from the scattering triangle. As we will see, **q** is often given in units of $\mathring{A}^1$, and it is the appropriate variable to characterize elastic scattering processes.

As a result, a volume element $d\mathbf{r}$ at **r** will add $d\mathbf{r}$ to the scattered field, which has a $\mathbf{q} \cdot \mathbf{r}$ phase factor. The atom's total scattering length is

$$-r_0 f^0(\mathbf{q}) = -r_0 \int \rho(\mathbf{r}) e^{-i\mathbf{q}\cdot\mathbf{r}} d\mathbf{r} \tag{3.10}$$

where, $f^0(\mathbf{q})$ is the atomic form factor. As $f(\mathbf{q})$ becomes closer to Z, the number of electrons in the atom, in the limit q=0, all of the various volume elements scatter in phase. With an increase in q from zero, the various volume elements begin to scatter out of phase, which ultimately limits $\lim_{q\to\infty} f(\mathbf{q}) = 0$. One may identify the right-hand side of Eq. (3.10) as a Fourier transform. It should be evident that we must evaluate Eq. (3.10) and multiply the result by its complex conjugate in order to determine the scattered intensity.

Naturally, discrete energy levels and quantum mechanics regulate atomic electrons. The electrons in the K shell, whose energies are similar to those of a typical X-ray

photon, are the most closely bonded. Because these electrons are bonded, their reaction to an external driving field is diminished if the energy of the X-ray photon is significantly smaller than the binding energy of the K shell. While electrons in less securely bonded shells (L, M, etc.) will be able to react to the driving field more strongly, in general, we anticipate that an atom's scattering length will be reduced by a certain amount, commonly represented by the symbol *f'*. It is possible to regard the electrons as free and assume that *f'=0* at energies far higher than the binding energy. Apart from modifying the actual scattering length, we anticipate that the electron's reaction will exhibit a phase lag in relation to the driving field, similar to that of a forced harmonic oscillator. This is made possible by the addition of the term *f"*, which stands for system dissipation. Therefore, by combining all the results, the atomic form factor becomes

$$f(q, \hbar\omega) = f^0(q) + f'(\hbar\omega) + if''(\hbar\omega) \tag{3.11}$$

where *f'* and *f"* represent the anomalous dispersion correction's real and imaginary components, respectively. To highlight that strongly bonded inner-shell electrons dominate *f'* and *f"* behavior, we have represented them as functions of the X-ray energy $\hbar\omega$. As a result,*f'* and *f"* behavior cannot have any apparent dependency on $\mathbf{q}$. As one may anticipate from these preliminary words when the X-ray energy equals one of the atom's absorption edge energies, *f'* and *f"* take on their extreme values. All the components in the decomposition (above equation) reach their extreme levels when ω is near one of the resonance frequencies in the atom, resulting in a substantial increase in total scattering. As a result, there is a noticeable change in the absorption coefficient's energy dependence close to the resonance, which is referred to as the absorption edge. The atomic factor exhibits strong sensitivity to the electronic state structure of the atom in this small energy range.

3.3 One molecule

This chapter is adapted from [17]. The scattering length for an electron and an atom made up of electrons has been discussed so far. It follows that the scattering length of a molecule will have a form factor, exactly like the scattering length of an

atom. By assigning an index j to each atom in the molecule,

$$F^{mol}(q) = \sum_j f_j(q) e^{iqr_j} \tag{3.12}$$

where $f_j(q)$ is the atomic form factor of the jth molecule in the atom. It is possible to estimate the locations of the atoms in the molecule if $F^{mol}(q)$ can be determined experimentally for a significant number of values of the scattering vector q. However, even in the extremely strong X-ray beams produced by today's synchrotron sources, the scattering length of a single molecule is insufficient to create a quantifiable signal. To do this, large-scale molecular samples that are either crystalline or non-crystalline in nature must be constructed.

3.4 X-ray diffraction by crystals: a kinetic hypothesis

Crystal diffraction of coherent X-ray light is one of the most amazing phenomena in X-ray research. The radiation scattered by various atoms interacts favorably in some directions in this instance, and the ordered ensemble of atoms functions as a three-dimensional (3D) diffraction lattice. Bragg peaks are the name for the strong peaks that appear on the detector as a result of the scattering pattern. Max von Laue made an experimental discovery of this phenomenon in 1912 [73] [74], and William Bragg provided a theoretical explanation in 1913 [75].

The kinematical and dynamical theories are two theoretical stances that explain how periodic structures affect the wave field. A significant simplification results from the kinematic theory's underlying assumption that the scattered radiation does not undergo rescattering on the way to the detector. Because it holds true when the intensity of the diffracted radiation is low compared to the intensity of the incident wave, this approximation is sometimes referred to as the weak-scattering limit [76]. The numerous scattering and interference effects brought about by the coupling of the transmitted and scattered waves in a crystal are taken into consideration by the dynamical theory. When X-ray diffraction occurs on a large crystal, the dynamical theory considers the consequences of multiple scattering, which becomes crucial. Dynamical theory provides a comprehensive explanation of refraction, extinction, and interference effects, in contrast to the kinematical approach. The impact of multiple scattering only become substantial for reasonably big crystals (around

microns) due to the poor interaction of X-rays with a medium. Given that the majority of crystalline materials seen in nature are made up of small, flawless blocks with a variety of orientations, the kinematic method is frequently adequate even in this situation. Within the framework of kinematic theory, diffraction on each block may be examined with an adjustment for the intensity loss that happens when the incident beam traverses the block (also known as secondary extinction). When large, perfect crystals of silicon and germanium were created artificially and used as the raw materials for the semiconductor revolution, scholarly interest in the dynamical theory began to expand quickly [77]. The dynamical theory of X-ray diffraction has various applications in modern X-ray physics, prominent among them being X-ray optics. We will go over the kinematic theory of X-ray diffraction using the example of an ideal crystal. [72]

An infinite medium with translational symmetry made out of identical cells (single or many atoms, molecules, etc.) is called an ideal crystal. These unit cells are characterized by three linearly independent space vectors, $\mathbf{a_1}$, $\mathbf{a_2}$, $\mathbf{a_3}$, and are positioned with an invariant translational symmetry. Next, each unit cell is moved in relation to each other by a distance determined by a translation vector

$$\mathbf{R_n} = n_1\mathbf{a_1} + n_2\mathbf{a_2} + n_3\mathbf{a_3}, \tag{3.13}$$

where the numbers n_1, n_2, and n_3 are integers. The crystalline lattice is a regular repeating pattern created by the periodic and systematic arrangement of atoms. Standard works on crystallography, such as [78], provide the complete categorization of all crystal structures, which include the 32 symmetry classes and 14 different types of lattices known as Bravais lattices. $\mathbf{R_n} + r_j$ gives the position of any atom in the crystal if $\mathbf{R_n}$ are the lattice vectors that define the lattice and r_j are the atoms' positions with respect to any given lattice site. Consequently, the crystal's scattering amplitude factorizes into the product of two components, which we represent as

$$F^{mol}(q) = \sum_j f_j(q) e^{iqr_j} \sum_j e^{iqR_n}, \tag{3.14}$$

where the first term is the unit cell structure factor and the second term is the sum over lattice locations. Phase factors on the unit circle in the complex plane are all

the terms in the lattice sum provided in Eq. (3.15).

$$q \cdot \mathbf{R_n} = 2\pi \times integer. \tag{3.15}$$

In reciprocal space, the infinite periodicity function is represented by the Fourier transform of the direct lattice. The sum of the δ-functions normalized by the unit cell volume $V_u c$ provides that. It gives the description of a reciprocal lattice, or regular grid, with basis vectors.

$$\mathbf{b_1} = 2\pi \frac{\mathbf{a_2} \times \mathbf{a_3}}{\mathbf{a_1} \cdot (\mathbf{a_2} \times \mathbf{a_3})}; \mathbf{b_2} = 2\pi \frac{\mathbf{a_3} \times \mathbf{a_1}}{\mathbf{a_1} \cdot (\mathbf{a_2} \times \mathbf{a_3})}; \mathbf{b_3} = 2\pi \frac{\mathbf{a_1} \times \mathbf{a_2}}{\mathbf{a_1} \cdot (\mathbf{a_2} \times \mathbf{a_3})}. \tag{3.16}$$

The reciprocal lattice vector is determined by the location of each node on this grid.

$$\mathbf{G_{hkl}} = h\mathbf{b_1} + k\mathbf{b_2} + l\mathbf{b_3}, \tag{3.17}$$

where h,k,l are integers. When the scattering vector aligns with a reciprocal lattice vector, the periodicity function therefore assumes nonzero values

$$\mathbf{q} = \mathbf{G_{hkl}}. \tag{3.18}$$

The Laue condition for the observation of X-ray diffraction is expressed as Eq. (3.18). In terms of physics, that is equivalent to the situation when the waves scattered by a single unit cell are in phase with the waves scattered by neighboring cells. The entire crystal experiences constructive interference as a result of translational symmetry, which produces a vibrant intensity peak in the chosen direction.

An elegant and straightforward method for visualizing diffraction events in reciprocal space is the Ewald construction, which is schematically depicted in Figure 3.3. The incident $\mathbf{k_0}$ and diffracted $\mathbf{k_h}$ wave vectors, when plotted in relation to the reciprocal lattice, form a triangle, with the scattering vector $\mathbf{q} = \mathbf{k_h} - \mathbf{k_0}$ representing the third side. The vector $\mathbf{k_0}$ forms an angle of θ_B with the crystalline planes and points to the reciprocal space origin. Starting at the same location as vector $\mathbf{k_0}$, vector $\mathbf{k_h}$ moves in the direction of the detector position. Then, a sphere of radius $2\pi/\lambda$, built around the wave vectors' starting point, represents every possible position in reciprocal space for a particular crystal orientation. That spherical cross-section of the reciprocal space is called the Ewald sphere [78], according to the published study.

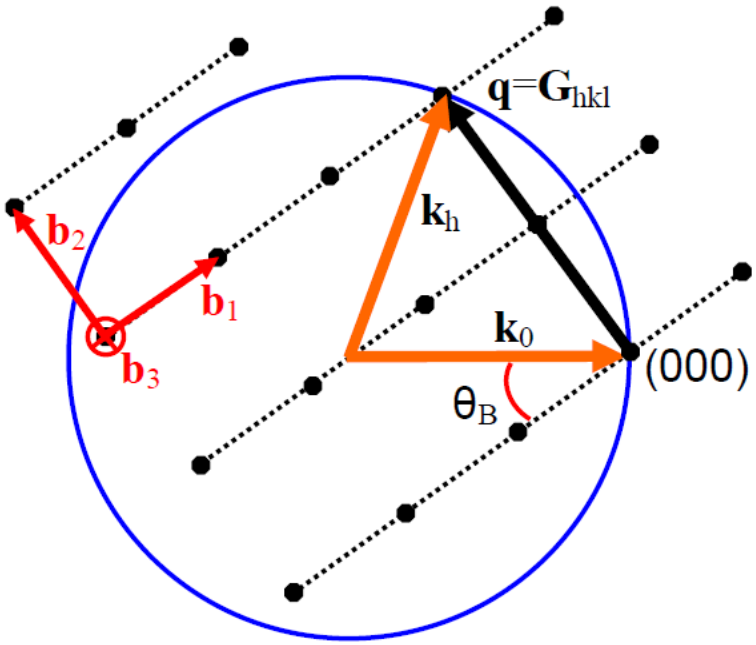

Figure 3.3: Graphical representation of the Bragg condition by the Ewald sphere along with the reciprocal lattice of a crystal with the basis vectors $\mathbf{b_1}, \mathbf{b_2}, \mathbf{b_3}$, and diffracting planes in real space, correspondingly marked with dash lines. Adapted with changes from [72].

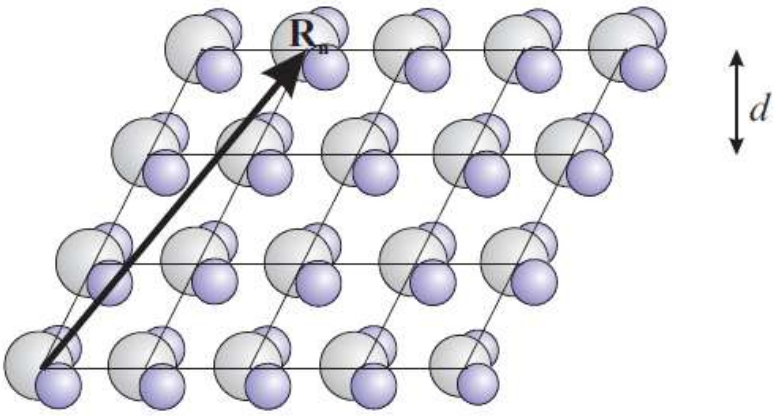

Figure 3.4: Scattering from a crystal of molecules. With position vectors R_n and a lattice plane spacing of d, the molecules are arranged on a lattice [17].

It must be admitted that, in reality, the detector's solid angle, which defines the thickness of the sphere, and the incident radiation's bandwidth are used to determine the intensity of the measurement. When the Ewald sphere passes over a node in reciprocal space with the vector $\mathbf{G_{hkl}}$, constructive interference is discovered, which fulfills the Laue condition.

A collection of parallel, equally spaced planes in the crystal corresponding to each node in reciprocal space designated by the reciprocal lattice vector $\mathbf{G_{hkl}}$. As seen here, the reciprocal lattice vector's magnitude and the distance between the planes d_{hkl} are related

$$d_{hkl} = \frac{2\pi}{|\mathbf{G_{hkl}}|}. \tag{3.19}$$

It is evident that one of the planes crosses the unit cell's origin, and the next closest one intercepts the crystallographic axes $\mathbf{a_1}$, $\mathbf{a_2}$, $\mathbf{a_3}$ at $\mathbf{a_1/h}$, $\mathbf{a_2/k}$, $\mathbf{a_3/l}$. In literature, the numbers **h**,**k**,**l** also known as Miller indices, are frequently employed to indicate the family of crystallographic planes. The direct lattice basis and these values may be used to determine planar spacing. For instance, it follows simply from geometry that, in the case of a cubic lattice

$$d_{hkl} = \frac{a}{\sqrt{h^2 + k^2 + l^2}}. \tag{3.20}$$

The Laue condition for a family of reflections may be redefined as follows by using the relation:

$$2d_{hkl}sin\theta_B = n\lambda, \tag{3.21}$$

where the order of the reflection is denoted by n = 1, 2, 3. Bragg's law refers to this way of expressing the diffraction condition.

The peak's typical width narrows with increasing crystal size and vice versa. Instrumental broadening is introduced into the peak width if the X-ray beam's size is equivalent to that of the sample or if the radiation is not entirely coherent with the crystal's size. When it comes to mosaic crystals, the Bragg peak's structure is made up of contributions from each tiny, perfect block, with the orientations distributed around a mean value. The average size and the angular dispersion of the mosaic blocks are then described by the linear growth of the peak width from the first level of reflections to higher orders. The Williamson-Hall technique [79] is the equivalent examination of the crystal's mosaicity characteristics performed by Bragg diffraction. In a limit, when the sample consists of a very large number of microcrystals oriented randomly, the Bragg peaks turn into uniform rings. Since all possible crystal orientations are evaluated simultaneously, the recorded diffraction data correspond to a three-dimensional reciprocal lattice projected onto a one-dimensional space [80].

Numerous applications of the kinematical theory may be found in imaging, and crystallography. A notable instance of this is the structural analysis of X-ray diffraction, which involves determining the maximum number of Bragg peaks as a function of Miller indices in order to solve the three-dimensional structure of the crystalline material. This approach determines the structure factor by using the relative intensities and positions of the Bragg reflections. The positions of the Bragg peaks provide information about the lattice symmetry and the lengths between the crystallographic planes, while the relative intensities provide information about the spatial arrangement of the atoms or molecules in the unit cell. But in order to fully understand the structural element, phases of the reflections are also necessary, and they cannot be quantified. With the development of sophisticated methodologies [81], it is now possible to identify a unique solution, and the structure determination procedure for a single crystal is now regular and heavily automated.

3.5 Principles of X-ray Diffraction:

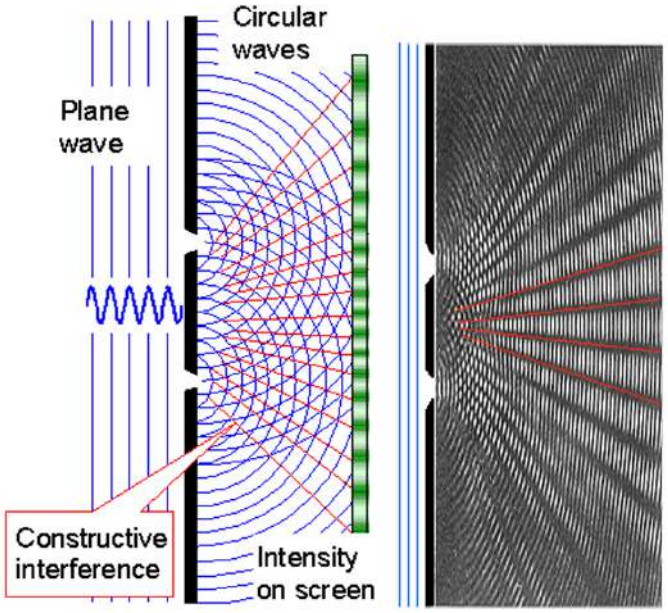

Figure 3.5: Generation of spherical waves and their interference, resulting in constructive and destructive interference. Adapted with changes from [82]

This section is based on [82]. The purpose of having the beam of X-rays fall on the material is to find out information at the atomic scale. Under most circumstances, there will be no X-rays coming out from the material due to the destructive interference scattering. In certain special cases, the part of incident radiation comes out

from the material due to constructive interference of scattered radiation carrying all the information regarding the crystallography of the material, and this process is known as the process of diffraction. As the two waves propagate towards each other, they start to overlap. At certain points where the peaks of the waves coincide, the amplitudes of the waves add together, resulting in a larger amplitude. This is known as constructive interference. In contrast, at certain points where the peaks of one wave coincide with the troughs of the other wave, the amplitudes of the waves cancel out, resulting in a smaller amplitude. This is known as destructive interference.

In Fig. 3.5, the blue lines indicate the peaks of the wave, which, when passed through the pinholes, would eventually create spherical waves. Having such pinholes at equal distances would eventually act as a diffraction grating. The 3D lattice can be considered a three-dimensional diffraction grating. The atoms can be seen as the obstacles that create these spherical waves when the X-ray beam strikes them. These spherical waves will then superimpose with each other. This is the concept of Young's double-slit experiments.

Usually the intensity of the diffracted beam is much weaker than the incident beam; approximately one or less than 1% of the intensity of the incident beam is obtained as a diffracted beam from the material. Inside the material, we have a number of atomic planes, with a number of atoms lying on each plane. So, whenever the X-ray beam is incident on an atom, it interacts with the electrons in the outer shells of the atoms, and due to this interaction, the incident ray will be scattered in all directions. With this, one can also comment that atoms are nothing but the scattering centers. By analyzing the diffracted beam, we can determine the locations of atoms, crystal structure, type of unit cell, parameters of the material, etc.

Now here we consider the plane wave, traveling in a direction with a wave vector $\mathbf{k}$ and with the wave vector length $|\mathbf{k}| = 2\pi/\lambda$. Here, we can now have two possibilities. Either the wave can travel through the lattice or it can get reflected from the other lattice points (or atoms) and now travel in a different direction. The wave would get reflected when the angle between the incident wave and the lattice place is θ, which is known as the Bragg angle, giving us Bragg's law. Thus, the lattice structure could tell us where we will find these reflections, giving rise to different lattice structures. At the same time, the atoms within the lattice would contribute to the intensity of these reflections [82]. Bragg's law is a fundamental principle in X-ray crystallography

that describes how X-rays interact with a crystal lattice and produce a diffraction pattern. The law states that when an X-ray beam strikes a crystal lattice at a particular angle, the X-rays will be diffracted at specific angles that are determined by the spacing between the lattice planes.

The Bragg equation relates the wavelength of the X-rays, the spacing between the lattice planes, and the angle at which the X-rays are diffracted. One would achieve a maximum in these reflected waves when the path length difference in the two reflected waves is an integral multiple of the wavelength. Mathematically,

$$Path \quad difference = n\lambda \tag{3.22}$$

$$AO = BO = d\sin\theta \tag{3.23}$$

where the path difference is given by AO+BO. Thus, the total path length difference is $2d\sin\theta_B$, which should be equal to $n\lambda$ for a peak intensity. When these conditions are met, the diffracted X-ray beam will have a specific intensity and angle of diffraction that can be measured and used to determine the structure of the crystal lattice.

3.6 X-rays through a material

This section is adapted from [17]. Let us assume a simple scenario where X-rays are passing through a given material of a certain thickness (Fig. 3.6). Suppose the absorbing material thickness is L, the intensity of the incident X-ray beam is I_0 and the intensity of the transmitted beam is I_L. Naturally, the I_L is less than I_0.

The fractional change in intensity when an X-ray passes through the material is given by:

$$-\frac{dI}{I} = \mu dL, \tag{3.24}$$

where, I is the intensity of the X-ray beam, dI is the fractional change in the intensity, μ is the linear absorption coefficient, and dL is the distance traversed. Now

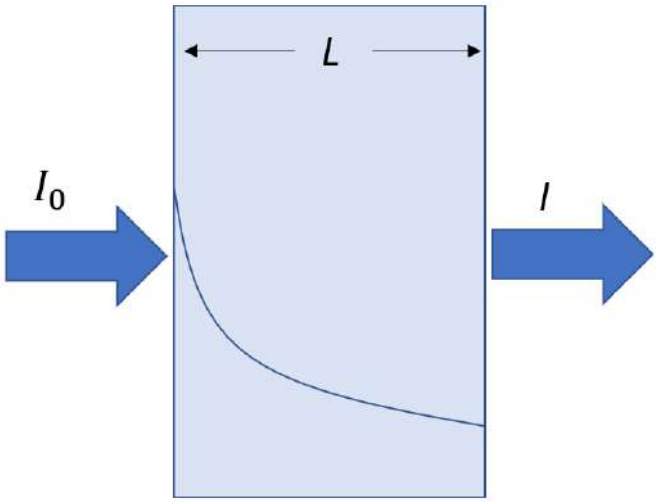

Figure 3.6: X-ray absorption through a material of thickness L

integrating equation above would give:

$$I_L = I_o e^{-\mu L} or I_L = I_o e^{-\frac{\mu L}{\rho}} \tag{3.25}$$

which is also known as the Lambert-Beer Law. Where ρ is the density of the material and μ/ρ is the mass absorption coefficient. The higher the value of this coefficient, the higher the absorption of the X-rays. Similarly, a thicker material will also cause higher attenuation in the transmitted energy. Moreover, the absorption coefficient can also be defined as:

$$\mu = \frac{\rho \cdot N_A}{M} \cdot \sigma_a, \tag{3.26}$$

where N_A is the Avogadro's number, M is the molar mass and σ_a is the absorption cross-section,. If one has several materials in a single sample, then we can easily find the mass absorption coefficient by

$$\frac{\mu}{\rho} = \frac{\mu}{\rho_1} + \frac{\mu}{\rho_2} + \frac{\mu}{\rho_3} + ... \tag{3.27}$$

In the case of X-ray fluorescence spectroscopy, the X-rays are emitted by the sample and have a broad range of wavelengths that include K-alpha, K-beta, and white radiation. To isolate the K-alpha radiation, a crystal monochromator is used. The crystal is positioned at a specific angle relative to the incident X-rays such that only

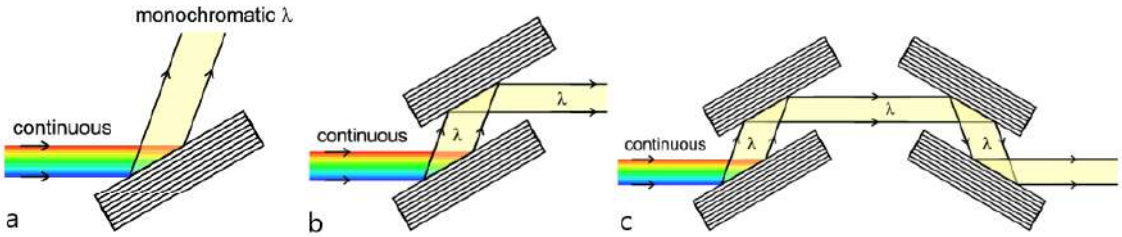

Figure 3.7: Different configurations of a) single crystal arrangement, b) double monochromator, c) 4 bounce arrangement. Adapted from [83]

the K-alpha radiation is diffracted by the crystal's atomic planes, while the K-beta and white radiation are not diffracted or are diffracted at a different angle.

This requires precise orientation of the crystal, which allows the diffraction of the wavelengths, satisfying Bragg's law at that angle. One of the commonly used monochromators is the 'double channel' monochromator, which allows the right orientation or direction of the diffracted monochromatic energy, but the beam height is altered. One can use the single crystal as well, but that could lead to disorientation of the diffraction beam. Another type of monochromator would include the use of multiple crystals, which are complex in design but would allow aligning both the height as well as the direction of the beam. In the case of a double-channel monochromator, both the crystals are part of the same crystal structure, where a central channel is cut to provide the two crystal surfaces for the beam diffractions. Moreover, in this way, in a 4-bounce arrangement, two double-channel monochromators are used. These configurations are shown in Fig. 3.7.

The K-alpha radiation that is diffracted by the crystal is then collected and directed to the detector, resulting in a monochromatic signal at the wavelength corresponding to the K-alpha radiation. By selectively filtering out the unwanted K-beta and white radiation using the crystal monochromator, a monochromatic signal is achieved, which allows for a more accurate determination of the sample's elemental composition. When a polychromatic X-ray beam is incident on the crystal, it is diffracted at different angles depending on the individual wavelengths. The crystal is oriented at a specific angle such that only the K-alpha radiation is diffracted in a way that produces constructive interference. The K-beta and white radiation are either not diffracted or diffracted at a different angle and are thus not recorded by the detector. The diffracted K-alpha radiation then passes through a slit or collimator that further narrows the range of angles and wavelengths that can pass through. The resulting

collimated monochromatic beam of K-alpha radiation is then directed onto the sample, and the emitted X-rays are detected and analyzed.

4 Semiconductor nanowires

The fundamental structural characteristics of nanowires (NWs) and associated heterostructures are covered in this chapter. The history and current uses of semiconductor NWs are covered in the introduction section. In this chapter, we also talk about strain relaxation and typical development strategies in NWs.

4.1 Introduction

Isamu Akasaki, Hiroshi Amano, and Shuji Nakamura shared the 2014 Nobel Prize in Physics "for the invention of efficient blue light-emitting diodes which enabled bright and energy-saving white light sources" [86]. It is an example of the enormous advancements made in the previous several decades in the field of lighting devices based on semiconductors. The whole visible light spectrum is emitted by the phosphors, which are pumped by the incredibly effective blue light-emitting diodes (LEDs). Band gap adjustment from the near-infrared to the deep ultraviolet spectral

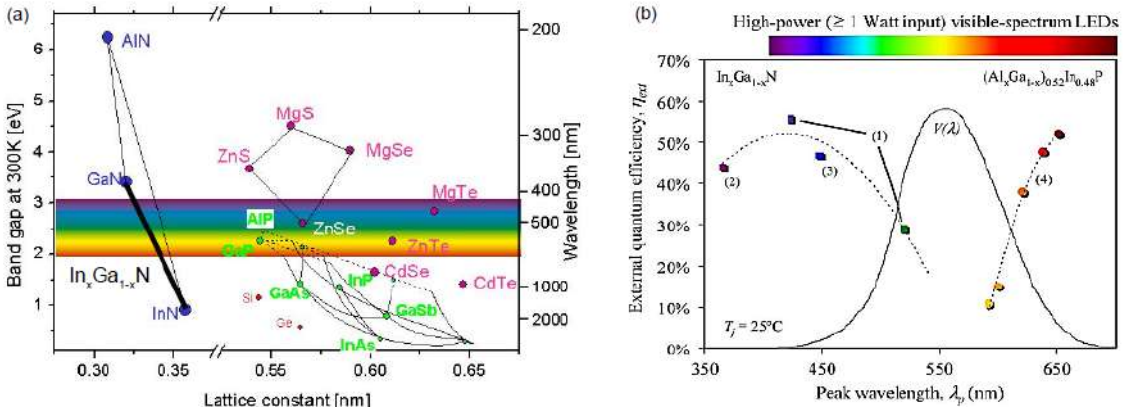

Figure 4.1: (a) Binary semiconductor band gap diagram with matching visible light emission spectrum [84]. The whole visible range is covered by compounds in the form of $In_xGa_{1-x}N$ (indicated by a thicker line). (b) The decrease in the green-to-yellow light area is revealed by the external quantum efficiency for ternary compounds such as $In_xGa_{1-x}N$ [85].

region is possible using ternary compounds, which are based on III-nitrides (see Fig. 4.1(a)). The term "green gap" refers to a decline in external quantum efficiency that occurs in planar LEDs in the green-yellow spectral range (see Fig. 4.1(b)). This limitation arises from the difficulties in generating stressed planar structures that are free of defects. The growth processes cause misfit dislocations to occur at the interface where the mismatched layers that make up the electrical device meet. The concentration of these faults has a major impact on charge carrier movement. Consequently, switching to NWs is seen as a possible next step in improving performance and lowering production costs for electrical products. Since the NWs have a high surface-to-volume ratio, they are better at relaxing strain.

Quasi-one-dimensional crystals, or NWs, have been used in a variety of exciting recent advances in photonics [87] [88] [89], photovoltaics [90] [49], electronics [91] [92], and other domains [93]. The distinct functioning of NWs is caused by a number of material properties, of which strain is a major one. The capacity of a compound to efficiently relax under strain determines the possibilities for mixing compounds of diverse lattice parameters and characteristics in the same NW. Mapping the strain in these nano-objects is very important since the composition of a single NW (such as a mismatched shell in core-shell structures) would have a significant impact on the strain of an upright-standing NW device.

The III V semiconductors are the ones, which are prepared from the elements of the group III and group V of the periodic table. The III-V nanowires are essential for the modern technologies, considering heir applications in electronics and opto-electronics industries, specifically in the development of transistors, LED systems, diode units, photo detectors and solar cells. Such NWs posses higher electron mobility properties and direct band gap nature, enabling efficient charge transport. Some of the key properties include 'enhanced carrier mobility', 'tunable emission control' and 'stronger light matter interaction'. The group III elements include 'B',Al',Ga' and 'N'. While group V elements include 'N', 'P', 'As' and 'Sb'. Gallium Arsenide (GaAs) Nanowires are one of the primary III V NW structures, which offers approximately 1.4eV direct bandgap properties. This NW can offer good emission properties in the infrared region, and thus are good solutions for opto-electronic applications. Indium Phosphide (InP) Nanowires are another type of direct bandgap III V NWs with approximate band gap of 1.35eV. These NWs offer strong absorption and emission in near infradred region and offer applications in telecommunications communication,

solar cells and quantum dot domains. Indium Arsenide (InAs) Nanowires offer very low direct bandgap of about 0.36eV with extremely high electron mobility, making it highly suitable for high speed electronic applications. Coordinate band hole III-V semiconductor nanowires, counting GaAs, InP, InAs, and GaN, display interesting electronic and optical properties that make them profoundly appropriate for a assortment of progressed applications in optoelectronics, high-speed gadgets, and vitality collecting. Their development strategies, custom-made to optimize quality and usefulness, are basic for saddling their full potential in both current and future mechanical headways.

4.2 Development of nanowires (NW)

This section is adapted from [94]. Because of their size-dependent characteristics, nanostructures have attracted a great deal of attention as quasi-one-dimensional NWs. Top-down and bottom-up approaches to "controlled NW development" include the two main categories of methodologies covered by current methodologies.

Using a top-down method, the crystalline material, that is already present on the substrate is etched in order to reduce the size of bigger microstructures and create NWs. Adatoms put on the substrate are combined to create the NW by a bottom-up method. Because it is more likely to result in nanostructures with fewer flaws, a more homogenous chemical composition, and improved short- and long-range ordering, the latter strategy is preferable to the top-down one. As a result, the majority of synthesis methods take a bottom-up strategy.

The two common NW growth mechanisms used in this thesis's projects are covered in the following sections: selective area growth using metalorganic vapour phase epitaxy (MOVPE), also referred to as metalorganic chemical vapour deposition (MOCVD), and vapor-liquid-solid (VLS) with metal catalyst particle using molecular beam epitaxy (MBE).

4.2.1 Growth of MBE using Au-catalyst

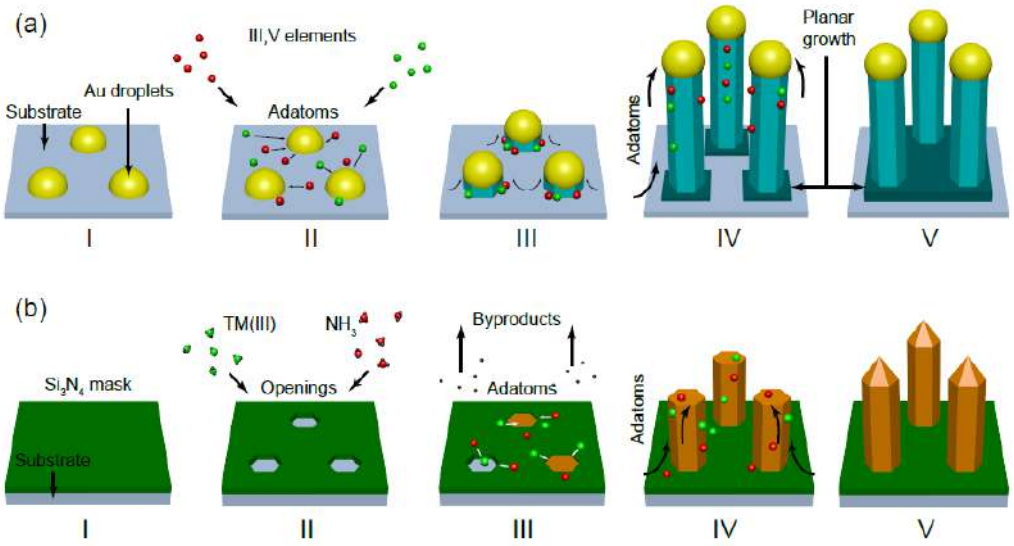

Figure 4.2: (a)Schematic illustration comparing the selective area and catalyst particle aided. (b) NWs' expansion [94].

When it comes to producing single-crystalline NWs in huge quantities, the VLS technique works incredibly well. Wagner and Ellis first invented the process in 1964 [95], and several research groups have since modified it to enable the growth of NWs from a wide range of materials, including III-V semiconductors. [96] [97]

The VLS method's schematic depiction is displayed in Fig. 4.2(a). A gold or other metal aerosol nanoparticle is first deposited onto the substrate to begin the process (see Fig. 4.2(a)-I). The particles enter the liquid phase when the temperature rises. The catalyst particle (II) allows the materials to diffuse through once they are introduced in the vapor phase. Crystal planes of the NW begin to form between the droplet and the substrate (III) as the concentration of material atoms exceeds supersaturation. The NW growth is raising the metal particle IV. Adatoms, or adsorbed atoms, are primarily responsible for the growth kinetics. They land straight on the substrate and proceed to the droplet at the tip by traveling along the NW walls. Furthermore, the III/V material grows planarly right on the substrate. The final stage of the growth process is the cooling and crystallization of the Au particle. With the catalyst particle at the top (V), the NWs remain perpendicular to the substrate [94].

4.2.2 Growth of catalyst-free MOVPE

Using a MOVPE technique, the InAs nanowire was produced on p-type Si (111) substrates. As group III and group V precursors, respectively, trimethylindium (TMIn), trimethylgallium (TMGa), trimethylantimony (TMSb), and arsine (AsH3) were employed. To get rid of impurities and native oxide, all Si (111) substrates were cleaned using the RCA (Radio Corporation of America) cleaning method and diluted HF (1:50). The substrates were placed into the MOVPE chamber after being dipped in hydrogen peroxide (H2O2) for 120 seconds, rinsed with DI water, and dried with N2 to initiate the reoxidization process. Substrates were heated to 700 °C for 10 minutes before being cooled to 400 °C in an H2 environment. After that, AsH3 was flown for 3 minutes to get the (111)B surface [98]. In general, the formation of InAs NWs was achieved by adjusting the growth temperature between 550 °C and 650 °C, while maintaining a set 150-second growth period. The flow rates of TMIn (2.9 × 105 moles/min) and AsH3 (4.5 × 103 moles/min) were also maintained. Pinhole-containing SiOx layer on silicon substrate has been used for both catalyst-free [99] and self-catalyzed nanowire growth processes. Typically, a few nanometer-thick SiOx layer is used to create it. The SiOx layer might be the native oxide layer of the Si substrate, several monolayers of oxidized Si, a thermal oxide layer, or an oxide layer transformed by organic chemicals [100].

When the temperature in MOVPE rises over 500 °C, the thin oxide layer on Si(111) turns extremely mobile and forms holes and clusters, according to B. Handl et al [101]. This indicates that more pinholes emerge in Si substrate with thin oxide when it is subjected to higher temperatures—annealing in our instance, for example, [102]. The substrate lattice will become air-exposed when the SiOx layer is sufficiently thin, allowing pinholes to pass through the oxide layer. The primary function of the SiOx layer is to act as a nucleation site, immobilize indium atoms, and alter the size and density distribution of indium droplets, also known as InAs islands, which aid in the development of nanowires. By adjusting the length of time spent dipping in H_2O_2, were able to manage the oxide thickness and produce a high yield of uniform InAs nanowires. Reoxidation has the benefit of producing an oxide layer on the Si substrate that is evenly covered. On the reoxidized Si substrate, InAs NWs with identical NW growth conditions exhibit an optimal shape with highly uniform InAs nanowires [103].

4.2.3 Crystal composition of NW's

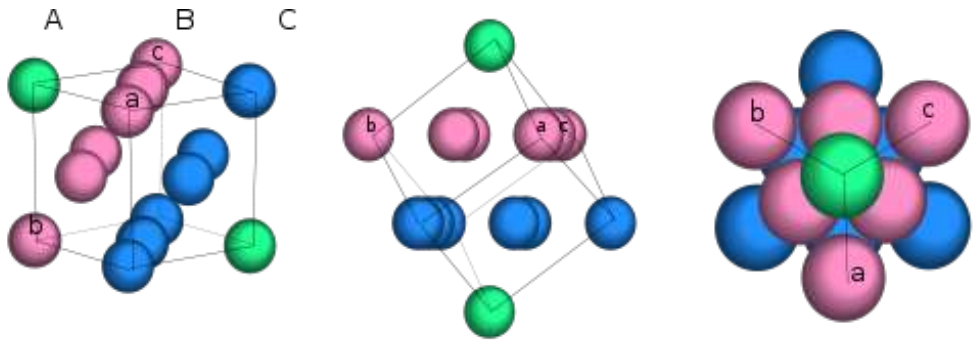

Figure 4.3: Explanation of cubic closest packing breakdown. Adapted with changes from [104].

Two popular crystal structures or polymorphs for III-V semiconductor NWs are Wurtzite (WZ) and Zinc-Blende (ZB). These two polymorphs are called sphalerite, or zincblende, and wurtzite. Zincblende is cubic in structure, but wurtzite has a hexagonal structure. It is distinguished by the preservation of a 1:1 zinc-to-sulfur ratio and single bonds between all of its atoms. Zincblende is characterized by a face-centered cubic, or cubic closet packing, (CCP) structure. In the figure 4.3, this crystal lattice structure is shown [104].

The hexagonal closest packing structure (hcp) of Wurtzite is typified by the presence of 12 ions in each unit's corners, which form a hexagonal prism (Fig. 4.4). In addition to growing defect-free InAs NWs, it is now feasible to modify the crystal structure of individual NWs by creating atomically sharp interfaces between the zinc blende (Zb) and wurtzite (Wz) structures.

4.2.4 Measurements of strain in NW's

The physical, chemical, and electrical characteristics of NWs may be investigated using a variety of thorough characterisation methods, including high-resolution scanning and transmission electron microscopy (SEM, TEM) [105], Raman spectroscopy (RS) [106], and different x-ray diffraction (XRD) techniques. The Raman inelastic scattering phenomenon, which occurs when the wavelength of scattered radiation experiences a shift matching to the optical phonons in the crystal, provides the basis for the RS technique [107]. A specialized spectrometer equipment and a concentrated optical laser beam are needed for the RS. The technique's implementation is quite

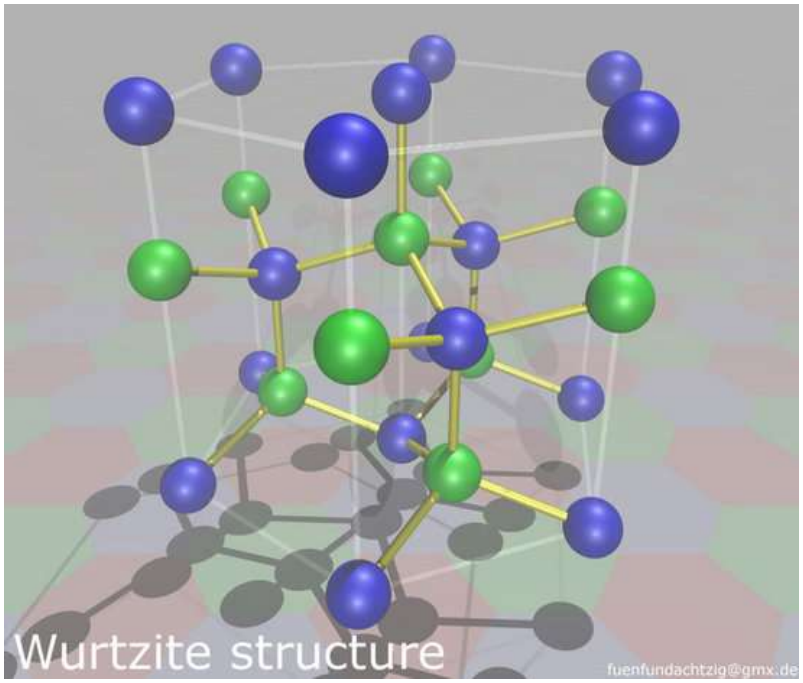

Figure 4.4: The wurtzite HCP structure. Adapted with changes from [104].

straightforward, but it has drawbacks such as indirect strain measurement and low resolution because of the large probe size [108].

Atomic resolution nanostructure characterization is made possible by methods based on electron diffraction [93]. The SEM offers a thorough analysis of an NW's surface. SEM does not, however, offer any details on the strain field. The High Resolution TEM (HRTEM) can provide the greatest spatial resolution images, down to individual atomic locations inside the crystal. High-resolution strain maps of the NWs may be obtained by combining geometrical phase analysis with the HRTEM [109]. The primary drawback of electron scattering methods is their ability to analyze only very thin materials, often less than 100 nm. As a result, in situations when the NW's initial state might change, a destructive sample preparation is required [110].

When compared to electrons, the high penetration depth of X-rays, for instance, enables structural characterization of thick objects at the nanoscale without requiring damaging sample preparation [111]. Contemporary third-generation synchrotron radiation facilities (see [139] for an example) are excellent sources of X-rays for characterizing NW structures. They produce coherent, brilliant, and steady X-ray beams that can be concentrated down to less than 100 nm in diameter [112], [113].

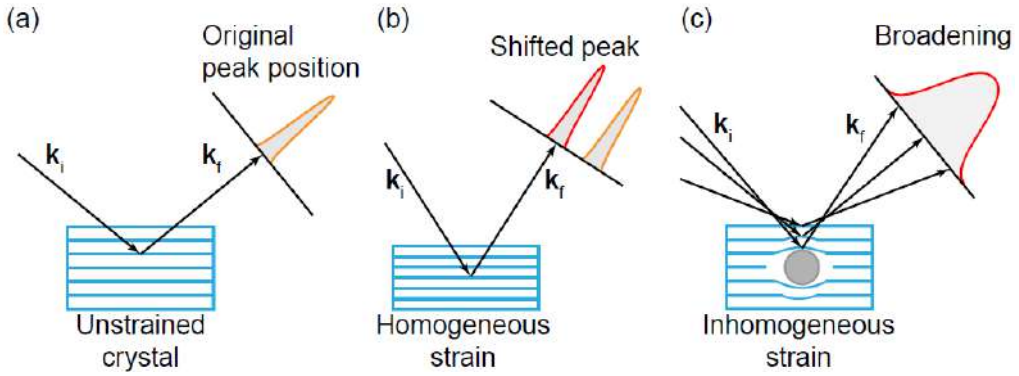

Figure 4.5: Effect of strain on the position of a Bragg peak. (a) Bragg reflection of a perfect unstrained crystal. (b) When homogenous strain is present, the Bragg peak shifts in relation to the unstrained condition. (c) An inhomogeneous strain causes the Bragg peak to broaden [94].

Average strain profiles of ensembles of nanostructures may be obtained by reciprocal space mapping. Although the resolution of scanning x-ray diffraction microscopy (SXDM) is constrained by the size of the beam, it may yield strain information for both ensembles of NWs [114], [115], [116] and individual nano-objects. With the latter method, the local strain distribution is determined by directly assessing the Bragg peak shifts at every position where the beam is positioned on the sample (refer to Fig. 4.5).

The following equation results from differentiating Bragg's law expression from Eq. (3.20) in relation to the angle

$$\frac{\delta d_{hkl}}{\delta \theta} = -\frac{\lambda cos\theta_B}{2sin^2\theta_B} \tag{4.1}$$

We are able to determine the relationship between the mechanical strain ε and the locations of the Bragg reflections from strained crystals because of this equation

$$\varepsilon = \frac{\delta d_{hkl}}{d_{hkl}} = -\frac{\delta \theta}{tan\theta_B} \tag{4.2}$$

5 A Synopsis of Piezoelectric Technology

5.1 Introduction

Materials technology has exerted such a significant influence on the history of human civilization that historians have designated separate historical periods by the materials that were prominent throughout these eras (e.g., the Stone Age, the Bronze Age, and the Iron Age). Today's well-designed, man-made engineering materials that outperform conventional materials, such as plastic and composites, are what define the Synthetic Materials Age, also known as the Engineering Materials Age. However, because they are often pre-processed and made to respond to a narrow range of external stimuli, these engineering materials and structures have been referred to be "dumb." These reactions are often not ideal under any one set of circumstances, but they are optimized to best meet the variety of scenarios that a material or structure may encounter [117].

The Smart Materials Age will begin to develop at the beginning of the 21st century due to the growth of various emergent technologies in recent years, including biotechnology, biomimetics, nanotechnology, and information technology [36]. Nonliving devices called "smart materials" combine sensing, actuation, logic, and control to react adaptively—typically in a repeated and helpful way—to changes in their state in the environment to which they are exposed. For a range of technical applications, smart materials are functional materials that are part of smart systems. They are capable of both perceiving and acting. If appropriately developed, many existing engineering materials may be used as actuator and sensor materials. These consist of conductive polymers, optical fibers, shape memory alloys, piezoelectric ceramics, and polymers. All of them are able to meet the unique criteria that the upcoming smart materials systems may have.

The general properties of piezoelectric materials are examined in this chapter. The chapter begins with a brief overview of history, which is followed by an explanation of the macroscopic and microscopic factors that support piezoelectricity. A broad overview of terminology based on the ferroelectric material's hysteresis behavior and various aspects of material processing are then provided. An examination of the linear mathematical theory of piezoelectric materials and the technological constraints on their use rounded up the chapter.

5.2 A quick overview of history: Piezoelectricity

This chapter is adapted from [117]. The Greek verb piezein, which means to press, is where the term piezoelectricity originates. The direct piezoelectric effect occurs when stress is applied to a piezoelectric crystal. This produces an electric polarization inside the material that is proportional to the strain's magnitude and sign. The opposite effect occurs when an elastic strain in the same material is produced by a polarizing electric field (converse piezoelectric effect). Actually, humans have been interacting with piezoelectricity for centuries. It is commonly known that early humans created fire by mechanically impacting flint, a kind of quartz. Since flint had excellent cutting qualities and could be used to make tools and weapons, it was really the primary material used throughout the Stone Age. It was quite by chance that the material's "lighter" quality was discovered when making tools. Prior to the development of matches, the substance was still being utilized as a lighter, striking iron later on. Nevertheless, a careful evaluation of the flint's unique and practical ability to start fires was not done.

Pierre and Jacques Curie conducted the first significant experimental study on piezoelectricity in 1880 [118]. The earliest evidence of this effect was found in single crystals, such as quartz. The final measurement of surface charges that emerged on carefully prepared crystals—among them, tourmaline, quartz, topaz, cane sugar, and Rochelle salt—that were put under mechanical stress was the focus of their investigations. However, the Curie brothers did not anticipate that crystals that showed the direct piezoelectric effect—electricity generated by applied stress—would also show the inverse piezoelectric effect, which is the result of applied stress responding to an electric field. Lippmann arrived at this feature by mathematical deduction from the basic principles of thermodynamics in 1881. The "converse effect" was promptly

experimentally verified by the Curies, who went on to acquire quantitative evidence of the total reversibility of electro-elastic-mechanical deformation in piezoelectric crystal. During World War I, the first significant application research on piezoelectricity devices was conducted. P. Langevin and his French colleagues started working on developing an ultrasonic submarine detector in 1917. Their transducer was housed in a submersible enclosure and included a mosaic of thin quartz crystals adhered between two steel plates, with a resonance frequency of around 50 kHz.

They succeeded in achieving their aim of sending out a high-frequency "chirp" underwater and timing the return echo by working on it after the conflict ended. Nonetheless, no industrialized country disregarded the strategic significance of their accomplishment, and ever since, sonar transducers, circuits, systems, and materials have all continued to be developed. The popularity of sonar led to a flurry of work in the creation of resonant and non-resonant piezoelectric devices of all types. It was at this time that the majority of the traditional piezoelectric applications—such as signal filters, phonograph pick-ups, accelerometers, ultrasonic transducers, bending element actuators, microphones, and more—were developed and put into use. It's crucial to keep in mind, though, that the materials accessible at the time—single crystals made of both natural and manmade materials—often restricted device performance and most definitely constrained economic exploitation.

Isolated research groups working on improved capacitor materials in the US, Japan, and the USSR during World War II found that some artificial polycrystalline anisotropic formations—like barium titanate, which is a polycrystalline—that were created by sintering metallic oxide powders exhibited dielectric constants up to 100 times higher than those of common cut crystals. The materials did not exhibit a macroscopic piezoelectric effect because of the thousands of small single crystals' randomly dispersed and macroscopically averaged distribution. But scientists did not realize until 1946 [119] that this kind of polycrystalline material—also referred to as ceramic ferroelectrics—could be produced piezoelectric by the introduction of an electric field, a procedure known as poling. Extensive research and development into piezoelectric devices was sparked by the discovery of this conveniently made piezoelectric material with astounding performance characteristics. The significant finding of the lead zirconate titanate (PZT) solid solution, which had enhanced piezoelectric characteristics, was published by Jaffe et al. in 1954 [120]. The main characteristic of PZT is its phase diagram, which shows a barrier between a tetragonal

and a rhombohedral phase with a zirconate concentration of around 52%. This boundary is called the morphotropic phase boundary (MPB). This characteristic, which is utilized in commercial compositions, makes apps easier to use in a variety of contexts. The PZT's general qualities have been examined by analyzing various compositions and adding additional elements to the fundamental PZT.

Uniaxially drawn polyvinylidene fluoride (PVDF) was shown to have high piezoelectricity and pyroelectricity in 1969 after being poled in an appropriate electrical field. It is also known that, while not as strongly as PVDF, other plastics, such as nylon or PVC, exhibit the piezoelectric effect. Numerous innovative materials have been the subject of piezoelectric studies since the early 1980s. The future is bright for composites made of ceramics and polymers, as well as grain-oriented glass ceramics, which are composites made of a glassy phase and one or more crystalline phases.

5.3 Piezoelectric effect

Mechanical quantities like stress (σ) or strain (ϵ) and electrical values like electric field (E), electric displacement (D), or polarization (P) are connected in crystals with piezoelectric characteristics. We refer to this process as electromechanical coupling, (refer to Appendix for more details)

5.3.1 Direct and Indirect impacts

As schematically shown in Fig. 5.1 [121], the piezoelectric effect, also known as piezoelectricity, is the creation of electric charges on the surface of some non-conducting materials in response to applied mechanical stress, or, on the other hand, the creation of a mechanical strain in such materials when they are exposed to an electric field. Because the mechanism of the piezoelectric effect is reversible, materials that display the direct piezoelectric effect also display the converse piezoelectric effect. Therefore, although the term "piezoelectricity" frequently refers to the direct piezoelectric effect of the internal creation of electrical charges as a result of an applied mechanical force. Piezoelectricity is also used to refer to both direct and converse effects.

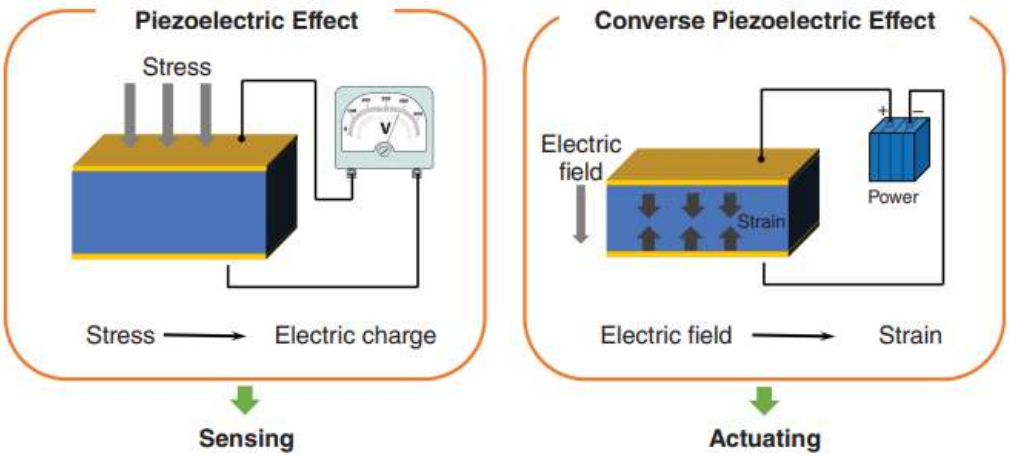

Figure 5.1: (a) When mechanical stress is applied, the direct piezoelectric effect produces an electric charge; (b) the converse piezoelectric effect represents the scenario in which strain occurs when an electric field is applied [121].

Direct Piezoelectricity may be defined as the induced polarization due to the applied mechanical stress. This effect can be mathematically defined in a linear relation such that the 3 components of the polarization (P_i) are linear combinations of the 9 components of the stress tensor (σ_{jk}). The polarization and the strain tensor are related via the property of the material, known as the piezoelectric strain constant (d_{ijk}), and mathematically given as: [122].

$$P_i = d_{ijk} \cdot \sigma_{jk}. \tag{5.1}$$

When the induced polarization is solely due to the applied mechanical stress, one can define the electric displacement as a result of direct polarization, as follows:

$$D_i = d_{ijk} \cdot \sigma_{jk}, \tag{5.2}$$

where i,j,k = 1,2,3. The piezoelectric strain tensor has a total of 27 components. However, utilizing the symmetry of the stress tensor, one can reduce the (d_{ijk}) tensor as well. When contracted, the jk indices of the (d_{ijk}) are contracted as per the strain tensor. Eq(5.2) can be further written as:

$$D_i = d_{il} \cdot \sigma_l, \tag{5.3}$$

where, i =1,2,3 and l = 1,2,....6, and the contracted tensor has now 18 components, as a 3×6 matrix.

On the other side, the "converse" piezoelectric effect is defined as the application of the electric field, inducing mechanical strain within the piezoelectric material. In this scenario, we have another linear relationship, with the same piezoelectric strain constant, mathematically given as:

$$\epsilon_{jk} = d_{ijk} \cdot E_i, \tag{5.4}$$

where i,j,k = 1,2,3 and the contracted tensor is further given as:

$$\epsilon_l = d_{il} \cdot E_l. \tag{5.5}$$

For instance, the d_{31} constant resembles the electric displacement in the '3' direction (or 'z' direction), caused by the stress applied in the '1' or 'x' direction. Similarly, the converse piezoelectric effect resembles the induced strain in the 'x' direction due to an electric field applied in the 'z' direction. One can also comment on the directional nature of the piezoelectric effect. Reversing the direction of the applied field also reverses the direction of the induced mechanical deformation. [122]

In specific design scenarios, several types of piezoelectric constants are employed in addition to the piezoelectric charge or strain constant. Together with the previously described piezoelectric charge or strain coefficient (d), there are a total of four piezoelectric constants. [123]. Partial derivatives determined under constant strain, constant electrical field, constant electrical displacement, or constant stress are the definitions of these piezoelectric constants. These states are referred to as "open circuit," "short circuit," "mechanically free," and "mechanically clamped," in that order. For further understanding of mathematical relations for piezoelectric materials, refer Appendix.

5.3.2 Contribution of Ferroelectric Properties to Piezoelectricity.

Reviewing ferroelectric characteristics and their role in piezoelectricity is important since the majority of high-performance piezoelectric materials are also ferroelectric materials [122]. Certain materials exhibit ferroelectricity, which is the ability to

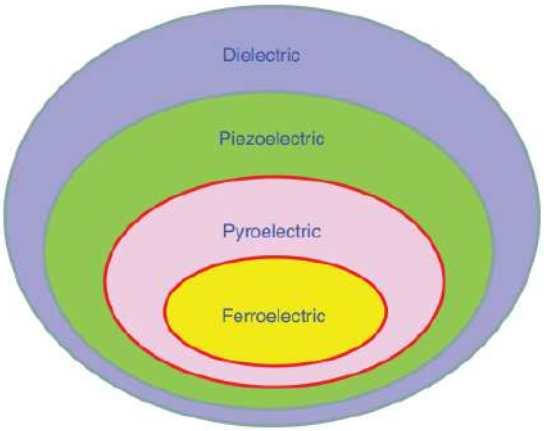

Figure 5.2: Connection between materials that are dielectric, piezoelectric, pyroelectric, and ferroelectric [122].

reverse their spontaneous electric polarization with the introduction of an external electric field. Ferroelectrics are the core subset of dielectrics, as seen in Fig. 5.2. Dielectrics are a large family. When put across the plates of a capacitor, dielectric materials—basically electrical insulators—become polarized due to the peripheral application of the electrical field. Although stress can result in a net separation of positive and negative charges in a piezoelectric crystal with a non-centrosymmetric crystal structure, piezoelectric materials are members of the dielectric group.

Because a temperature change can thermally alter the polarization magnitude in a pyroelectric crystal, pyroelectric materials are those that can produce a temporary voltage when heated or cooled. In contrast, polarization changes in a piezoelectric crystal are caused by mechanical stimulation, which leads to the accumulation of charges at the crystal's surfaces. A subclass of pyroelectric materials used in experiments is called ferroelectrics. Not all ferroelectric materials are pyroelectric, just as not all pyroelectrics are piezoelectric. On the other hand, not all piezoelectric materials are pyroelectric. It is established that the aforementioned classification is controlled by crystal symmetry. Every crystalline material falls into one of the 32-point groupings known as crystallography. Ten ferroelectric point groups and twenty piezoelectric point groups are present.

While an electric field may reverse the orientation of an electric dipole in ferroelectric materials, it cannot be altered in piezoelectric, pyroelectric, or ferroelectric materials. Consequently, the ability of ferroelectrics to reverse spontaneous polarization in the opposite direction with a high enough applied electric field is what sets them apart.

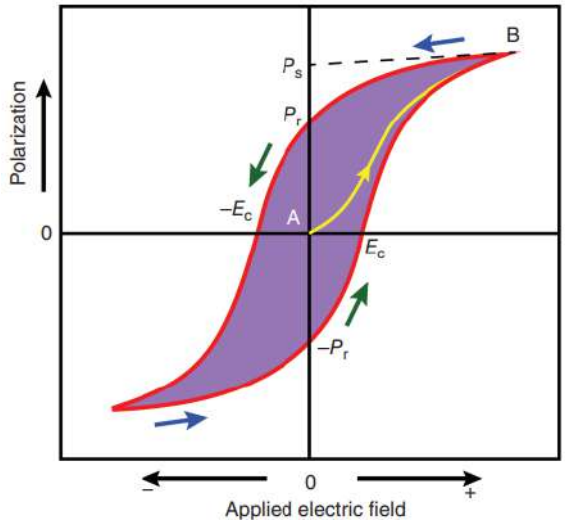

Figure 5.3: Ferroelectric materials: polarization against the hysteresis loop of the electric field [122].

Moreover, as Fig. 5.3 illustrates, polarization depends on both the electric field and the material's past experiences, producing a hysteresis P–E (polarization-electric field) loop. When the applied field is high enough, the polarization from point A starts to grow steadily with the E-field and eventually becomes extreme. The polarization then achieves a saturation level (saturation polarization, P_s) during an extended and gradual stage. Normally, the saturated linear component and the polarization axis coincide to estimate the P_s. After the E-field is removed, the polarization does not return to its initial state; rather, it produces non-zero values, or residual polarization, or P_r. An E-field applied to $i{+}n$ in the opposite direction is necessary to achieve a zero polarization condition. The coercive field, or E_C, refers to the strength of the applied electric field that reverses the direction of ferroelectric polarization and is the name given to this E-field.

One crucial factor in determining whether a material is ferroelectric is the presence of a P-E loop. Because the reaction of electric domains to an electric field is similar to that of ferromagnetic material's magnetic domains against a magnetic field, ferroelectric materials exhibit such hysteretic behavior. It is important to note that even in the presence of extremely strong external electrical fields, a polar material may be piezo- or pyroelectric but not ferroelectric if the orientation of its dipoles cannot be switched. One typical piezoelectric material that lacks ferroelectric characteristics is single-crystalline quartz. In a similar way, ZnO is often non-ferroelectric but piezoelectric.

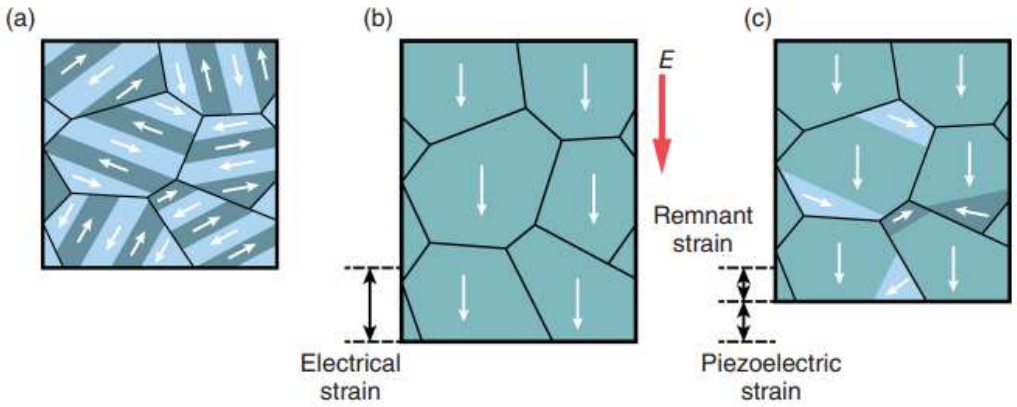

Figure 5.4: Graphic representations that demonstrate how the ferroelectric domain aligns with the macroscopic stresses that occur when an electric field is applied to a ferroelectric material during poling. (a) The Virgin State. (b) State of saturation. (c) State of remnants [122].

Polarization occurs when a ferroelectric crystal cools below the Curie temperature. A structural phase transition known as the ferroelectric phase transition occurs when ion displacements cause lattice distortions and change the crystal's symmetry. For a particular crystal structure and composition, the amplitude of the ion displacements along certain crystallographic axes in the materials varies. A depolarizing electric field will result if the polarization spreads evenly over the whole crystal. The crystal typically breaks into areas known as domains—a region in which the polarization is uniform—in order to reduce the electrostatic energy related to this field. Domain walls are the areas that divide two adjacent domains. Usually, their thickness ranges from 10 to 100 Å. A domain is an area of a ferroelectric material where the polarization is homogeneous in one direction. The total polarization in an extreme condition, where (almost) all domains are aligned along the direction of the applied electric field, is known as saturation polarization, or P_s. The remaining polarization results from certain of these domains continuing in the same direction even after the electric field is removed. Given that ferroelectric materials may produce electric charges in response to mechanical stress, it is conceivable that they might be employed as piezoelectric materials in a condition where they still exhibit residual polarization. In simpler terms, if a ferroelectric material has not been exposed to an electric field, then polycrystalline bulk materials should not exhibit a piezoelectric response. This is because in the event that the domains are randomly distributed in various directions, all of the charges will be dismissed together, leading to zero change when the material as a whole experiences mechanical deformation. Therefore, one of the properties of ferroelectric materials is piezoelectricity, and

generally speaking, ferroelectric materials must be poled in order to be employed as piezoelectric materials. For ferroelectric piezoelectric materials, electrical poling is therefore an essential procedure.

When ferroelectric materials are poled, a high electric field is applied across them; as a result, most of the domains lose their original polarization and align along the direction of the electric field. The polling procedure is schematically depicted in Fig. 5.4. An electric field is applied to the virgin materials, and it should be high enough relative to the coercive field (E_C to allow the domains to reorient almost in the same direction). The expansion of the poled materials or tensile stresses occurs during the poling process, as seen in Fig. 5.4(b), and this is essentially consistent with the converse piezoelectric phenomena. Fig. 5.4(c) illustrates how, in order to lessen mechanical stresses, certain domains reverse or shift in orientation when the poling electrical field is removed, even if the majority of the domains remain along the poling direction. The material has a macroscopic polarization following the poling treatment, which is equivalent to the residual polarization P_r in the previously described P-E loop. Thus, for piezoelectric materials, the poling process is crucial. The following piezoelectric characteristics, particularly the piezoelectric charge coefficient (d_{33}, will be extremely low even for identical materials if they are not fully poled). Furthermore, it is evident that non-ferroelectric materials cannot be processed using the poling method. For this reason, ferroelectric materials are first required for high-performance piezoelectric materials.

5.3.3 Piezoelectric Studies of $HfZrO_2$ in Nanostructured Devices

For many years, HfO_2 and ZrO_2 material systems (refer to Figure 5.5) have been researched and applied. HfO_2, for example, is employed in CMOS technology as a high-$\varkappa$ dielectric material for field-effect transistor (FET) gate insulators and dynamic random access memory capacitor insulators. Oxide fuel cells employ ZrO_2 doped with Y, commonly referred to as yttria-stabilized zirconia. Ferroelectricity was, however, found in Si-doped HfO_2 and oxides solid solution $Hf_{0.5}Zr_{0.5}O_2$ (HZO) in 2011. Since then, as new applications are made possible by the ferroelectric characteristics of these materials, the global community of researchers working on HfO_2 and ZrO_2-based systems has continued to expand. [124] A new field of use for ferroelectric $Hf_{1-x}Zr_xO_2$ has emerged recently. There is a fundamental limit to how effectively the gate voltage may block the current flow through the channel of a

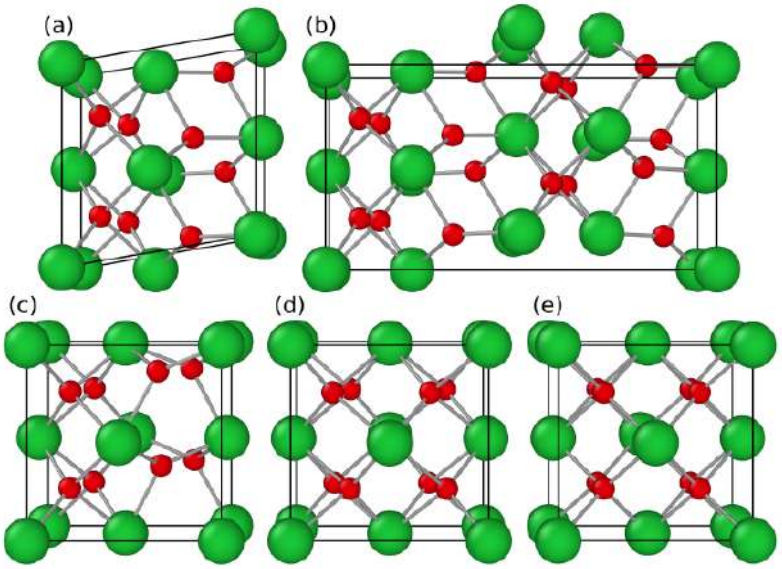

Figure 5.5: Crystal phases of HfO_2 and ZrO_2 are arranged as follows: (a) monoclinic; (b) orthorhombic; (c) polar orthorhombic; (d) tetragonal; and (e) cubic. Atoms of metal and oxygen make up the green and red spheres, respectively. [124]

FET, an indispensable basic building element of today's semiconductor industry. A FET functions as a switch with clearly defined "on" and "off" states.

Systems of $Hf_{1-x}Zr_xO_2$ materials also show electrocaloric, pyroelectric, and piezoelectric phenomena. The pyroelectric effect's physical inverse is known as the electrocaloric effect. They both connect the electrical and thermal domains and are crossover effects, much like the direct and converse piezoelectric effects. The way that the residual polarization changes as temperature changes is explained by the pyroelectric phenomenon.

Piezoelectricity and antiferroelectricity in $Hf_{1-x}Zr_xO_2$

The twofold hysteresis loop seen in experiments is a manifestation of the antiferroelectric-like behavior in $Hf_{1-x}Zr_xO_2$. For example, the Si-doped HfO2 and $Hf_{1-x}Zr_xO_2$ with x near to 1 exhibit the double hysteresis loop. This is most evident in pure ZrO_2. [125] The alternating configuration of the electric dipoles in a crystal is the atomistic source of antiferroelectricity. In $Hf_{1-x}Zr_xO_2$, the antiferroelectric phase is proposed to be the o-phase [53], but this phase happens at high pressure. The O-phase, or orthorhombic phase, is a specific crystallographic phase characterized

by an orthorhombic crystal structure. In materials science and solid-state physics, the term "O-phase" is often used to describe this particular arrangement of atoms within a crystal lattice. The T-phase, or tetragonal phase, refers to a specific type of crystallographic structure where the unit cell of a material is shaped like a rectangular prism, with two of its axes of equal length and the third axis of a different length. This structure is particularly important in the context of ferroelectric and piezoelectric materials. The P-O-phase, which stands for the "pseudo-orthorhombic" phase, is a term used to describe a specific crystallographic phase that is closely related to the orthorhombic phase but may have some distortions or deviations that make it not perfectly orthorhombic. Similar to perovskite antiferroelectrics, the general explanation for the antiferroelectric-like behavior in this material system is the electric field-driven phase shift from the paraelectric t-phase into the ferroelectric p-o-phase [126]. Furthermore, the p-o-phase needs to be inducible from the t-phase through the electric field. This implies that, in the first approximation, there needs to be a surmountable energy difference between these two phases.

Applications for the piezoelectric $Hf_{1-x}Zr_xO_2$ material system include resonators, actuators, sensors, transducers, and more. This material system attribute seems to be the one that has received the least attention yet. Piezoelectric coefficients for Si-doped HfO_2 have recently been published [127], with $d_{33} = 19.8pmV^{-1}$ and $d_{31} = 11.5pmV^{-1}$. Piezoelectric coefficient $d_{33} = 10pmV^{-1}$ was observed for both undoped and Mg-doped ZrO_2 [128]. According to the authors of these studies, the crystal volume shift that occurs during the electric field-induced transition from the t-phase to the p-o-phase accounts for the piezoelectric activity in each of their situations. In case of commonly used material lead zirconate titanate (PZT) has the piezoelectric coefficients as $d_{33} = 60 - 130pmV^{-1}$ and $d_{31} = -120pmV^{-1}$. [129]

5.3.4 Finite Element Method (FEM)

A numerical approach known as the finite element method (FEM) may be used to solve problems that can be expressed as functional minimization or as partial differential equations. An assembly of finite components is used to represent a domain of interest. Finite element approximating functions are found in terms of the desired nodal values of a physical field. An unknown nodal value discretized finite element issue is derived from a continuous physical problem. A system of linear algebraic equations has to be solved for a linear scenario. Nodal values can be used to retrieve

values contained within finite elements. Two noteworthy aspects of the FEM are as follows: 1) Even with basic approximating functions, piece-wise approximation of physical fields on finite elements yields high precision (by increasing the number of elements, we can reach any precision). 2) For a discretized issue, the locality of the approximation results in systems of sparse equations. This aids in the resolution of issues with a significant number of nodal unknowns [130].

The need of the FEM

Real world structures are complex in nature, and require analysis in a much more refined manner. FEM analysis enables the users to discretize the structures into smaller segments, making it possible to analyze complex interactions across smaller elements. FEM analysis also allows us to well investigate heterogeneous structures where different segments of the prototype exhibits different material properties. This helps the users to understand the dynamic response of different materials under different operating conditions. FEM analysis also enables the users to achieve the study of non-linear behavior, which often involves nonlinearities due to large deformations, material plasticity, and contact problems. FEM can well handle such non-linear responses while working as iterative solution solver. The similar level if democratization can be performed over the time scale, where the structural response is then analyzed at each instant of the time frame, where the operating conditions can be tuned differently for each time frame. Therefore, the use of FEM in dynamic analysis is as a result of the complications and the protracted nature of the real life engineering problems. The capability of ANSYS to handle geometries, material composition, nonlinearity, time variation, and multiphysics is the key feature that makes this software useful to engineers and researchers. Thus, the usage of FEM allows for the better understanding of structures' behaviour as well as the development of more efficient, safer and more reliable engineering solutions.

The functioning of the FEM

The essential steps of the finite element solution approach are listed below to provide a broad overview of how the finite element method works.

Discretize the continuum: Splitting a solution area into finite components is the initial step. The preprocessing software usually creates the finite element mesh.

Nodal coordinates and element connectivities compose the majority of the arrays that make up the mesh description.

Select interpolation functions: To interpolate the field variables across the element, interpolation functions are employed. Polynomials are frequently chosen to serve as interpolation functions. The number of nodes allocated to each element determines the polynomial's degree.

Find the element properties: It is necessary to develop the matrix equation for the finite element that links various parameters to the nodal values of the unknown function. Several techniques can be applied to this problem; the variational approach and the Galerkin method are the most practical.

Assemble the element equations: We must put together each element equation in order to determine the global equation system for the entire solution region. In simpler terms, all of the discretization-related local element equations need to be combined. The assembly method takes advantage of element connectivities. Boundary conditions, which are not taken into consideration in element equations, should be enforced prior to solution.

Solve the global equation system: Typically, the finite element global equation system is positive definite, symmetric, and sparse. There are direct and iterative approaches to problem-solving. The solving process yields the nodal values of the requested function.

Compute additional results: We frequently need to compute extra parameters. For instance, strains and stresses—which are found when the global equation system is solved—as well as displacements are important in mechanical difficulties. [130]

COMSOL Multiphysics and FEM

Based on the finite element approach, COMSOL Multiphysics is a general-purpose simulation program for multi-field issues. By using the built-in interfaces or creating user-defined physics, this program allows the combination of several physics. The generic framework for the continuum mechanics-based study of solid bulk is provided

by the Solid Mechanics module. As a result, this method requires that the created mesh comply with the interface bounds and explicitly model the discontinuities in the solution domain. This is conceivable by making use of COMSOL's intriguing feature, which gives users access to field variable definitions (such as stress and strain fields). A number of internal variables and functions (such as path and domain integration tools) in COMSOL Multiphysics are essential to carrying out the suggested FEM study. These choices are mostly used to carry out the pre-processing (like level set calculation) and post-processing tasks in addition to realizing the enrichment idea [131].

There are some key features of COMSOL Multiphysics:

1. **Multiphysics Modeling:** The capacity of COMSOL to handle coupled or multiphysics phenomena—in which two or more physical processes interact—sets it apart. Accurately replicating real-world phenomena, such as piezoelectric effects, fluid-structure interaction, or electromagnetic heating, requires this capacity.

2. **User-Friendly Interface:** Through the modeling process, from geometry creation and physics setup to mesh generation, solution, and post-processing, it provides a graphical user interface (GUI) that leads users through the experience.

3. **Customizable and Extensible:** Equations and expressions can be added to COMSOL models by users to suit their own needs. Because of the software's versatility, user-defined physics may be added, or current models can be improved.

4. **Wide Range of Application Areas:** Applications for COMSOL Multiphysics cover a wide range, such as fluid, thermal, chemical, acoustic, mechanical, and electrical processes.

5. **Module-Based Software:** Numerous modules that focus on certain application domains, including RF, wave optics, microfluidics, structural mechanics, and chemical engineering, among others, may be added to the basic platform.

6 Experimental Results

6.1 Overwiew

For initial experimental analysis, I was involved in the experiment at NanoMax beamline at MAXIV synchrotron in LUND, Sweden, and Coherence Application beamline P10 at PETRA III, Hamburg, Germany. In MAXIV, we performed the experiment on the Hafnium Zirconium oxide (HZO) samples, which are over the InAs-substrate. However, at PETRA III, the experiment was performed on the InAs III-V NW samples, which were covered by the HZO layer. In this work, we will demonstrate that annealed HZO films formed on III-V semiconductor substrates and NWs, particularly InAs, have a piezoelectric effect. The films were electrically driven while also being observed in an X-ray beam. To determine the strain impact of the HZO on the nanowires, the strain in oxide-covered III-V NWs will be measured, and the change as a function of an applied voltage to the oxide was observed. This should confirm the HZO - III-V NW system's excellence as a platform for operando research on strain variation. Optical and ultrafast dynamics observations were integrated with X-ray measurements.

Figure 6.1: An overview of an automated stage, detectors, data collection system, and other scientific equipment used in a high-precision material analysis facility PETRA-III P10.

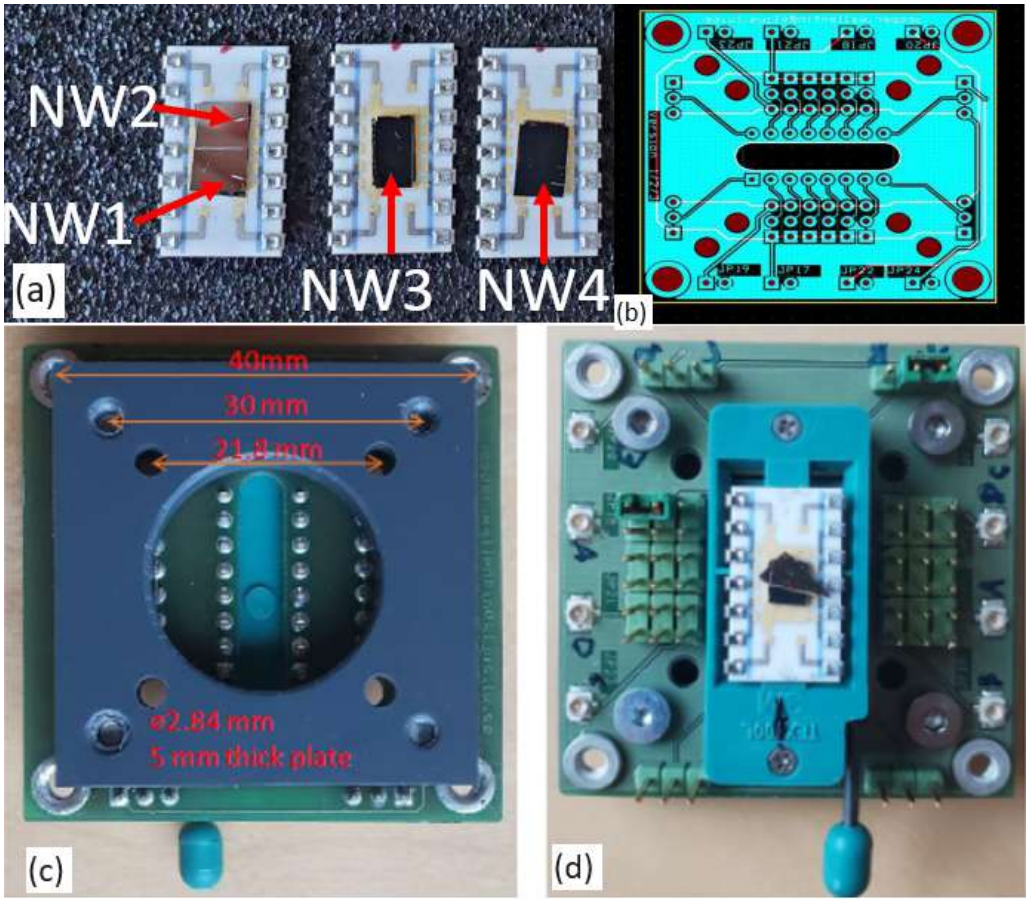

Figure 6.2: Illustration of the samples that were used in the experiment: (a) four nanowire samples with the labels NW1 to NW4, (b) an electrical connection diagram for the circuit board, (c) an image of a sample holder with its exact measurements marked, and (d) a nanowire sample positioned at the sample holder. Moreover, the actual dimensions of the sampler holder are marked in Fig. 6.2(c) and our final prepared NW sample along with the holder is shown in 6.2(d).

The NWs were fabricated at Lund University with a diameter of 100 nm and length of 2 µm using metal-organic vapor phase epitaxy. After the growth, several NWs were removed from the substrate and positioned on a (111) Si wafer. HZO was deposited on the substrate using atomic layer deposition (ALD). The piezoelectric effect was initially quantified using planar samples of HZO mounted on III-V substrates with a top TiN electrode. The piezoelectric effects in an NW sample were then investigated using InAs NWs coated with HZO and a TiN electrode. The HZO films were 10 nm and 50 nm thick, while the NW was 100 nm in diameter (strongest coefficients at 10 nm, but easier to see in thicker films). Prior to the X-ray measurements, optical absorption and electrical transport measurements of the film and NW were made

concerning the voltage applied to the film. Electrical measurements were made as the piezoelectric effect was created by applying a voltage across the film, in addition to the X-ray observations. Before and after the X-ray tests, electrical measurements were made. To examine the strain field of a single NW, a very spatially coherent X-ray beam had to be focused on it down to micrometer size. The energy of the X-ray photons was 13 keV. A six-circle diffractometer was required to do 3D measurements. To demonstrate structural changes in NWs used in devices, we wanted to integrate electron microscopy, electrical and optical device measurements, and X-ray coherent scattering methods with X-ray nano-beams. As a function of applied voltage, we aimed to connect the piezoelectric effect in annealed HZO films with simultaneous strain measurements in oxide-covered III-V NWs.

Different samples were analyzed during this experimental analysis. The details of the samples that were used in this thesis are highlighted in Fig. 6.2. In Fig. 6.2, all the samples are mentioned and numbered accordingly. In Fig. 6.2(a), samples are numbered "NW1", "NW2", "NW3", and "NW4". The chip design that is used to mount the samples on it is shown in Fig. 6.2(b), which includes the connections provided in order to supply the potential and ground signals.

6.2 Experimental studies at NanoMax

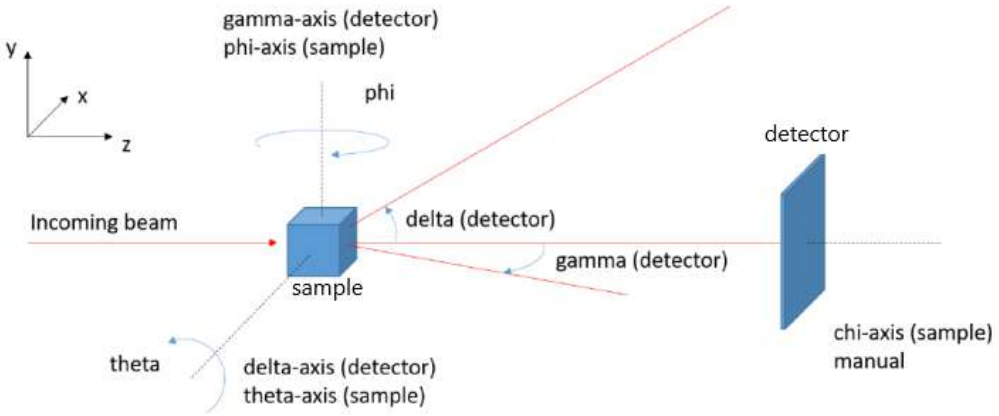

Figure 6.3: Represents the experimental geometry.

The initial analysis of the sample was first performed at NanoMax, MAXIV, Lund, Sweden. The operating energy was 13 KeV while the data was recorded at the Merlin

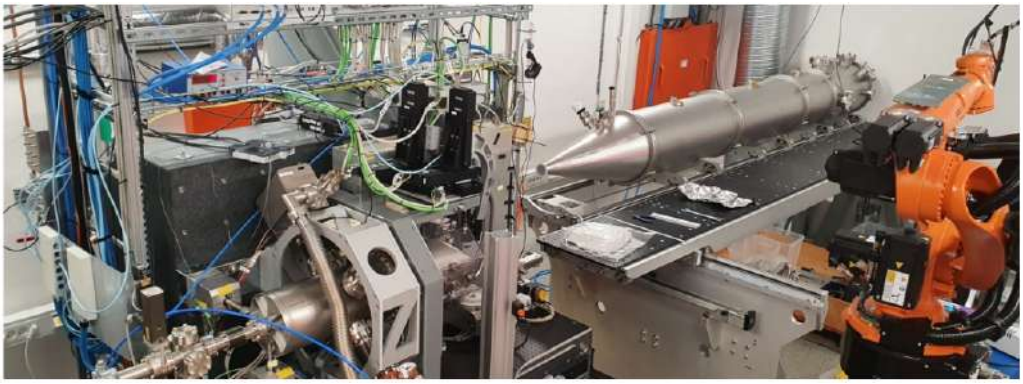

Figure 6.4: An overview of an automated stage, detectors, data collection system, and other scientific equipment used in a high-precision material analysis facility NanoMax, MAXIV.

detector with a pixel size of $55\mu m \times 55\mu m$. The experimental geometry is given in Fig. 6.3.

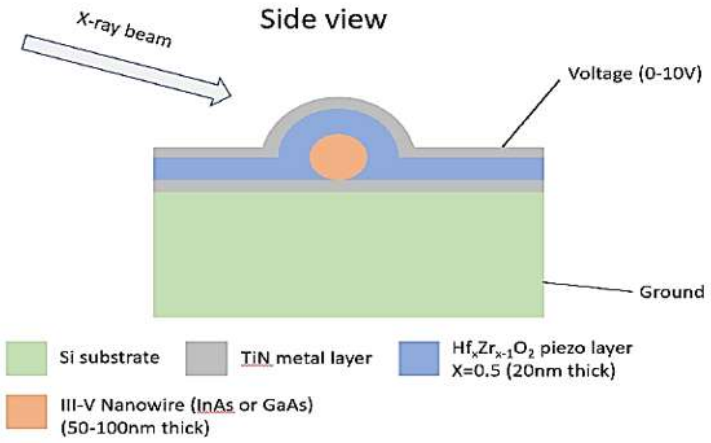

Figure 6.5: Shows the side view of the proposed design of the sample under investigation.

Fig. 6.3 graphically resembles the experimental setup during the analysis at NanoMax, MAXIV. Whereas Fig. 6.4 shows the on-site experimental setup at the MAXIV site. During the analysis of the dataset retrieved from the experiment at MAXIV, both the X-ray diffraction and x-ray fluorescence maps were investigated. To understand the sample better, Fig. 6.5 shows the side view sample under investigation. The ideal sample shows the NW structure with an approximate thickness of 50–100 nm, which is placed over the TiN layer of thickness 10 nm. The 20-nm-thick piezo HZO layer covers the NW and Tungsten contact is finally provided at the top for applying

potential cycles. The Si substrate has an approximate thickness of 60 nm, while the voltage is given via the Tungsten contact. As visible from Fig. 6.5, the NW is not covered by HZO from the side edges. This proposed sample design would also be our reference while modeling and analyzing the sample using COMSOL (as mentioned in later stages).

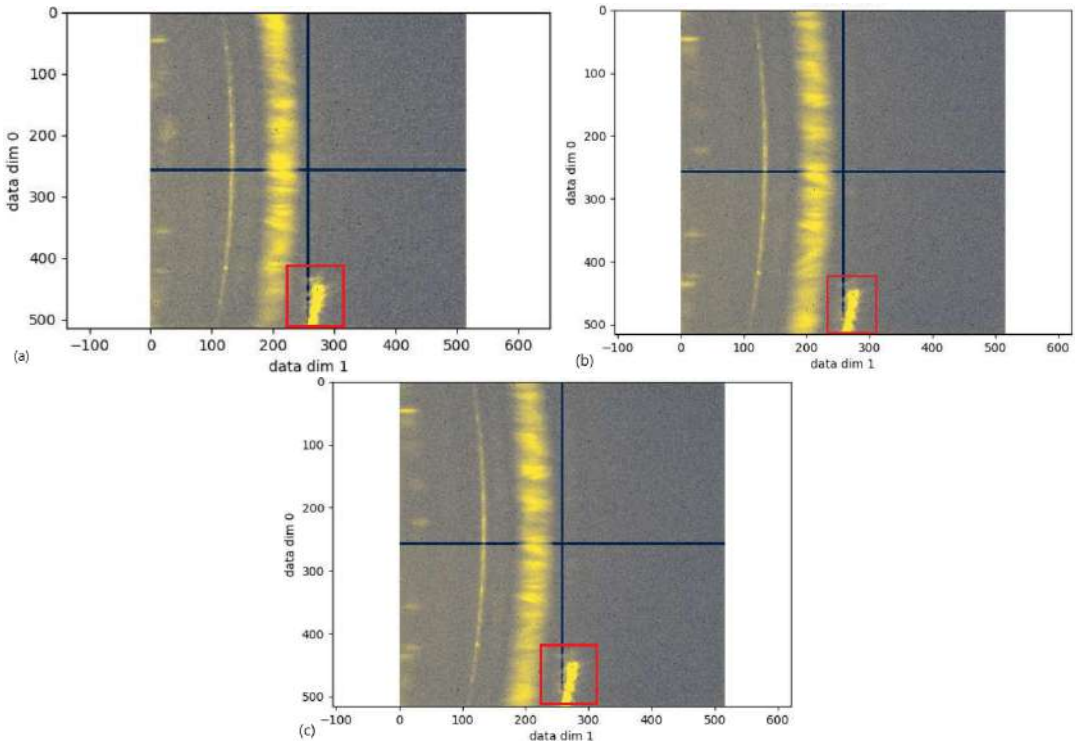

Figure 6.6: Diffraction pattern of nanowire observed at 0 V (a), the pattern at 1 V with a current rating of 1.6 µA (b) and Diffraction pattern at 2 V with a current rating of 14 µA (c).

The XRD results from the NW sample are shown in Fig. 6.6. The figure shows three different voltage levels applied: 0 V, 1 V, and 2 V. Interestingly, a highly dominant powder ring is observed, which could certainly minimize the peak from the NW itself. The amorphous behavior of the diffraction peak (big ring in Fig. 6.6) could be from the HZO material itself. We were only able to retrieve the HZO data in NanoMax. Due to its complicated crystal structure, we conducted the experiment again at PETRA III and obtained the data for InAs NW, whose crystal structure is much simpler than that of HZO. However, understanding the induced strain dependence over the applied voltage over the sample structure would require analyzing the change in the diffraction peaks from the NW structure. Therefore, a dominating diffraction ring would certainly make the analysis from the NW peaks much more complex.

The highlighted red area in the diffraction map could possibly arise from the NW response. However, as mentioned before, the diffraction results are highly complex in nature due to the possible overlapping of the diffraction peaks from the NW and HZO structures and the highly minimized peaks from the NW sample, as observed in the figure. These results thus bring out the need to re-perform the experimental study, and thus, the next analysis was performed at PETRA III. Choosing another synchrotron facility for our next experimental analysis was essential, as this would enable us to confirm the results retrieved at the NanoMax MAXIV. However, one of the targets of choosing PETRA III was to re-conduct the experiment with the aim of observing the NW response prominently.

6.3 Experimental studies at PETRA III

The experiment was conducted at P10 Coherence Application beamline, PETRA III, Hamburg, Germany. The X-ray photon of energy 13.1 KeV hits the sample and diffraction occurs at the detector, Eiger 4M, and the distance between the sample and detector was 1.8 m. A highly spatially coherent X-ray beam focused on the NW down to 1 µm in size. The retrieved data is then analyzed to understand the strain variations in the InAs nanowire (NW) due to the piezoelectric effect of HZO by applying a voltage across the sample. The diffraction patterns were recorded in samples at different voltage cycles. These patterns are shown in Fig. 6.8. The analysis shown specifically in Fig. 6.8 was performed over the NW4 sample (refer to Fig. 6.2). Experimentally, two different cycles of the voltage variations were applied: the first is the series of 0 V, 4 V, and 0 V, and the second is the sequential voltage cycle of 0 V, 1 V, 2 V, 3 V, 4 V, and 5 V. Fig. 6.8 specifically highlights the diffraction maps of the NW4 sample at cycles 0 V, 4 V, and 0 V. The ROI highlighted in each pattern shows the 2D space across which the NW peak was visible, and the analysis is performed across this ROI only. This ROI-based analysis enables data reduction and faster computations. Moreover, based on preliminary visual analysis, one does not observe voltage-dependent variations. In simpler terms, one does not observe any evident back-forth change in diffraction peaks as the voltages range from 0 V to 4 V. This is further observed from the rocking curve retrieved from the diffraction patterns at different voltage cycles. Fig. 6.9, showing the consolidated rocking curve at different ω positions for NW4 at 0 V and 4 V cycles, further confirms that we do not find reversible behavior in the intensity profile as we switch the voltage from 0 V to 4 V and then back to 4 V. However, the rocking curve at each applied voltage

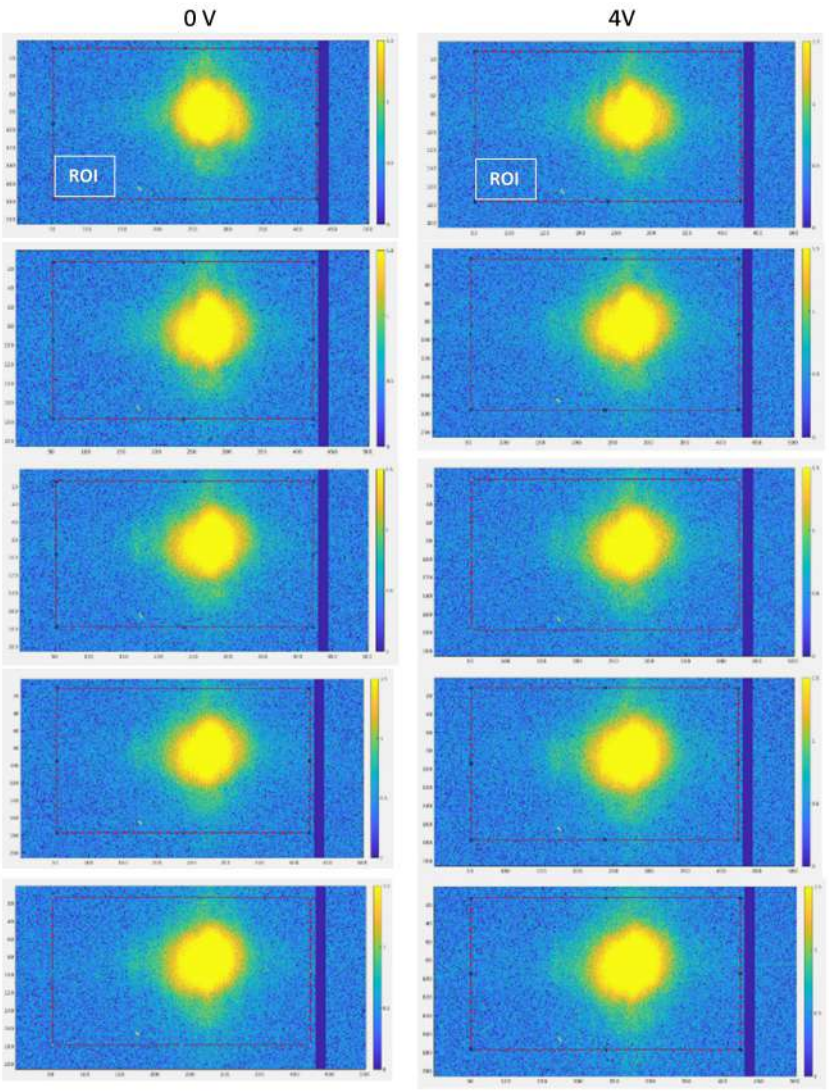

Figure 6.7: Represents the diffraction maps at voltages 0V and 4V of sample "NW4". The red box is a region of interest (ROI). The diffraction maps at different voltage levels do not show any reversible or back-forth variations. Potential issues can arise due to combined NWs response, resulting in merged diffraction responses.

rather showed a combined response of the individual NW peaks, highlighting the presence of multiple NWs, which also results in much more complex analysis due to shared response from each of the individual peaks. The observed multi-peak variations across different voltage cycles were not back-forth or reversible in nature and thus did not conclude voltage-dependent changes.

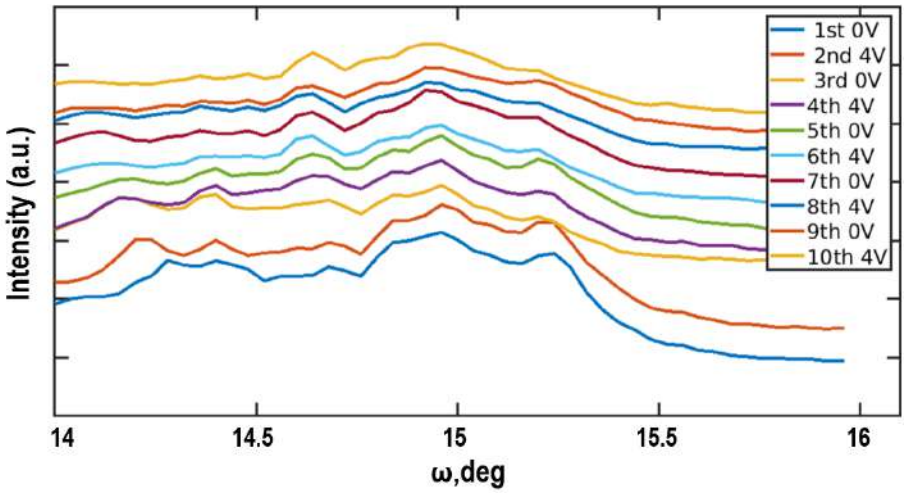

Figure 6.8: Represents the rocking curve for the diffraction patterns across the ROI.

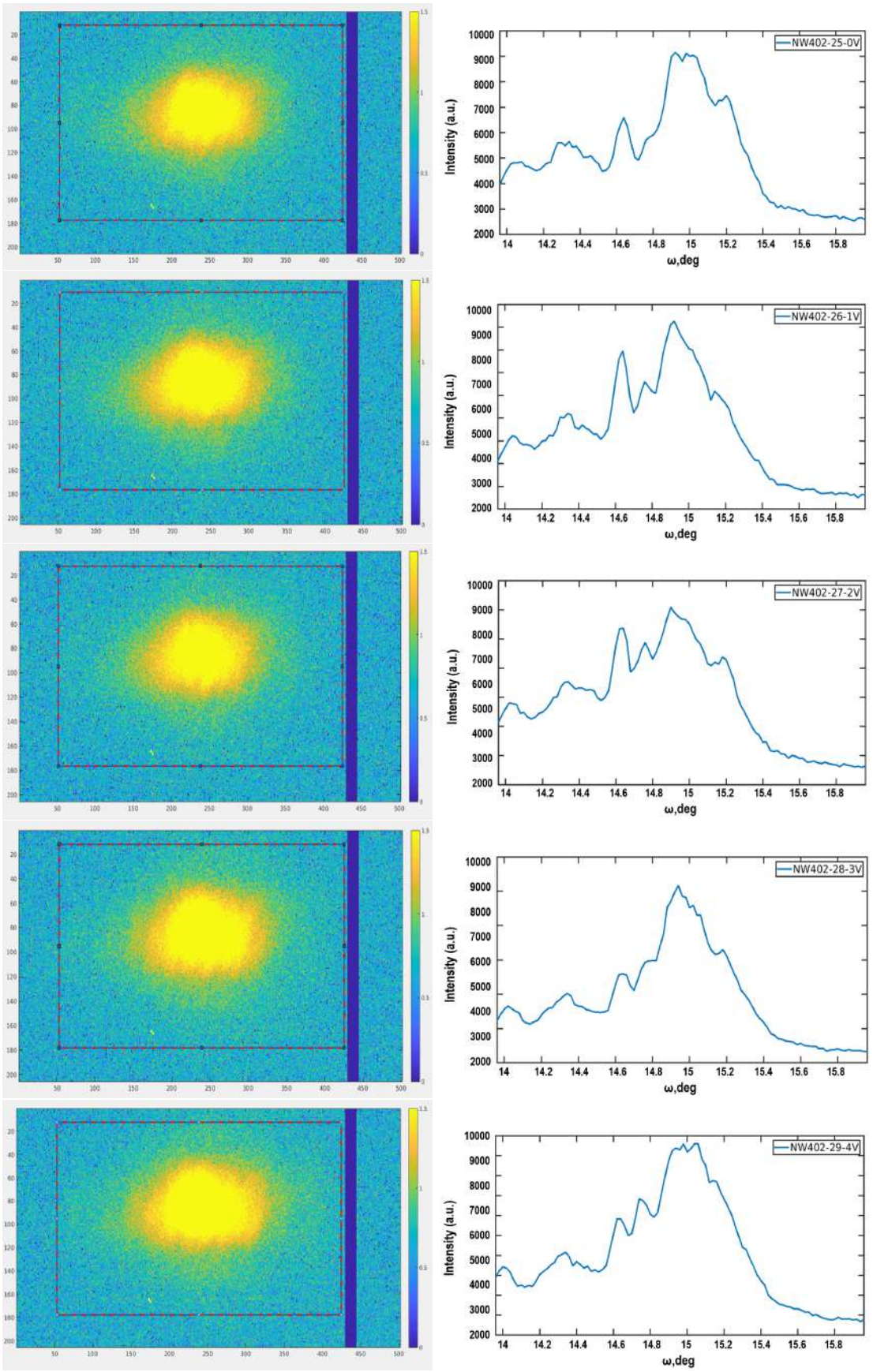

Figure 6.9: Represents the rocking curve for the diffraction patterns of NW4 across the ROI.

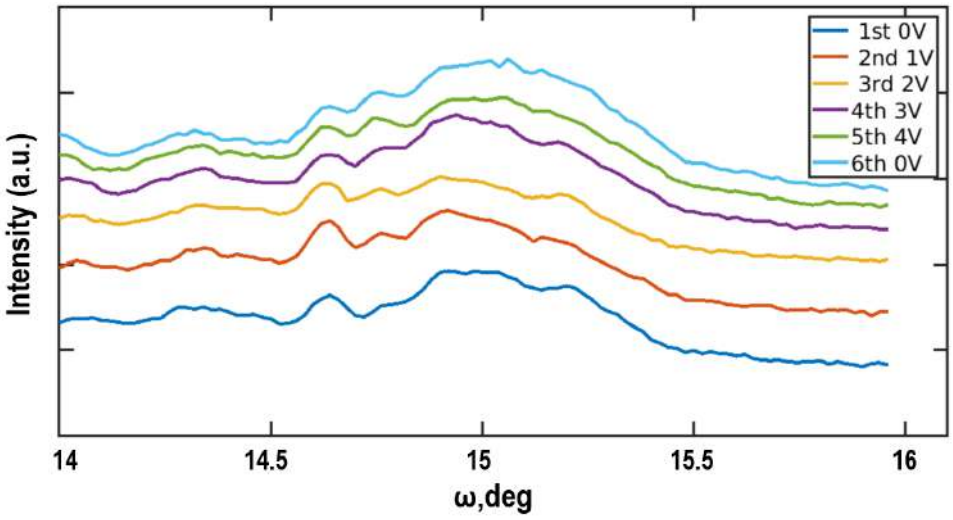

Figure 6.10: Represents the rocking curve for the diffraction patterns of NW4 at 0 V, 1 V, 2 V, 3 V, 4 V cycles across the ROI.

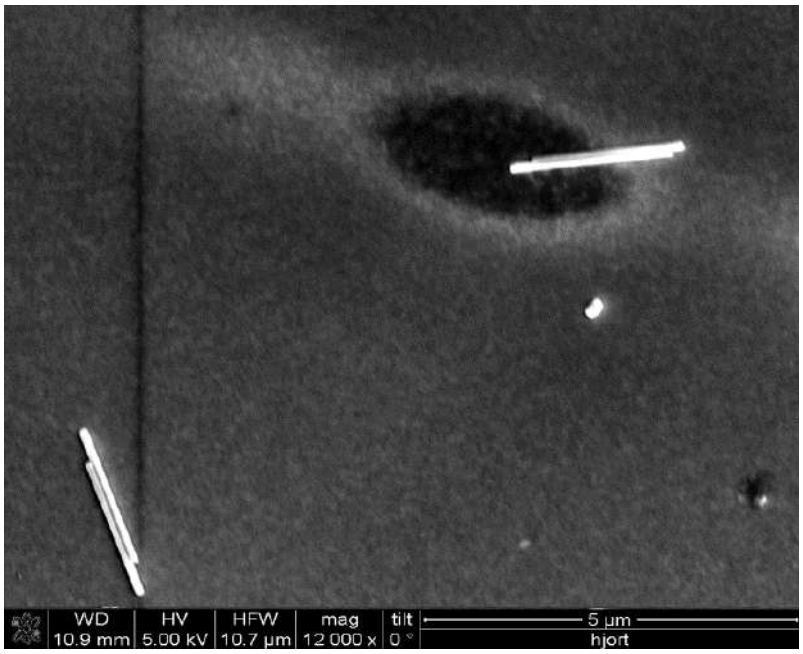

Figure 6.11: Shows the SEM image of the NW4, highlighting bunches of NWs and justifying the multiple peaks observed across the diffraction pattern.

Similar observations are made for the second voltage cycle 0 V, 1 V, 2 V, 3 V, 4 V, and 5 V as well, as shown in Figs. 6.10 and 6.11. Though individual peaks were observed to undergo changes at different voltages, the combined responses from the NWs did not conclude back-forth variations. Moreover, to confirm the presence of

multiple NWs, the SEM image of NW4 samples was recorded, as shown in Fig. 6.12. The next immediate analysis that could enable us to investigate these results would precisely involve individual peak analysis from the obtained results. This would include splitting the rocking curve into multiple peaks and then analyzing the change in each peak with voltage levels. However, without any previous understanding of the response from individual NWs, it will be a challenging and complex task to directly work on the analysis of the combined response from the bunches of NWs.

Therefore, a potential methodology to analyze this multi-NW scenario would involve a precise understanding of the sample's response in the case of a single NW-based structure. Thus, considering the retrieved experimental results, it was essential to quantify the variations in the strain/stress tensor from the voltage cycles, and to achieve this, 3D Comsol modeling and FEM analysis were performed using the COMSOL Multi-physics. The FEM analysis will allow us to understand the dynamic behavioral response of our proposed sample in a more precise manner. With the intent of understanding the effect of NW structure, the impact of voltage cycles on the piezoelectric HZO material, and strain and stress variations with the applied potential and misfit strain, the decision to work on the modeling and simulation of the proposed multi-layer sample via FEM analysis was taken.

6.4 Sample Design and Modeling

In order to perform the analysis over COMSOL Multiphysics, it is important to finalize the material parameters and other involved parameters. It is also essential to consider the stress induced at the interface layers of the adjacent materials. Table 6.1 highlights the parameters for the different materials we used during the sample modeling and analysis in this thesis.

Table 6.1: Modeling parameters used for FEA Analysis

Material Property	TiN	Si	InAs	HZO
Lattice parameter(nm)	0.495	0.543	0.427	0.515
Young's Modulus(Pa)	2.9×10^{11}	1.7×10^{11}	5.14×10^{10}	1.31×10^{11}
Poisson's ratio	0.325	0.28	0.35	0.31
Thickness(nm)	10	60	80	20

In the context of structural mechanics or finite element analysis (FEA), the elasticity matrix—also known as the stiffness matrix—is a mathematical representation that shows how a material or structure deforms under applied forces. It captures a structure's geometrical features and material qualities, enabling engineers to forecast how the structure will react to outside stresses. In addition to these parameters, we would additionally utilize the elasticity matrix C_{ijkl}

$$C_{ijkl}[GPa] = \begin{bmatrix} 546 & 101 & 101 & 0 & 0 & 0 \\ 101 & 546 & 101 & 0 & 0 & 0 \\ 101 & 10 & 546 & 0 & 0 & 0 \\ 0 & 0 & 0 & 77 & 0 & 0 \\ 0 & 0 & 0 & 0 & 77 & 0 \\ 0 & 0 & 0 & 0 & 0 & 77 \end{bmatrix} \tag{6.1}$$

and the coupling matrix explains the interplay between several physical events in a system. It frequently refers to the interplay of various forces and deformations, including mechanical, thermal, and electrical fields, in structural engineering. Therefcoupling matrix H_{ijk} for the HZO layer

$$H_{ijk}[C/m^2] = \begin{bmatrix} 0 & 0 & 0 & 0 & 17 & 0 \\ 0 & 0 & 0 & 17 & 0 & 0 \\ -6.6 & -6.6 & 23 & 0 & 0 & 0 \end{bmatrix} \tag{6.2}$$

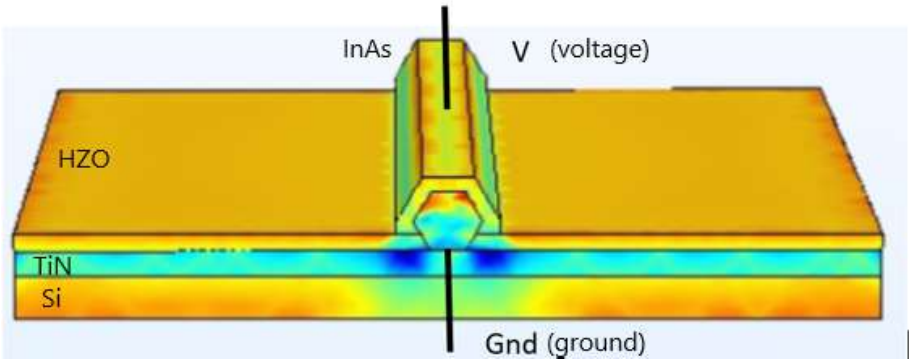

Figure 6.12: 3D model structure showing the applied voltage (V) and ground signal.

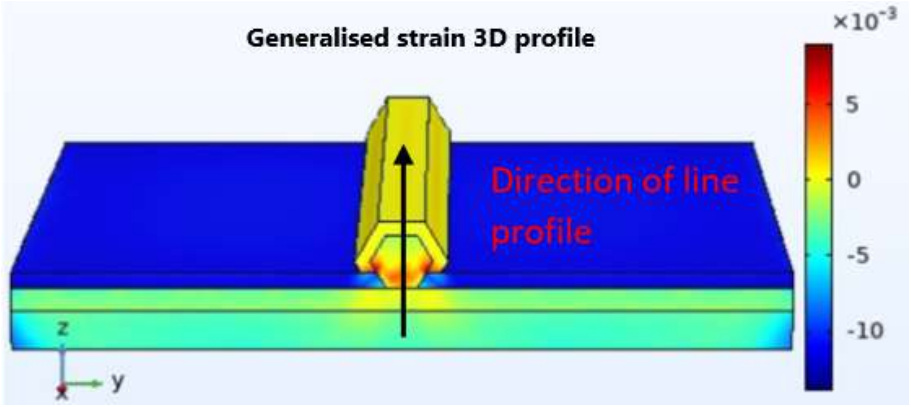

Figure 6.13: 3D model structure showing the direction of the profiling while retrieving 1D results.

As per the structural design discussed above, the sample modeled has silicon (Si) of 60 nm thickness in the z-axis. Then, over the Si, we have titanium nitride (TiN) of 30 nm in the z-axis and at the center, we have placed InAs nanowire (NW) in a hexagonal shape with 70 nm thickness in the z-axis, at the top of the TiN. Finally, the HZO layer covers from the top the InAs NW and TiN layer, which can be seen in Fig. 6.13. The x-axis and y-axis of all the layers are 1000 nm in dimension. Fig. 6.14 shows the overall model of the sample under investigation, modeled with the COMSOL, as per the dimensions mentioned and material properties, as mentioned in Table 6.1. In the figure, 'V' resembles the applied voltage while 'Gnd' resembles the ground, provided to the substrate end. In addition to this, Fig. 6.14 shows the direction across which the profiling is performed in subsequent results. In simpler terms, the variations in the properties are retrieved in the direction from the substrate to the applied HZO layer, as shown in Fig. 6.14.

While performing the analysis, two analysis pipelines were performed. The first analysis was performed with the applied voltage only, where only external voltage-dependent results were investigated. In the second analysis pipeline, both misfit strain and voltage cycles were applied. The misfit strain at each of the interfaces was calculated and applied. The line profiles were retrieved in the direction from the substrate to the HZO layer, along the z-axis. The line profile of the applied electric potential, displacement field, strain tensor, and stress tensor are retrieved and different components of the displacement field and stress/strain tensors are analyzed.

For each of these two analysis pipelines, two further sub-analysis were performed. One for the conventional 4-layer structural analysis, and the second using the actual NW structure. This sub-level analysis enables us to understand the change in stress and strain profiles while replacing the conventional layered configuration with that of the NW structure. Table 6.2 briefly highlights the overall analysis performed using COMSOL Multiphysics.

Table 6.2: FEA Analysis performed using COMSOL Multiphysics

Analysis type	Analysis 1	Analysis 2	Analysis 3	Analysis 4
Structure type	4 layer model	4 layer model	NW sample	NW sample
Voltage applied	True	True	True	True
Misfit strain	False	True	False	True

6.5 Analysis 1: 4 layer sample structure with only applied voltage

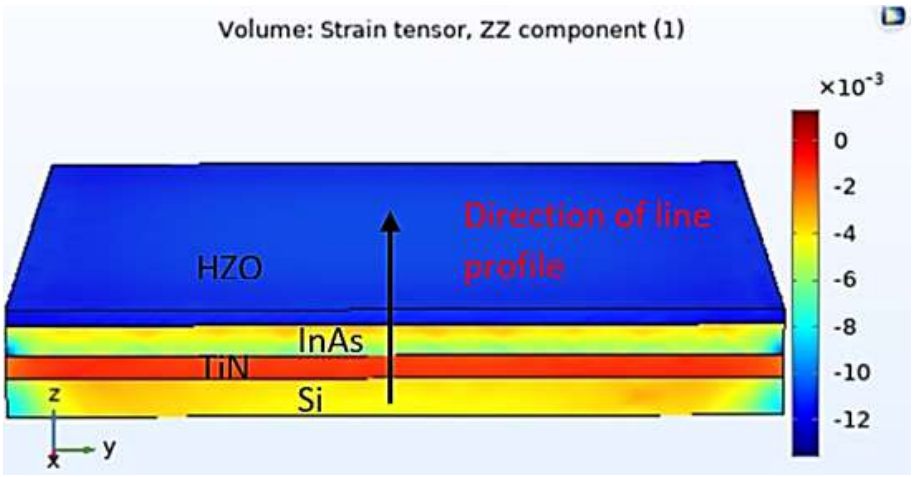

Figure 6.14: 3D modeled structure for Analysis I.

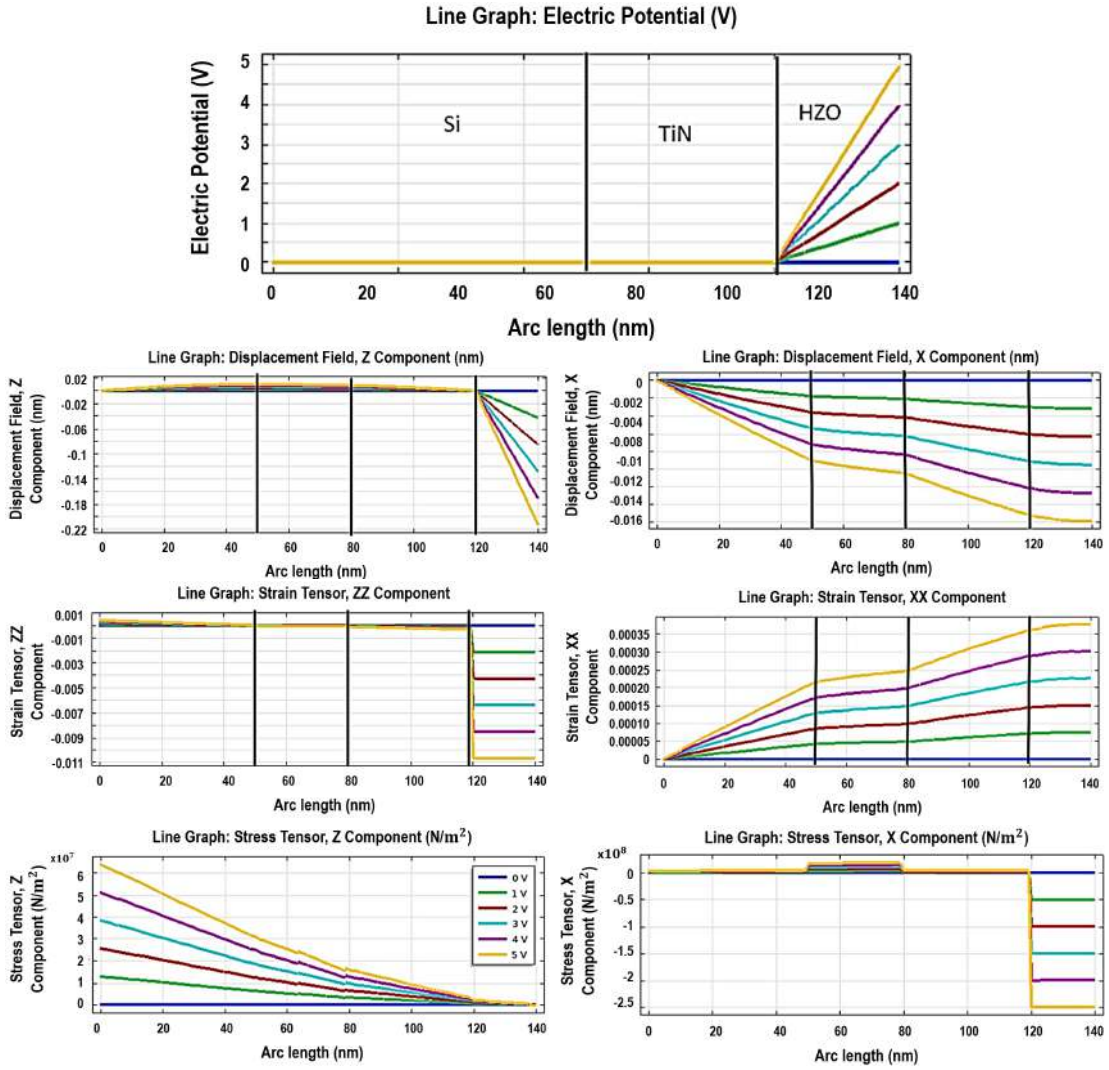

Figure 6.15: Analytical results showing the line profiling for Analysis I.

The first analysis was performed with only applied voltage across the rectangular, layered structure. The model is shown in Fig. 6.15, where the profiling is done along the direction from the substrate to the HZO layer, and the NW stricture is replaced by a simpler layered design. The thickness of each of the layers is as follows: HZO layer [20 nm], InAs [40 nm], TiN [30 nm] and Si [50 nm]. The intensity values in Fig. 6.15 show the ZZ component of the strain variations.

Fig 6.16 shows the results from the 3D model of the 4-layer structure. We performed several analyses across different configurations and voltage cycles. The following results were retrieved during the FEM analysis of the sample structure.

- Potential profile: Analyzing the variations in the potential across the individual

materials. We aim to observe voltage variations across the HZO piezoelectric layer only, as the output stress/strain response depends on the voltage-induced variations across the piezoelectric material. This is achieved, as visible in the line profile of the electric potential variations from Fig. 6.16.

- Displacement field: The displacement profile was extracted across two directions, the z component and the x component, so as to observe the variations across both perpendicular to the plane and parallel to the plane directions.
- Stress and strain components: From the 3D variations in strain and stress, we analyzed the z component and the x component. All the line profiles are extracted, passing through the approximate center of the sample along the z direction.

For analysis 1, we observed significant voltage-induced variations. The voltage cycles were applied as the DC voltage input at levels 0 V, 1 V, 2 V, 3 V, 4 V, and 5 V. The higher magnitude of stress, strain, and displacement supports the idea of higher piezoelectric response at higher applied voltages. Ensuring potential drop across the HZO layer only helps us ensure maximum observable variations, as potential change across non-piezoelectric material would not yield any stress/strain variations. Interestingly, it is also important to ensure the sample has a rigid structure, while also allowing the individual layers to undergo physical deformations at the nano-level. To achieve this, we applied boundary conditions at two of the opposite edges of the samples, ensuring necessary rigidity to the structure, and treating it as a rigid structure.

6.6 Analysis 2: 4 layer sample structure with applied voltage and misfit strain

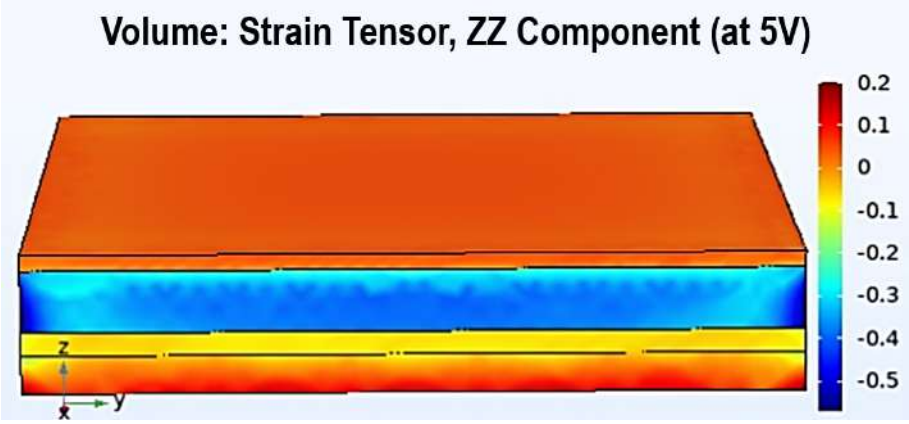

Figure 6.16: 3D modeled structure for Analysis II.

As the analysis I ends, we would now switch towards the analysis under the application of both voltage and the misfit strain. This would bring a more realistic analysis, as both the voltage and misfit strain would impact the behavioral response of the sample in real-life situations. The magnitude of the misfit strain depends on the lattice parameters of the interface layers, which are explicitly added during the modeling. With initial observations from Fig. 6.17, we can certainly comment on the much higher magnitude of the strain and stress tensors over the sample in the case of added misfit strain.

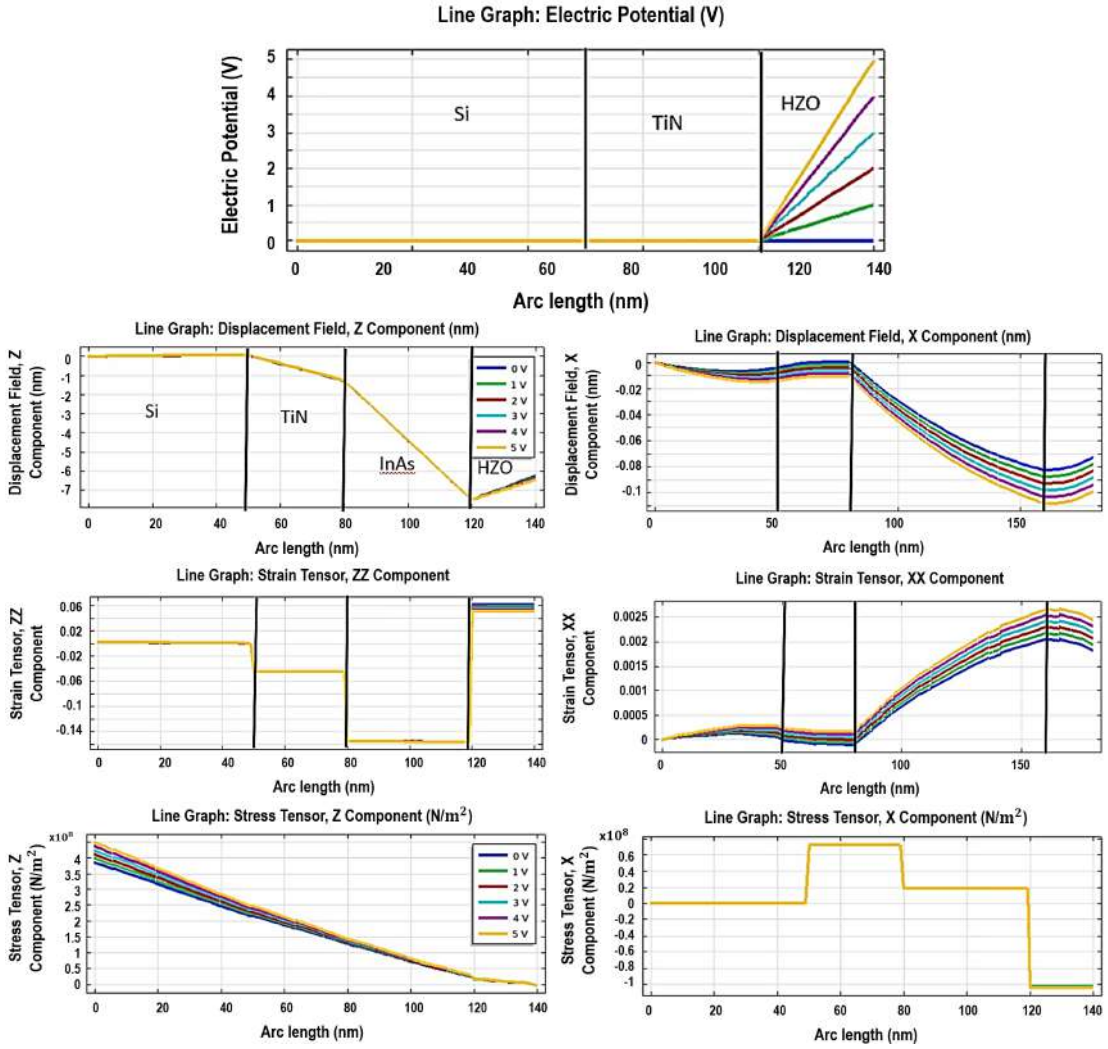

Figure 6.17: The analytical results showing the line profiling for Analysis II.

This increase in magnitude is evidently visible across the line profiles of the FEM results as well. To ensure precise comparison, we maintained the same potential drop for both the Analysis I and Analysis II scenarios, as shown in the potential profile in Fig. 6.18. However, the z component of the displacement field variations at different voltage cycles almost overlaps with each other. However, the proportional behavior of response, that is, an increase in applied voltage proportionally increases the magnitude of the displacement, is still maintained, which matches our expectations. The possible overlapping of the profiles for different properties (displacement field, strain tensor, and stress tensor) along the z component can be explained by the high impact of the misfit strain. The added misfit strain component well dominates the voltage-induced variations. Though proportional voltage-induced variations are still maintained, their relative impact on the overall line profile is highly minimized due

to the much stronger effect of the added misfit strain. This behavior is observed for all analyzed properties across the z component.

Though the high value of properties can be explained with the addition of misfit strain, it is highly important to quantitatively understand the results as well so that the observed values lie in the expected range. However, this adjustment of the stress values by introducing a correction parameter will be better discussed after the completion of all 4 analyses.

6.7 Analysis 3: NW sample structure with applied voltage only

After performing the analysis across the layered structure, the modeling and analysis of the NW-based structure are performed. This model, as shown in Fig. 6.19, correlates well to the actual structure of the sample under investigation. Analysis III allows us to understand the change in the stress and strain tensor as we shift from the layered structure to the NW-based samples. For analysis III, we applied the voltage cycles such that potential variations are observed across the InAs (NW) and HZO layers. This would allow us to observe the variations in the diffraction peaks from the NW structures. Similar to analysis I, we clearly observed voltage-dependent variations in the presence of the applied voltage only. Moreover, the overall behavior of the profile for strain and stress tensors undergoes significant change as we switch from the plane layer to the NW structure. This is evident by comparing the profiles from Analysis I and Analysis III and can be justified by the impact of the hexagonal NW shape, replacing the standard rectangular layer.

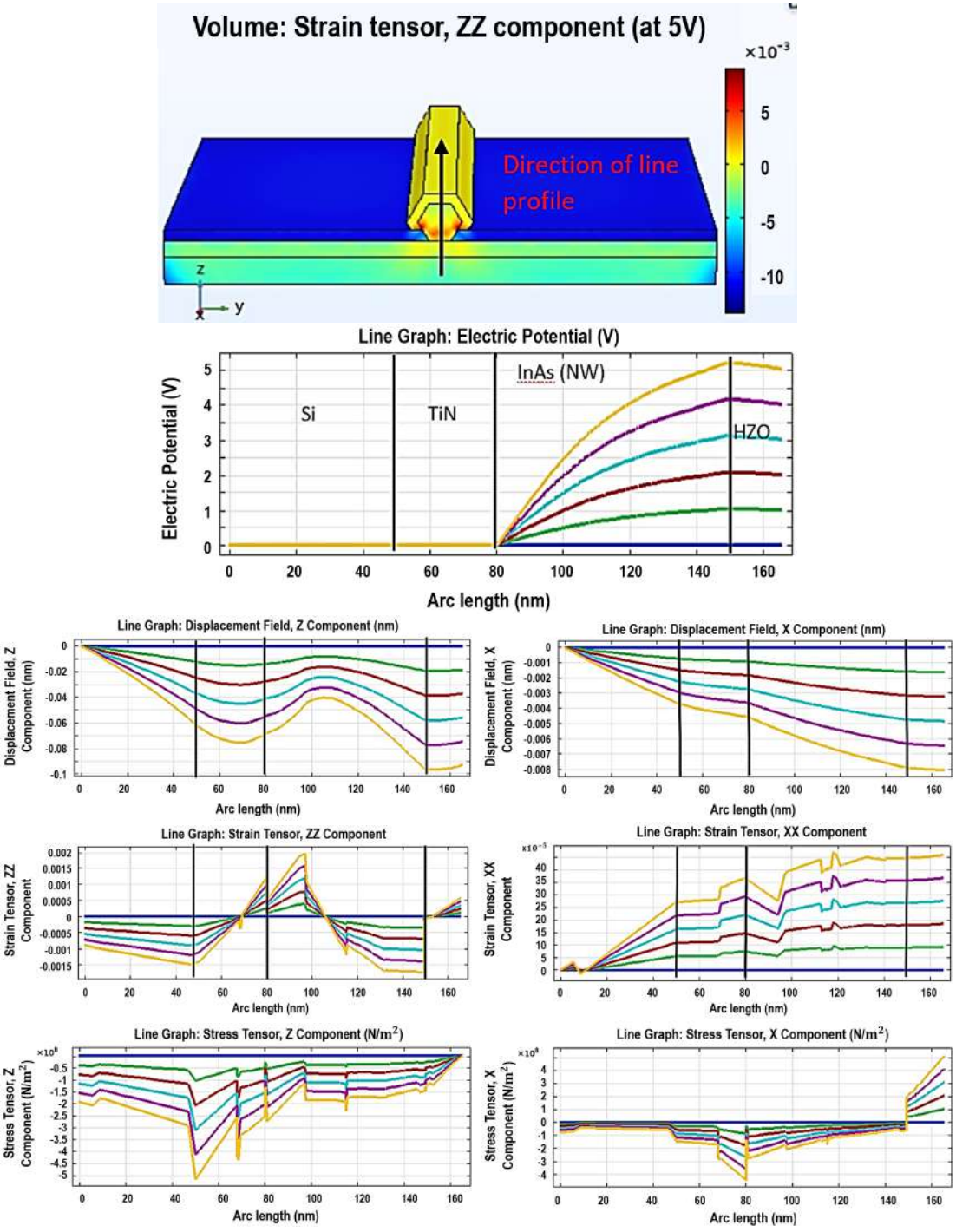

Figure 6.18: 3D modeled structure and FEM results for Analysis III.

6.7.1 Analysis 4: NW sample structure with applied voltage and Misfit Strain

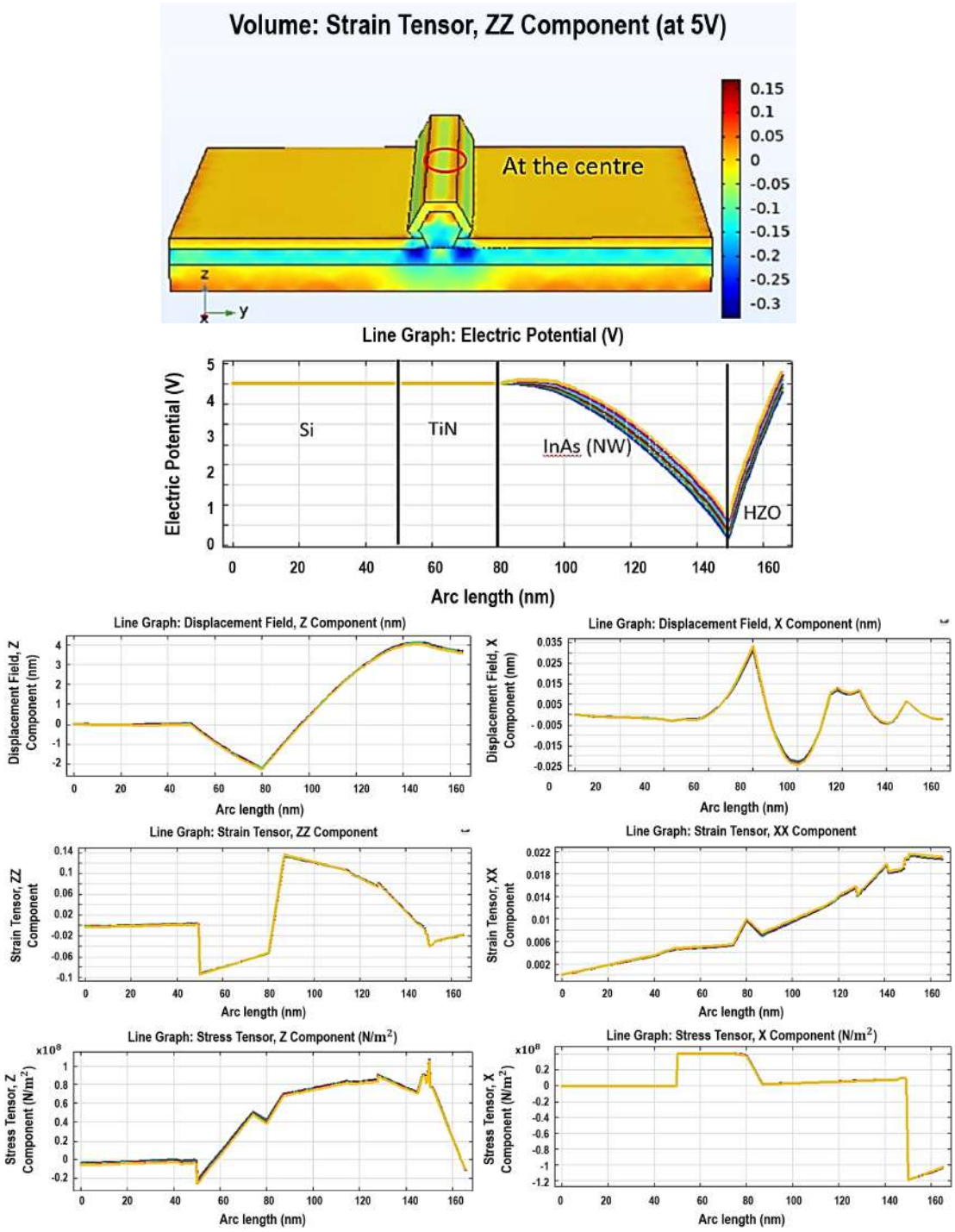

Figure 6.19: 3D modeled structure and FEM results for Analysis IV [ROI 1].

Analysis IV, as shown in Fig. 6.20, brings out the most realistic investigation for our study, as this corresponds to the actual dimensions and configuration and the right use of voltage cycles with misfit parameters. We again observed a significant increase in the overall magnitude of the displacement field, and stress/strain tensor, similar to what we observe as we move from Analysis I to Analysis II. Continuing this, we also observed the overlapping behavior of the variations at different voltage cycles as we did for analysis II with both voltage and misfit strain. The justification in this analysis IV would also be related to the high dominance from the misfit strain-induced variations, minimizing the relative variations due to different voltage cycles.

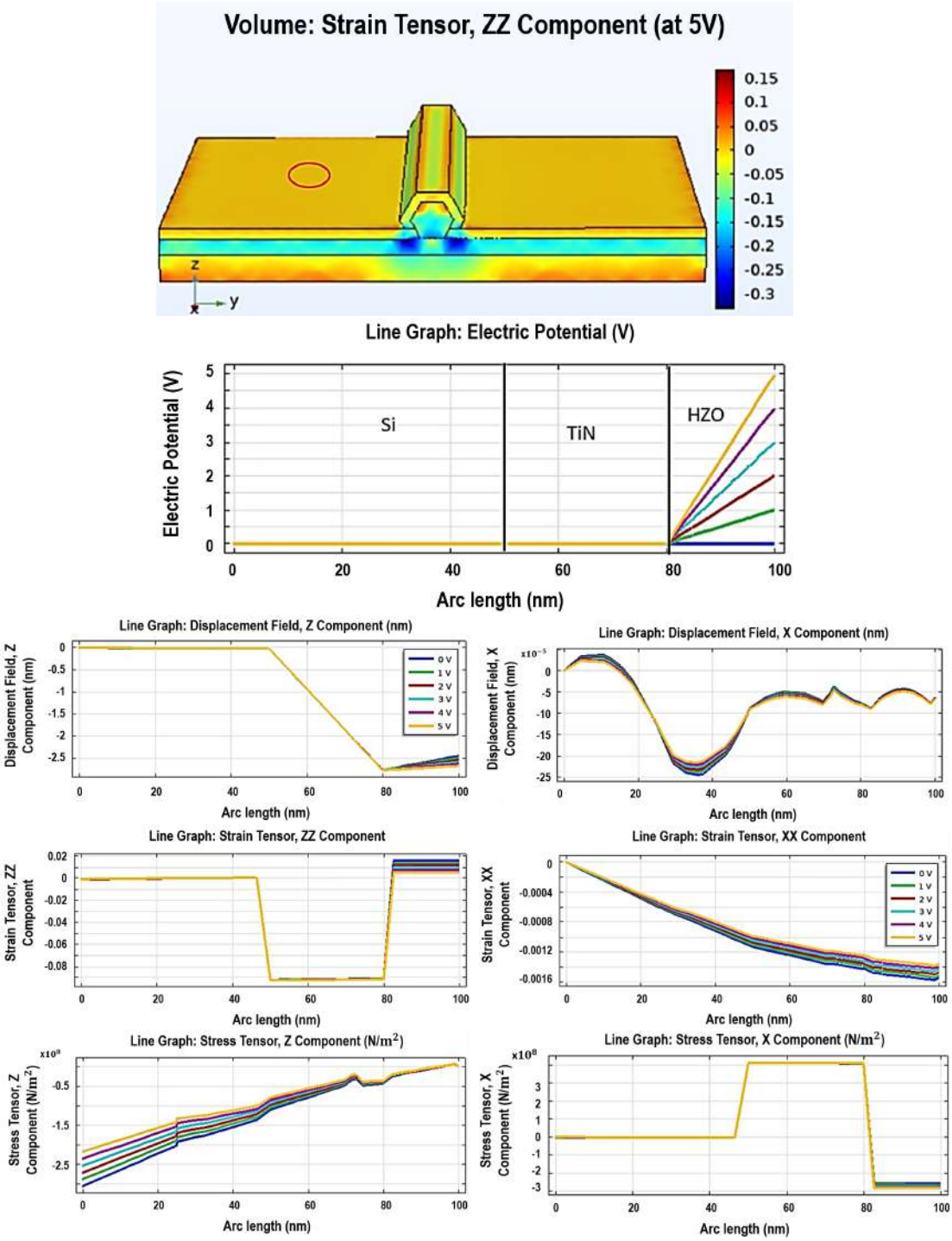

Figure 6.20: 3D modeled structure and FEM results for Analysis V [ROI 2]

Interestingly, analysis IV has two sub-analyses as well. The red ROI over the 3D model of the sample in Fig. 6.20 highlights the position across which the line profiling is retrieved. We should keep a note that positive stress values are observed in this ROI profile. This is essential as the net stress across the whole sample should cancel

each other, in the absence of any external application of stress. To ascertain this point, Fig 6.21 includes the same sample analysis, but rather at a different ROI position. Negative stress values at a different ROI complement our expectation that the overall stress tensor across the entire sample tends to cancel out each other. Now returning to the quantitative examination of the stress values, the maximum stress magnitude should be restricted within the order of 10^8 during the simulations in order to support the real model expectations. This magnitude should not be higher than we expect and we would thus we shall utilize a correction parameter to tune in the results so that the stress values can be in the expected range.

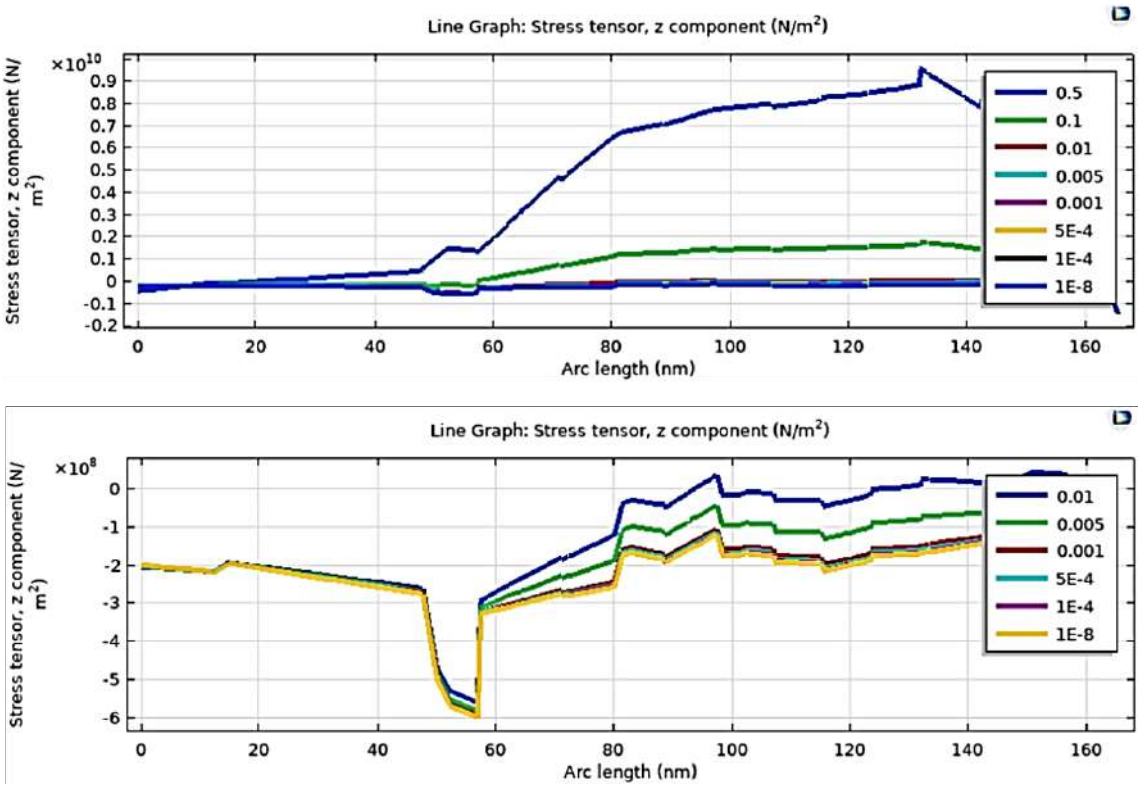

Figure 6.21: Correction parameter determination for tuning stress values.

The determination of the ideal correction parameter involved iterative analysis. While performing the iterative analysis, we selected a series of possible values for the correction parameter, which would impact the applied misfit strain and tune the stress tensor magnitudes while keeping the overall behavior intact. For a possible value of the correction parameter, we select the configuration where the stress tensor values are closer to the realistic values. As shown in Fig. 6.22, increasing the correction parameter above 0.01, the stress values will shift to higher positive values

(which is not desirable), and if we decrease it below 0.01, the stress values tend to observe a limiting scenario where we don't get any further drop even after reducing the value of the parameter before 0.0001. Therefore, the adequate value of the correction parameter is expected to be 0.01, providing a realistic drop in values at which stress magnitudes is around $10^8 N/m^2$.

6.8 Conclusion

The piezoelectric properties of a novel $Hf_xZr_{x-1}O_2$ based structure have been discussed in this section. While the experimentation over the sample structure was performed at MAXIV and PETRA III, the initial results showed concerns due to the multi-peak NW response. This not only caused the smearing of individual peaks but also dominated the reversible changes, one would expect while applying voltage cycles. The simulations and 3D modeling was then performed in order to determine the qualitative and quantitative behavior of the sample under investigation. This involved the use of necessary boundary conditions, physical parameters, and properties for each of the materials used within the sample structure. Several step-wise analyses were performed with different configurations and voltage cycles. We simulated different structures in layered and NW configurations, with and without the impact of the interface, to understand the impact on the pressure response from the piezoelectric layer. These simulation results will now be a reference for us while we perform peak splitting from the experimental datasets. As the final step, the variations in strain response due to the voltage cycles in simulations will allow us to quantitatively compare with the experiment analysis. Further optimization of the stress values was performed by the addition of a correction parameter, which enabled us to keep the stress field within the expected range of values.

7 Angular X-ray cross-correlation analysis (AXCCA)

7.1 Basics of AXCCA

Z. Kam first presented this method for reconstructing a single-particle scattering pattern from several patterns obtained from a system of disordered identical particles in his groundbreaking publications [132]. Because there wasn't enough equipment at the time, it wasn't developed further. Advances in instrumentation and computational capacity have, however, led to something of a revival for AXCCA since the more recent work by Wochner et al. [19]. In theoretical research [133], [134], the basic concept of a single-particle scattering pattern recovery was thoroughly established. As was shown for 2D [135] and 3D [136] particles, this single-particle scattering pattern may also be utilized for iterative phase retrieval techniques to rebuild the electron density within the particle. Figure 2.16 illustrates one such application of AXCCA.

Angular X-ray cross-correlation analysis (AXCCA) is a methodology that enables the structural analysis of the sample and quantitative assessment of the angular anisotropy of the diffraction patterns that were obtained experimentally. It allows the users to understand the orientation order of the structure and brings out better correlation signals between the individual intensities at their respective transfer vectors with the analysis of the averaged diffraction patterns. To start with the concept of AXCCA, one may consider a two-point Cross-Correlation Function (CCF) in order to investigate the correlations between intensities collected at different locations on a 2D detector. Mathematically, it is defined as:

$$C(q_1, q_2, \Delta) =< (I'(q_1, \varphi)I'(q_2, \varphi + \Delta)) >_{\varphi}, \tag{7.1}$$

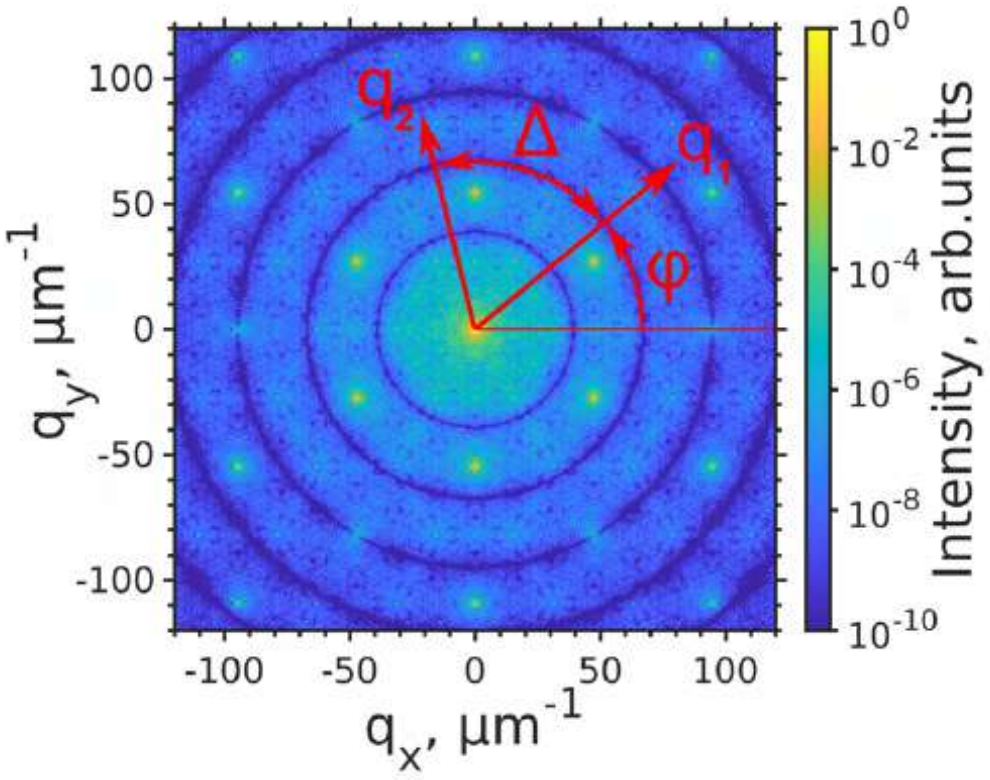

Figure 7.1: A cross-correlation function's definition. The CCF at this angle Δ is derived from intensities measured at two distinct locations, q_1 and q_2, separated by the angle Δ. Adapted from [137]

where φ is an angle along the arc for azimuthal coordinate, Δ is a relative angle between two locations, and $< .... >_{\varphi}$ indicates an average across the angle φ, ref Fig. 7.1. The normalized intensity, measured on the arc of radius q with respect to the direct beam position, is represented by $I'(q_1, \varphi)$. The variables in Fig. 7.1 are the ones utilized in this definition. [137]

There are several approaches to normalizing the measured intensity $I(q, \varphi)$ to its mean value $< I(q, \varphi) >_{\varphi}$.

$$I'(q, \varphi) = I(q, \varphi) - < I(q, \varphi) >_{\varphi} \tag{7.2}$$

$$I'(q, \varphi) = I(q, \varphi) / < I(q, \varphi) >_{\varphi}, \tag{7.3}$$

$$I'(q, \varphi) = [I(q, \varphi) - < I(q, \varphi) >_{\varphi}] / < I(q, \varphi) >_{\varphi} . \tag{7.4}$$

Eqs. 7.2, 7.3, and 7.4 qualitatively express the same CCF result; however, quantitatively, each of the three methods results in a different CCF value. While Eq. 7.2 gives a shifted value with a subtracted mean, Eq. 7.3 gives a scaled quantity with a divided mean. However, since the ideal qualitative nature of the CCF doesn't depend on normalization, the distinctive characteristics found in the ideal scenario of CCF are independent of normalization. On the contrary, in practical scenarios, variations in the CCFs obtained for various normalized measured intensities are observed and are affected by noise and other experimental factors, including detector gaps and poor detector calibration. This makes proper handling of such parameters an important aspect while performing statistical analysis using CCF.

The resultant CCF is mathematically expressed as a function of three primary parameters: angular variable, Δ, q_1, and q_2. When the intensities dispersed at a given relative angle Δ are correlated, the CCF function yields higher values, whereas when they are uncorrelated or anticorrelated, the function gives us lower values. This efficient property of CCF analysis brings numerous characteristic structural details about the sample being examined.

Considering the anisotropic behavior of the diffraction pattern, with the periodic behavior of the scattered intensities along the azimuthal angle φ, one can consider the Fourier-based understanding of the same period. Mathematically,

$$I(q,\varphi) = \sum_{n=-\infty}^{\infty} I_n(q) e^{in\varphi}, \tag{7.5}$$

where the nth component is expressed as:

$$I_n(q) = \frac{1}{2\pi} \int_{-\pi}^{\pi} I(q,\varphi) e^{-in\varphi} d\varphi, \tag{7.6}$$

With the Fourier series expansion of the CCF function:

$$C(q_1,q_2,\Delta) = \sum_{n=-\infty}^{\infty} C_n(q_1,q_2) e^{in\Delta}, \tag{7.7}$$

Where the nth component is given by:

$$C_n(q_1,q_2) = \frac{1}{2\pi} \int_{-\pi}^{\pi} C(q_1,q_2,\Delta) e^{-in\varphi} d\Delta, \tag{7.8}$$

CCF is a real-valued function in principle and thus gives us the same value for the conjugate complex, expressed as:

$$C_{-n}(q_1,q_2) = C_n^*(q_1,q_2), \tag{7.9}$$

Moreover, CCF is an even function by nature. The individual Fourier components $C_n(q_1,q_2)$ carry essential information about the symmetry of the system under analysis. Mathematically, n-fold symmetry in the retrieved diffraction pattern yields n-fold components in the CCF Fourier spectrum and this allows us to retrieve symmetries in the less ordered sample systems. These CCF components are related to the components of the scattered intensity $I_n(q)$. While following the convolution theorem, we get:

$$C_n(q_1,q_2) = I_n^*(q_1) \cdot I_n(q_2), \tag{7.10}$$

where the complex conjugation is indicated by $*$. These relationships may be used to extract the single-particle scattered intensities from an ensemble-averaged CCF

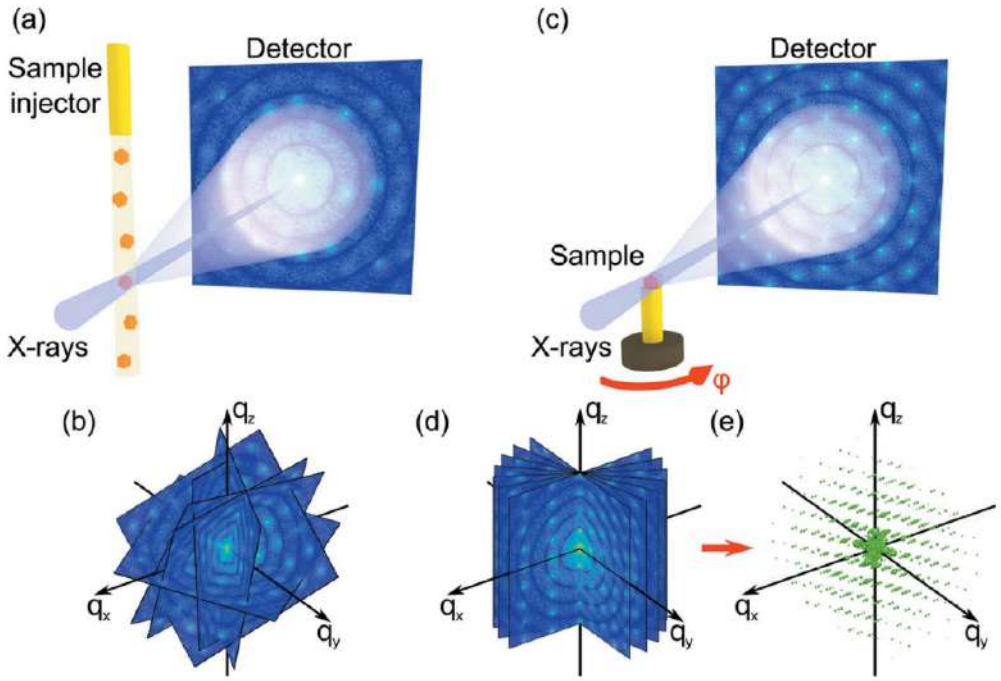

Figure 7.2: Generalized experimental setup showing the injected samples under investigation. (b) Shows the individual 2D slices of the 3D reciprocal space structure. The sample is rotated around the axis normal to the incident beam in order to retrieve individual 2D patterns. The individual 2D patterns are thus analyzed and interpolated across the 3D space. Adapted from [138].

as well as calculate the CCF from experimentally obtained intensities.

As mentioned before, the AXCCA involves the analysis of the two-point correlation function, depending on the individual intensities measured at q_1 and q_2 with relative angle Δ. The mathematical value of CCF due to correlation from these intensities is given by:

$$C(q_1, q_2, \delta) = \langle I'(q_1) I'(q_2) \cdot \delta(\frac{q_1 \cdot q_2}{|q_1||q_2|} - \cos\Delta) \tag{7.11}$$

The intensities in Eq 7.11 are the normalized intensities scaled to their mean values, as mentioned before. The averaging is performed along the intensities observed at the transfer vectors q_i with the length $\mid q_i \mid$. The overall process of the AXCCA analysis experimentally can be graphically represented from the setup, as shown in Fig. 7.2

The CCF values between all possible combinations of intensities are retrieved over many 2D diffraction patterns. Analysis over multiple patterns allows better statistics and suppresses the random correlations that we wish to avoid in our results. This also allows analysis across individual cuts of the 3D reciprocal space and enables the investigation of all possible correlations within the sample. While considering crystalline samples, AXCCA has been used to understand their scattering patterns corresponding to diffraction peaks. [36]. In such case, the CCF at the characteristic angular difference Δ yields higher values when the transfer functions q_1) and q_2 correspond to the respective Bragg positions, such that $q_1 =\mid g_1 \mid$ and $q_2 =\mid g_2 \mid$, ie: reciprocal lattice vectors. This gives us the precise fit of the proposed structural model and the experimental CCF peaks observed at the angle Δ, with lattice basis vectors a_1 and a_2. Thus, it allows us to analyze the sample structure along with the understanding of any deviations from the ideal model.

In the case of a system, made up of a few randomly oriented identical particles, characteristics in a scattering pattern can be linked to distinct particles and their interference with one another. Two kinds of correlations are present in the CCF computed for such a pattern: one, between the features of a single particle and the other between the features from different sets of particles. The first kind of correlation is constant, arising from the same particle correlation, while the second type of correlation depends on the relative orientation of the combination of different particles within the sample. Increasing the statistics of the retrieved CCFs across multiple orientations allows us to maintain systematic correlations, while random inter-particle correlations are eliminated. Mathematically, it has been proven that the ensemble-averaged CCF across multiple orientations tends to converge to the single particle CCF itself [133]. Mathematically,

$$< C(q_1, q_2, \Delta) >_M = C_1(q_1, q_2, \Delta) as M \rightarrow \infty \tag{7.12}$$

where $< .... >_M$ denotes ensemble averaging over M diffraction patterns are collected from a system of the same particles but in different random angular orientations, and $C_1(q_1, q_2, \Delta)$ is a CCF calculated for a scattering pattern from a single particle calculated at transfer vectors q_1 and q_2. $C(q_1, q_2, \Delta)$ is a CCF calculated for a scattering pattern from a system containing a few randomly oriented identical particles. Such ensemble averaging can be performed momentarily (when particles in dispersion are randomized owing to thermal motion) or spatially (by gathering

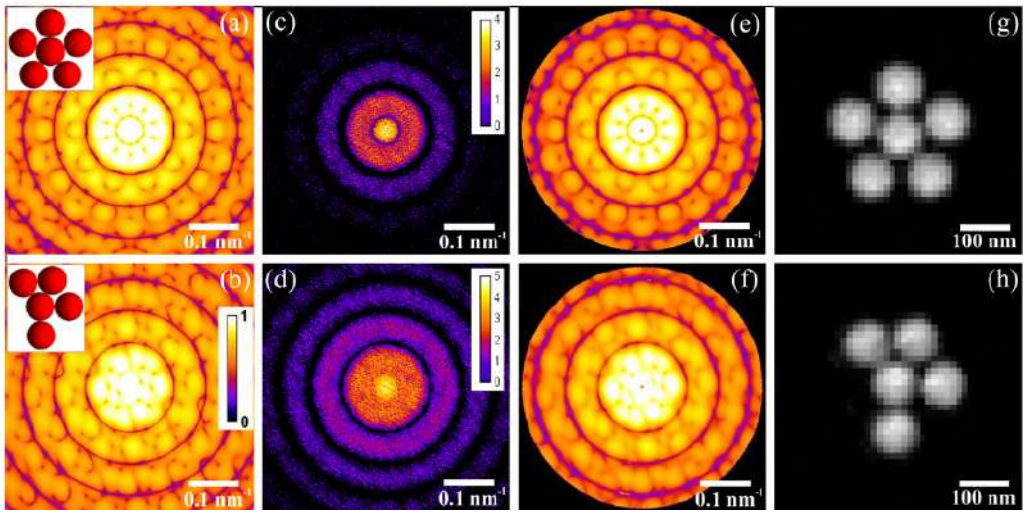

Figure 7.3: Recovery using AXCCA of a single-particle scattering pattern. (a, b) Simulated scattering patterns (logarithmic scale) for an asymmetric cluster (b) and a single pentagonal cluster (a); the clusters are displayed in the insets. (c, d) Scattering patterns from a disordered system with N = 10 clusters arranged randomly in terms of orientation and location. (e, f) Scattering patterns derived from M = 105 diffraction patterns, representing a single pentagonal (e) and asymmetric (f) cluster, respectively. (g, h) Reconstructed structure of a single cluster utilizing the diffraction patterns seen in (e) and (f) and an iterative phase retrieval approach. Adapted from [133].

scattering patterns from various parts of the sample). This kind of averaging is frequently employed in applications and enhances the distinctive signal.

7.2 Analysis of structural parameters of Au mesocrystals using angular X-ray cross-correlation analysis

7.2.1 Sample and Experimentation

Development of Angular X-ray Cross-Correlation analysis and its application to investigate the structural parameters of Au mesocrystals were analyzed with this technique and were formed by the octahedral nanocrystals as a part of our experimental analysis, as explained in this section. The gold mesocrystals were assembled from octahedral nanoparticle building blocks (33 – 67 nm) that were synthesized according to the literature [139]. The analysis is performed over five different samples of sizes 72 nm, 58 nm, 46 nm, and 37 nm. At 58 nm edge length, we have two polymer weights of 43 g/mol and 66 g/mol. These nanoparticles were functionalized into ω-thiol-terminated polystyrene (weight: 22 k g/mol, 43 k g/mol, 66 k g/mol) and transferred from water to toluene [140]. The self-assembly of the particles was introduced using a gas-phase diffusion technique with ethanol as an antisolvent. The antisolvent diffuses over the gas phase into the nanoparticle dispersion and gradually destabilizes the particles leading to self-assembly. The samples analyzed in this section are marked in Fig. 7.4 for visualization.

The X-ray diffraction (XRD) experiment was performed on gold (Au) mesocrystalline grains with different octahedral sizes (33 – 67 nm) and polymer chain lengths (see inset in Fig. 2). The experiment took place at in situ X-ray diffraction and imaging beamline P23 of the PETRA III storage ring (DESY, Germany) (see Fig. 2 for the schematic layout of the experimental setup). Monochromatic X-rays of 8.320 KeV were focused down to 1 µm × 3 µm (V×H) by compound refractive lenses (CRLs) made from beryllium (Be), totally covering smaller colloidal crystal grains. The mesocrystal grains were put on a tungsten tip and were rotated around the vertical axis in increments of 0.5° across a range of 0° to 180°. The 2D far-field diffraction patterns were collected by the X-Spectrum Lambda 750K detector, which was 1.497

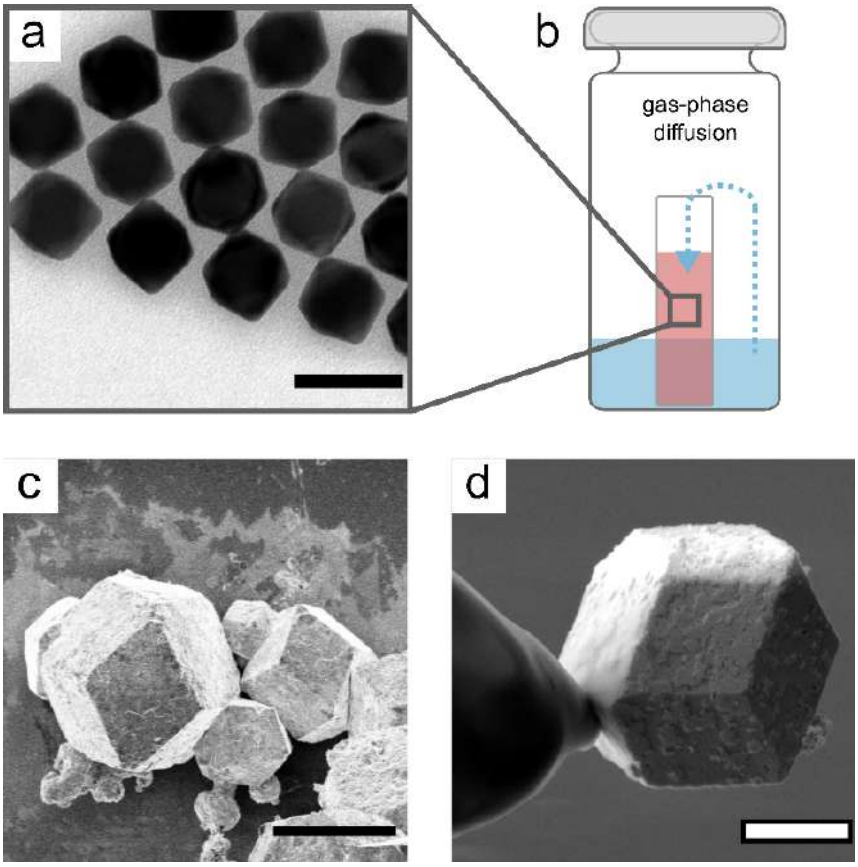

Figure 7.4: Overview of the synthesis of the mesocrystal samples. a) Exemplary TEM image of Au nano octahedra functionalized with ω-thiol-terminated polystyrene. The scale bar is 50 nm. b) The nanoparticles are assembled using a gas phase diffusion approach. The sketched setup depicts a closed vial containing the antisolvent and a smaller one containing the nanoparticle dispersion. The antisolvent diffuses over the gas phase into the nanoparticle dispersion and gradually destabilizes the particles, leading to self-assembly. c) The resulting mesocrystals are investigated using SEM and feature a defined faceting of the superstructure. The exemplary SEM image depicts mesocrystals being removed from the solution. The scale bar is 10 µm. d) Individual mesocrystals can be separated and attached to a polymer tip for diffraction measurements. The scale bar is 2 µm.

m downstream from the sample, at each angular position. A series of two frames of 1 s exposure each were measured at each angular position, resulting in a total of 2 s exposure. The sample was cooled by a liquid nitrogen stream to minimize radiation damage to the organic ligands (stabilizing nanocrystals), which might lead to nanoparticle coalescence and the loss of superlattice organization.

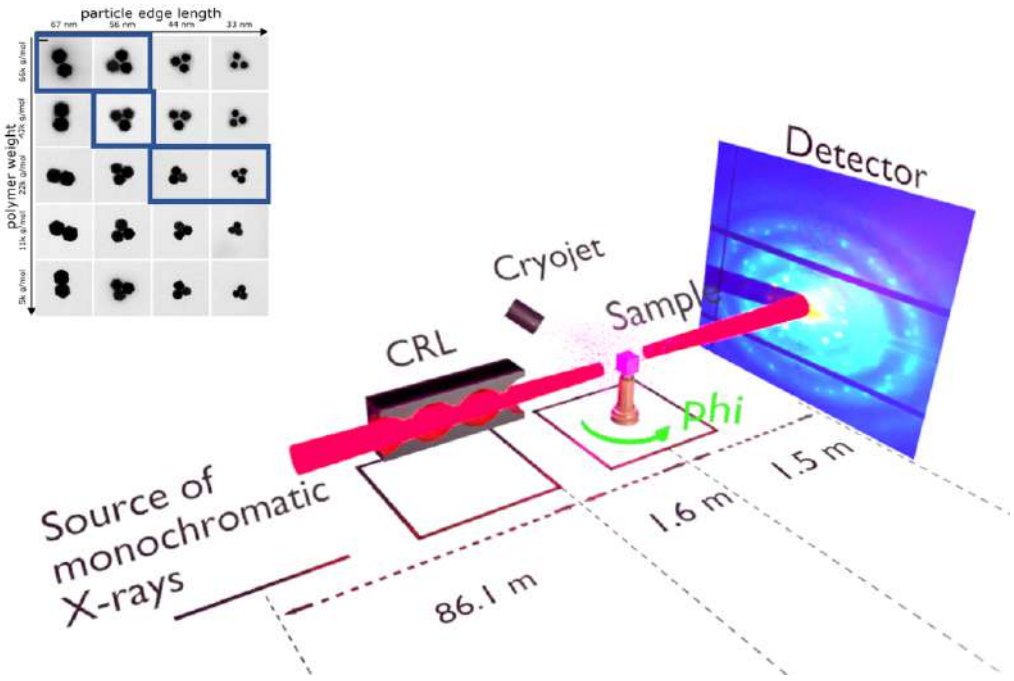

Figure 7.5: The experimental setup is depicted in a diagram. The Compound Refractive Lenses (CRL) concentrate an 8.3 keV monochromatic X-ray beam from the source to the sample. A liquid nitrogen cryostat was used to chill the sample. An X-ray Spectrum Lambda detector was positioned downstream at a distance of 1.5 m from the sample to measure the far-field diffraction patterns. Rotating the sample around the vertical axis produces a 3D diffraction map. In the inset, a TEM image of octahedral gold mesocrystals is shown. The blue boxes represent all the samples that were analyzed and highlighted in this section.

7.2.2 Analytical methodology

As the first analysis step, the 3D reciprocal space maps of octahedral Au samples were developed from the individual 2D scans, retrieved at different angles, as shown in Fig. 7.5. Fig. 7.5 highlights the 3D maps from the four investigated sample types. A 3D orthogonal grid was thus formed as the recorded 2D patterns were interpolated, giving them a voxel size of 0.0015 nm^{-1}. As the next step, the radial profile was determined, statistically representing the structure factor and form factor of nanoparticles composing the mesocrystalline grains, as shown in Fig. 7.6. Qualitatively, the radial profile highlights how the investigated sample scatters incident radiation at a given q-value, resembling the structure factor of the sample. Here, the scattered intensities at each q-value have been averaged over a range of q = [0.1:0.5] nm^{-1} with a step size of 0.001 nm^{-1}. Along with the structure factor, we can also determine the single particle scattering behavior at a given q-value. This

means that now we do not sum up the intensities, but we take a single expected value for each q position for the same q-range. The structure factor, represented by Fig. 7.6(a), is thus calculated by the angular averaging of the obtained 3D diffraction pattern at each momentum transfer position. Here, the peaks show the experimental Bragg peaks. On the contrary, Fig. 7.6(b) is constructed by acquiring the median of the angular average values at all the individual q-values, leading to the form factor curve.

The peaks across the radial profiles also provide us with the reference value of the q-space for the calculation of the cross-correlation values. Let's say the q_1 expressing the fixed value for sample O1 in the CCF calculation is shown in Fig. 7.6(a) with a dotted line. The cross-correlation function for the O1 sample was thus computed between the peak intensity at the q_1 position, corresponding to the brightest intensity, and the other momentum transfer values, q_2 in the region from 0.1-0.5 nm^{-1} with 0.001 nm^{-1} increments. The same analytical process is followed for all samples across all radial profiles accordingly. The reference q values for all samples are represented as q_1, q_2, q_3, q_4 and q_5.

As the proceeding step for the analysis part, Fig. 7.7 provides x-ray angular cross-correlation maps for Au specimens obtained experimentally. Here, they are represented by yellow spots that mark the correlation peaks appearing between the two respective Bragg peaks. The correlation map which is displayed by this cross-correlation gave the reading CCF(q_1, q_2, Δ). In the later step, the predicted peak positions with respect to these correlation peak coordinates for the geometrical model were determined.

By using the fitted geometrical model, the reciprocal and real space parameters for the samples were determined and highlighted in Table 7.11, along with the calculation of the uncertainties. Comparing the lattice parameter with the edge length of each sample will enable us to draw the conclusions of the CCF-based structural investigation. Looking at the case of O1, the experimental parameter (a = 66.8 nm) clearly conforms with the grain size, which is 67 nm. In terms of each calculated parameter, the corresponding uncertainty is attached to it. With an angle between equal bond faces of 60°, the FCC (primitive) structure can be confirmed in the reciprocal space and the BCC (primitive) in the real space structure when the retrieved real space parameters are $b_1 = b_2 = b_3 = b = 0.11nm^{-1}$.

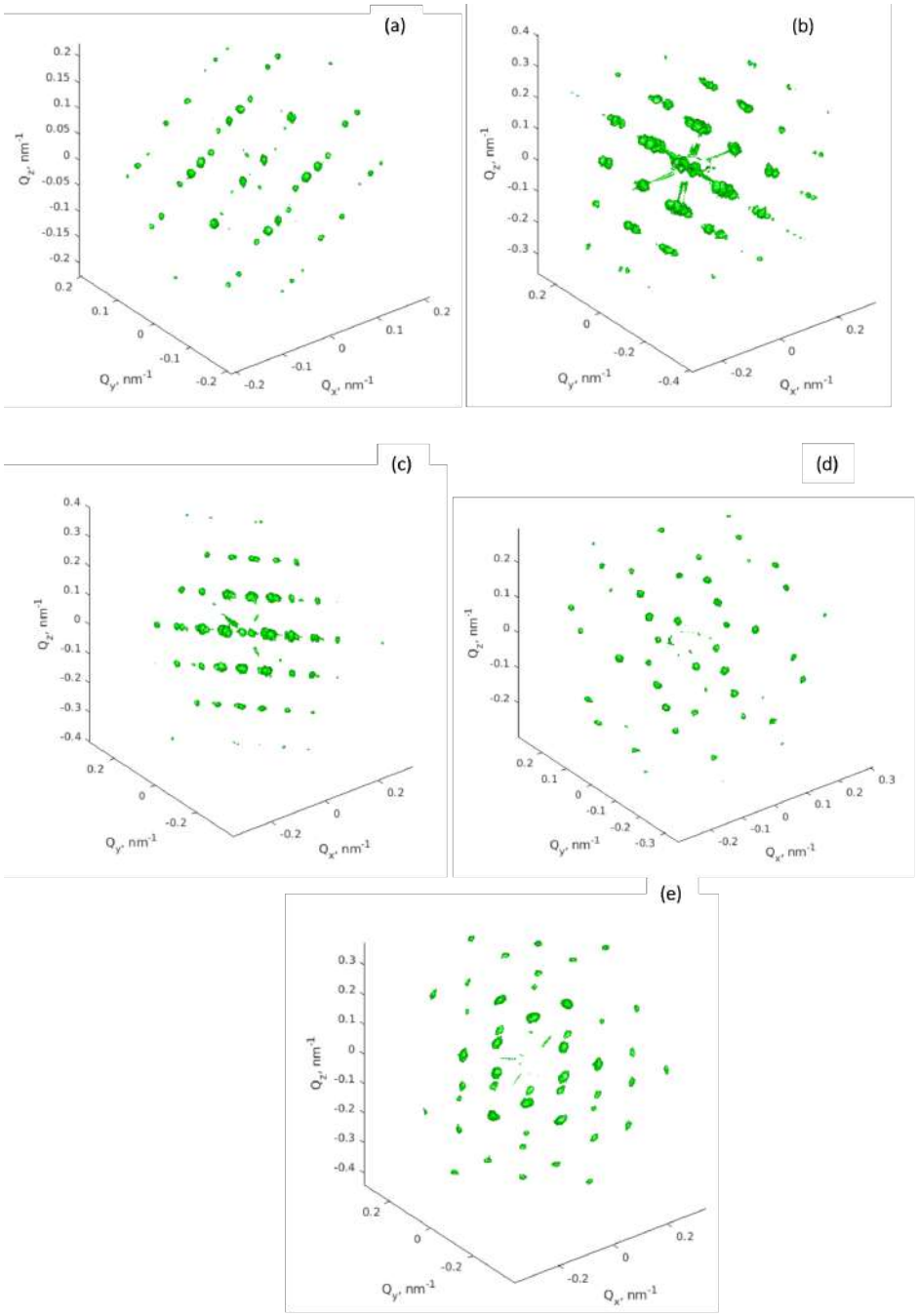

Figure 7.6: 3D reciprocal space maps of octahedral Au samples O1 (a), O2 (b), O3 (c), O4 (d), and O5 (d) measured at P23 beamline.

Such calculation process was repeated for each explored sample and all the parameters were derived along with their structure. In addition, the table also shows the peak values of all samples in the first height (which is considered as q_1 and depicted as a dotted line Fig. 7.6(a)) between them.

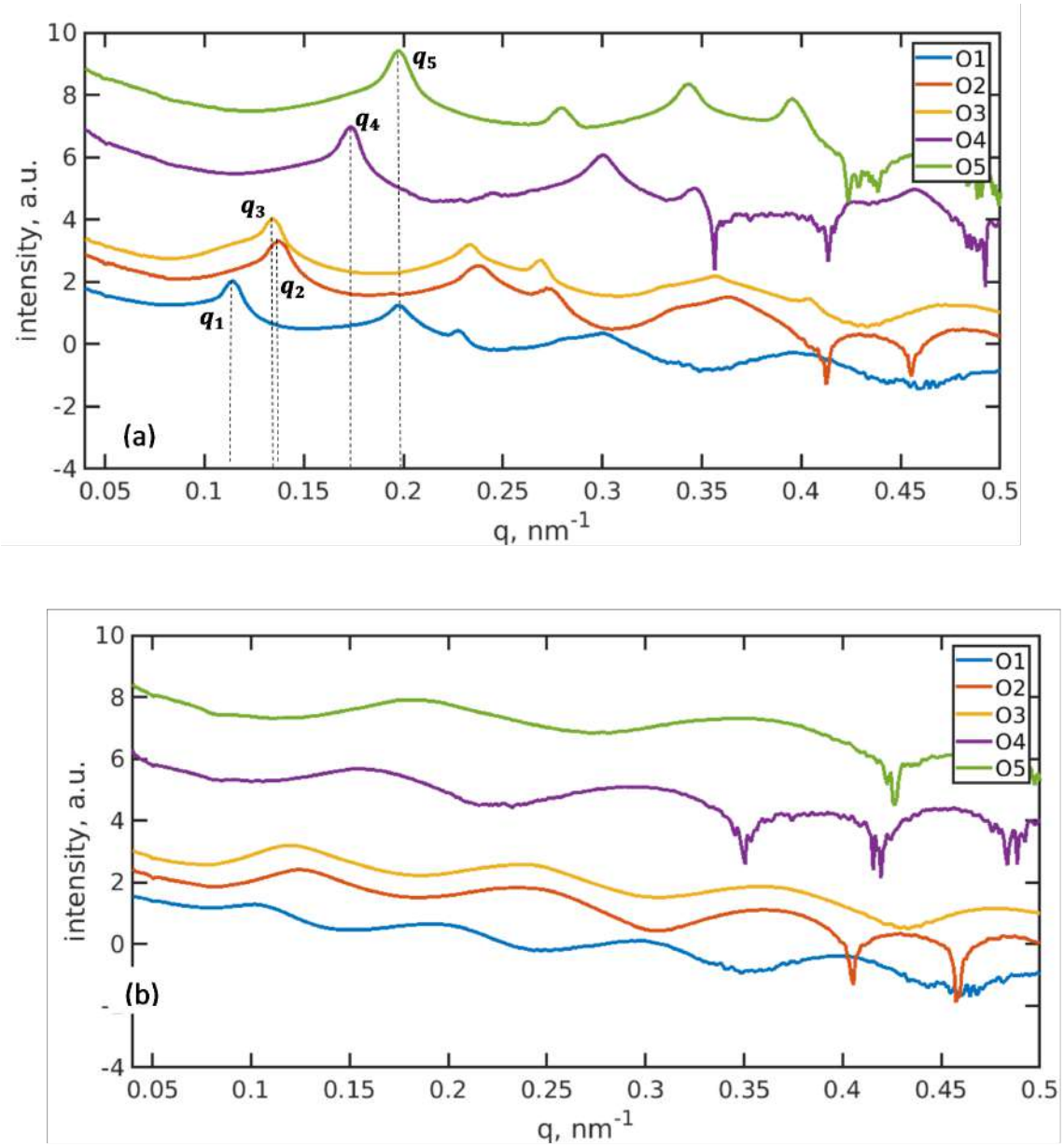

Figure 7.7: Structure factor (a) and form factor (b) for all samples measured at the P23 beamline. The different colors correspond to samples O1–O5. The first peak in all samples is indicated by vertical dotted lines. The curves are shifted by a multiplication factor of 2 for better visibilities.

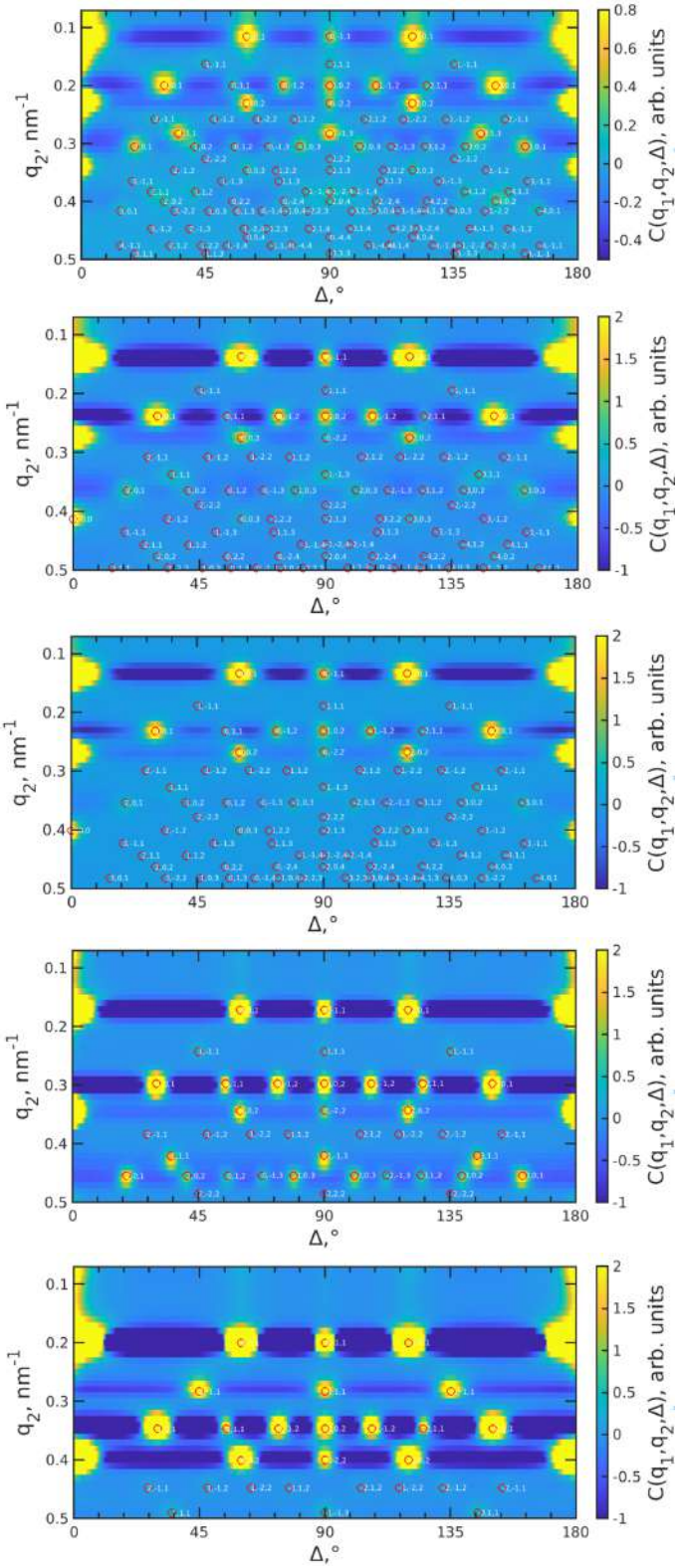

Figure 7.8: Angular x-ray cross-correlation maps C(q_1, q_2, δ) of experimental data for samples O1 (a), O2 (b), O3 (c), O4 (d) and O5 (e). Red dots represent the best model that fits the data. These correlation maps are obtained with the fixed momentum transfer q_1 corresponding to the first peak in Fig. 3 and varying momentum transfer q_2 from 0.1 nm^{-1} to 0.5 nm^{-1} with a step size of 0.001 nm^{-1}.

Table 7.1: Real Space and Reciprocal Space parameters

Samples	O1 1	O2 2	O3	O4	O5
b (nm^{-1})	0.11±0.01	0.13±0.01	0.13±0.01	0.17±0.02	0.20±0.02
Angle (degrees)	60±11.2	60±13.2	60±11.5	60±9.3	60±12.2
a (nm)	66.8±4	56±4.6	57.7±4.5	44.9±3.6	38.5±3.6
Angle (degrees)	109.5±4.6	109.5±5.4	109.5±4.7	109.5±3.8	109.5±5
First peak q-values (nm^{-1})	0.11	0.14	0.13	0.17	0.20

In summary, the structural feature is revealed by the angular X-ray cross-correlation analysis, and the lattice parameters were simultaneously established in the real and reciprocal space. To start with, we find the 3D reciprocal space maps of all Au mesocrystals for each of the samples, so that we get a complete picture of the whole diffraction pattern. Then, the radial was performed which was on an intensity vs q values basis, which in turn enabled us to identify the set of Braggs peaks obtained. The initial peak from the radial profile is the reference peak for the correlation CCF values. Firstly, cross-correlation maps were evaluated depending on the scattered intensities, stored in two q-values (q_1 and q_2), which were separated by an angular distance . The cross correlation between two Bragg peaks yields the CCF peaks in the 2D maps. Secondly, the geometrical model fitting was used to effectively deduce the real and reciprocal space parameters of the sample's data. To assess the precision, we did a Gaussian curve fitting for the values not only in real but also in reciprocal space. The analysis was successfully performed with mesocrystals of different sizes, and these calculated parameters were in good agreement with the corresponding edge lengths.

8 Appendix

8.1 Piezoelectric Supplementary Relations

The non-piezoelectric materials have independent mechanical and electrical behaviour. However, for piezoelectric materials, the electrical and mechanical behaviours are coupled, such that the stress, σ and strain, ϵ are related to each other, and are also related to the electric field, E and electrical displacement D. Starting from the fundamentals, for a piezoelectric material, the total net internal energy density is the summation of the mechanical and electrical work done, while ignoring the thermal effects. (for simplicity, we do not show the indices of the tensors in the equations below. Mathematically,)

$$dU = E_i dD_i - \sigma_{ij} \times d\epsilon_{ij} \tag{8.1}$$

Here, the internal energy $U(\epsilon_{ij}, D_k$ is the thermodynamic potential. Using the Legendre transformation, we can define three more thermodynamic potentials, as follows:

$$H = U - E_i D_i \tag{8.2}$$

$$F = U - \sigma_{ij}\epsilon_{ij} \tag{8.3}$$

$$G = U - \sigma_{ij}\epsilon_{ij} - E_k D_k \tag{8.4}$$

Where, H - enthalpy, F - Helmholtz free energy and G - Gibbs free energy in the notation of gaseous thermodynamics theory. Now using the differential form of the equation 5.7, 5.8 and 5.9, and utilizing relation from equation 5.6, one can find the

following mathematical relations:

$$dH = \sigma_{ij} \cdot d\epsilon_{ij} - D_i dE_i \tag{8.5}$$

$$dF = E_i dD_i - \epsilon_{ij} \cdot d\sigma_{ij} \tag{8.6}$$

$$dG = -\epsilon_{ij} \cdot d\sigma_{ij} - D_i dE_i \tag{8.7}$$

The H potential will lead to the stress formulation of the piezoelectric property, while the G potential will lead to the strain formulation. The above equations will also yield the stress and electric displacement as the derivative of H potential, as follows:

$$\sigma_{ij}(\epsilon, E) = (\frac{\partial H}{\partial \epsilon_{ij}})_E \tag{8.8}$$

$$D_i(\epsilon, E) = -(\frac{\partial H}{\partial E_i})_\epsilon \tag{8.9}$$

The subscript here resembles the constant parameter, while evaluating the variations of the other variable. Furthermore, derivative of the stress and displacement parameters (equations 5.13 and 5.14) depends on the change in the strain and the electric field accordingly. This gives us the electro-mechanically coupled piezoelectric constitutive equation. Mathematically,

$$d\sigma_{ij}(\epsilon_{kl}, E_m) = (\frac{\partial \sigma_{ij}}{\partial \epsilon_{kl}})_E d\epsilon_{kl} + (\frac{\partial \sigma_{ij}}{\partial E_k})_\epsilon dE_k \tag{8.10}$$

$$dD_i(\epsilon_{kl}, E_m) = (\frac{\partial D}{\partial \epsilon_{kl}})_E d\epsilon + (\frac{\partial D_i}{\partial E_k})_\epsilon dE_k \tag{8.11}$$

The above equations allow us to determine the mechanical stiffness and electric permittivity, as the material properties. Mathematically,

$$(\frac{\partial \sigma_{ij}}{\partial \epsilon_{kl}})_E = C_{ijkl} \tag{8.12}$$

$$(\frac{\partial D_i}{\partial E_j})_\epsilon = (\chi_{ij})_\epsilon \tag{8.13}$$

Moreover, the piezoelectric stress constant can be formulated as follows:

$$(-\frac{\partial \sigma_{jk}}{\partial E_i}) = (\frac{\partial D_i}{\partial \epsilon_{jk}}) = e_{ijk} \tag{8.14}$$

The piezoelectric formulation in an electro-mechanically coupled material is thus given as:

$$\sigma_{ij}(\epsilon, E) = (c_{ijkl})^E \cdot \epsilon_{kl} - e_{ki} \cdot E_k \tag{8.15}$$

$$D_i(\epsilon, E) = e_{ijk}\epsilon_{jk} + (\chi_{ik})^\epsilon \cdot E_k \tag{8.16}$$

9 Conclusions and outlook

This thesis is devoted to the utilization of the X-ray diffraction science in order to perform two broad research segments. While we covered the theoretical aspects of the underlying physics in the initial chapters of this thesis, we also covered the concepts of piezoelectricity, dynamic simulation analysis, cross-correlation analysis, and voltage-induced strain variations. In terms of the analysis of voltage-induced strain variations, we analyzed the experimental datasets recorded at MAXIV and PETRA III over the proposed sample structure. The experimental results highlighted the presence of multiple NW structures, leading to multiple diffraction peaks within close proximity of each other. The outcome was a dispersed reaction in which the individual peaks were more prevalent and the peaks overlapped primarily. As a result, the voltage-induced variations over the diffraction peaks were not found to be reversible in nature. To better quantify the strain variations within the sample structure, it was essential to understand the sample's behavior. We did this analysis via simulation-based studies and 3D analysis using COMSOL Multiphysics. We performed several levels of analysis, aiming at the stepwise behavior of the sample under different configurations. The analysis was done in 4 broad segments. In Analysis 1, a four-layer model was utilized, with voltage applied to the structure but without any misfit strain. This setup aimed to investigate the effects of voltage on the structural integrity and behavior of the layered model. Analysis 2 also employed a four-layer model but differed by incorporating both applied voltage and misfit strain. This combination allowed for a more comprehensive study of how both factors simultaneously influence the structure. Analysis 3 shifted focus to a nanowire (NW) sample.

In this analysis, the voltage was applied to the nanowire sample without introducing a misfit strain. This setup provided insights into the response of nanowire structures to electrical stimulation alone. Lastly, Analysis 4 examined a nanowire sample with both applied voltage and misfit strain. This comprehensive analysis aimed to understand the combined effects of electrical and mechanical stresses on the nanowire's structural properties.

The 3D model development of the investigated sample and the simulations were performed while discussing the variations across key process parameters. While profiling the changes in the potential changes across the layers in a top-bottom approach, we analyzed the following parameters: 1) The change in applied voltage potential to understand how the applied voltage is applied to the sample. We targeted the maximum voltage drop across the piezoelectric HZO layer only, as that would result in maximum induced strain across the layer and sample. The next analysis was done on the variations in the displacement field across the z (perpendicular to the sample) component and the x (parallel to the sample) component of the line profile. Moving forward, the stress and strain variations along the x and z components were then retrieved and analyzed to understand the behavior of our sample and the impact of the applied voltage cycles on the stress/strain profiles. This induced strain is then expected to cause variations in the diffraction peaks, which we aim to observe and analyze in the experimental readings.

Necessary boundary conditions were applied, allowing the sample to be rigid as a body, yet allowing it to be deformed in a vertical direction. Similarly, net zero stress was ensured, as no external force was applied to the structure. This was achieved by analyzing the behavior across different structural zones and understanding their variations, which tend to cause a net zero effect in the absence of any external force. The experimental analysis, though complex, provided us with the possibility of performing peak splitting for individual scans in order to investigate their response to variations due to applied voltage cycles.

We successfully performed the angular X-ray cross-correlation analysis (AXCCA) over meso-crystals of different size configurations. We highlighted the step-wise implementation of the AXCCA technique, starting with the data pre-processing of 2D scans, 3D dataset development, radial profile determination, and then calculating the correlation peaks between the diffraction intensities in order to reveal the structural parameters. As the validation step, the mathematical model was fitted using the reciprocal space parameters over the experimentally retrieved correlation peaks. The best possible fit between the theoretical model and that of experimental results would yield the structural information of the samples under investigation. The analysis was performed over different samples of varying edge lengths in order to evaluate the applicability of this technique over different size configurations.

The structural characterization of Au mesocrystals across five different samples was performed using angular X-ray cross-correlation analysis (AXCCA). The analysis

reveals a clear inverse relationship between the reciprocal lattice parameter and the real space lattice parameter.

In the first sample, the reciprocal space angle and the real space angle were measured, along with a peak in the radial intensity profile and a theoretical edge length. The second sample displayed similar measurements for these parameters, with slight variations. The third sample had consistent angles and peaks, with a theoretical edge close to that of the second sample. For the fourth sample, the measurements showed a higher reciprocal lattice parameter and a shorter theoretical edge length. Lastly, the fifth sample presented the highest reciprocal lattice parameter and the shortest theoretical edge.

Across all samples, the first peak in the radial intensity profile consistently matched the reciprocal lattice parameter, while the real space angle remained stable, suggesting a consistent unit cell structure.

These results highlight the variations in the structural features of different samples, underscoring the effectiveness of AXCCA in providing precise structural characterization at the nanoscale. The consistent measurements of angles and the variations in lattice parameters reflect the unique structural properties of each sample.

Overall, the thesis worked on two different research segments. The piezoelectric analysis of the HZO layer and multi-layered NW-based sample design also focused on simulation-based studies and experimental trials, while other segment on AXCCA was primarily focusing on the key experimental analysis and structural investigation.

Acknowledgements

I would like to express my deepest gratitude to my supervisors, Dr. Ivan Vartaniants and Prof. Dr. Anders Mikkelsen from Lund University, for their invaluable guidance and support throughout my PhD journey. Dr. Ivan Vartaniants, your unwavering mentorship and insightful advice have been instrumental in shaping this thesis. Your dedication and encouragement have been a constant source of inspiration.

I am also immensely grateful to Prof. Dr. Mathias Wallin from Lund University for his expertise and assistance in the field of data simulation using COMSOL. Your technical guidance has significantly contributed to the success of this work.

My heartfelt thanks go to my former colleagues, Dr. Dameli Assalauova, Dr. Dmitry Lapkin, Dr. Ruslan Khubbutdinov, and Dr. Dmitry Dzhigaev, for their support and encouragement at the beginning of this journey. Your camaraderie and advice helped lay the foundation for this thesis.

I would like to extend my appreciation to the team at Lund University, particularly Nelia Zaiats and Dr. Dmitry Dzhigaev, for their invaluable help during the experiments and beamtimes. Your collaboration and technical support have been crucial in achieving the research outcomes presented here.

I am also thankful to my current colleagues, Dr. Bihan Wang, Dr. Gerard Hinsley, and Dr. Kuanhoon, for their continuous support and encouragement throughout my PhD. Your positive and supportive nature has made this journey more manageable and enjoyable.

Special thanks to my close friend Dr. Ayush Sharma for his unwavering support in every aspect of my life. Your friendship has been a pillar of strength during the challenging times of this journey.

Finally, I am profoundly grateful to my parents and my brother Siddharth for their lifelong support and belief in me. Your love and encouragement have been the bedrock of my achievements, and I could not have reached this milestone without you.

Thank you all for being part of this journey and for your significant contributions to the completion of this thesis.

List of Abbreviations

3D Three-dimensional

ACF Autocorrelation function

CDI Coherent Diffraction Imaging

CXDI Coherent X-ray Diffraction Imaging

CRL Compound refractive lenses

DOC Degree of Coherence

DLSR Diffraction-limited storage ring

EuXFEL European X-ray Free-electron Laser

FEL Free-electron Laser

FWHM Full Width at Half Maximum

PAL-XFEL Pohang Accelerator Laboratory - X-ray Free-electron Laser

SASE Self Amplification of Spontaneous Emission

SSR Synchrotron storage ring

XES X-ray Emission Spectroscopy

XFEL X-ray Free-electron Laser
] 2D Two-dimensional

3D Three-dimensional

ACF Autocorrelation function

CDI Coherent Diffraction Imaging

CXDI Coherent X-ray Diffraction Imaging

CRL Compound refractive lenses

DOC Degree of Coherence

DLSR Diffraction-limited storage ring

EuXFEL European X-ray Free-electron Laser

FEL Free-electron Laser

FWHM Full Width at Half Maximum

PAL-XFEL Pohang Accelerator Laboratory - X-ray Free-electron Laser

SASE Self Amplification of Spontaneous Emission

SSR Synchrotron storage ring

XES X-ray Emission Spectroscopy

XFEL X-ray Free-electron Laser

Own Publications

Publication directly related to this thesis

- Dmitry Lapkin, Shweta Singh, Felizitas Kirner, Sebastian Sturm, Dameli Assalauova, Alexandr Ignatenko, Thomas Wiek, Thomas Gemming, Axel Lubk, Knut M uller-Caspary, Azat Khadiev, Dmitri Novikov, Elena V. Sturm, and Ivan A. Vartanyants. Revealing the Impact of Polystyrene Functionalization of Au Octahedral Nanocrystals of Different Sizes on the Formation and Structure of Mesocrystals. *ChemNanoMat*, 9(12):e202300336, 2023. eprint: https://onlinelibrary.wiley.com/doi/pdf/10.1002/cnma.202300336.

Bibliography

[1] Charles Kittel. *Introduction to Solid State Physics*. Wiley, Hoboken, NJ, 8th edition, 2005.

[2] Max Born and Emil Wolf. *Principles of Optics : Electromagnetic Theory of Propagation, Interference and Diffraction of Light,*. Cambridge ; New York : Cambridge University Press, 6th edition, 1999.

[3] Shi-Hai Wei, Bo Jing, Xue-Ying Zhang, Jin-Yu Liao, Chen-Zhi Yuan, Bo-Yu Fan, Chen Lyu, Dian-Li Zhou, You Wang, Guang-Wei Deng, Hai-Zhi Song, Daniel Oblak, Guang-Can Guo, and Qiang Zhou. Towards Real-World Quantum Networks: A Review. *Laser & Photonics Reviews*, 16(3), 2022.

[4] Neil W. Ashcroft, N. David Mermin. *Solid State Physics*, New York, 1st edition, 1976.

[5] John Sydney Blakemore. *Semiconductor Statistics, A volume in International Series of Monographs on Semiconductors* . Elsevier, 1962.

[6] Jeffrey Hesler, Rohit Prasankumar, and Jerome Tignon. Advances in terahertz solid-state physics and devices. *Journal of Applied Physics*, 126(11), September 2019.

[7] John Michael David Coey. *Magnetism and Magnetic Materials*. Cambridge University Press, Cambridge, 2010.

[8] Jonathan Schmidt, Mário R. G. Marques, Silvana Botti, and Miguel A. L. Marques. Recent advances and applications of machine learning in solid-state materials science. *Computational Materials*, 5(1):1–36, August 2019.

[9] Mark Fox. *Optical Properties of Solids*. Oxford Master Series in Physics. Oxford University Press, Oxford, New York, 2nd edition, 2010.

[10] Paul F. McMillan, Olga Shebanova, Dominik Daisenberger, Raul Quesada Cabrera, Edward Bailey, Andrew Hector, Victoria Lees, Denis Machon, Andrea Sella, and Mark Wilson. Metastable phase transitions and structural

transformations in solid-state materials at high pressure. *Phase Transitions*, 80(10-12):1003–1032, October 2007.

[11] Willy Cahyadi, Yeon-Ho Chung, Zabih Ghassemlooy, and Navid Bani Hassan. Optical Camera Communications: Principles, Modulations, Potential and Challenges. *Electronics*, 9:1339, August 2020.

[12] Electromagnetic Spectrum Information | https://www.twinkl.co.th/teaching-wiki/electromagnetic-spectrum.

[13] Octavia Brayley, Dr Martin How, and Dr Andrew Wakefield. Biological Effects of Light Pollution on Terrestrial and Marine Organisms. *International Journal of Sustainable Lighting*, 24(1):13–38, March 2022.

[14] Dmitry Chizhik, Jonathan Ling, and Reinaldo Valenzuela. The effect of electric field polarization on indoor propagation, <>iIEEE</i>. 1:459–462, October 1998.

[15] Peter Schmüser, Martin Dohlus, Jörg Rossbach, and Christopher Behrens. *Free-Electron Lasers in the Ultraviolet and X-Ray Regime: Physical Principles, Experimental Results, Technical Realization*. Springer Tracts in Modern Physics. Springer International Publishing, 2nd edition, 2014.

[16] Christiane Mellak, Klaus Krischan, and A. Muetze. Synchronous Reluctance Machines as Drives for Rotary Anode X-Ray Tubes-A Feasibility Study, 2613-2618, International Conference on Electrical Machines, *ICEM*. September 2018.

[17] J Als-Nielsen and Des McMorrow. *Elements of Modern X-ray Physics*. 2nd edition, 2011.

[18] Balraj Singh Saini and Raminder Kaur. X-ray diffraction, Handbook of Modern Coating Technologies, *85-141*. Elsevier, Amsterdam, January 2021.

[19] X-ray Production, Tubes, and Generators, https://radiologykey.com/x-ray-production-tubes-and-generators.

[20] Practical Electron Microscopy and Database | https://www.globalsino.com/EM/.

[21] Ruslan Khubbutdinov. *Statistical Properties of the X-ray Radiation at Large Scale Facilities*. PhD thesis, Dissertation, University of Hamburg, 2022.

[22] Shigemi Sasaki, Kazunori Kakuno, Takeo Takada, Taihei Shimada, Ken-ichi

Yanagida, and Yoshikazu Miyahara. Design of a new type of planar undulator for generating variably polarized radiation. *Nuclear Instruments and Methods in Physics Research Section A: Accelerators, Spectrometers, Detectors and Associated Equipment*, 331(1):763–767, 1993.

[23] David Attwood and Anne Sakdinawat. *X-Rays and Extreme Ultraviolet Radiation: Principles and Applications*. Cambridge University Press, Cambridge, 2 edition, 2017.

[24] Keith Codling and Robert Madden. New Rydberg Series in Molecular Oxygen near 500 Å. *The Journal of Chemical Physics*, 42(11):3935–3938, July 2004.

[25] Ruslan Kurta, Massimo Altarelli, Edgar Weckert, and Ivan Vartaniants. X-ray cross-correlation analysis applied to disordered two-dimensional systems. *Physical Review B*, 85(18):184–204, May 2012.

[26] Helmut Wiedemann. Synchrotron Radiation, *Particle Accelerator Physics*, 647–686. Springer Berlin Heidelberg, Berlin, Heidelberg, 2003.

[27] Philip Willmott. *An Introduction to Synchrotron Radiation: Techniques and Applications*. Wiley Online Books, 1st edition, 2019.

[28] Ivan A. Vartanyants and Andrej Singer. Coherence Properties of Third-Generation Synchrotron Sources and Free-Electron Lasers. In Eberhard Jaeschke, Shaukat Khan, Jochen R. Schneider, and Jerome B. Hastings, editors, *Synchrotron Light Sources and Free-Electron Lasers: Accelerator Physics, Instrumentation and Science Applications*. Springer International Publishing, 2014.

[29] The Use of Light and Colour in Modern Technology, How do synchrotrons work, http://todaystechnologyy.weebly.com/how-do-they-work1.html.

[30] Mikael Eriksson and J. Friso van der Veen. Diffraction-Limited Storage Rings and New Science Opportunities, *Journal of Synchrotron Radiation*. 21(5), 2014.

[31] R. Hettel. DLSR design and plans: an international overview. *Journal of Synchrotron Radiation*, 21(5):843–855, September 2014.

[32] R. Khubbutdinov, A. P. Menushenkov, and I. A. Vartanyants. Coherence properties of the high-energy fourth-generation X-ray synchrotron sources. *Journal of Synchrotron Radiation*, 26(6):1851–1862, November 2019.

[33] J. Stöhr. Two-Photon X-Ray Diffraction. *Physical Review Letters*, 118(2):024801, January 2017.

[34] Nastasia Mukharamova. *Mesoscopic materials studied with advanced X-ray scattering methods*, Dissertation, University of Hamburg, 2020.

[35] Christian G. Schroer, Ilya Agapov, Werner Brefeld, Reinhard Brinkmann, Yong-Chul Chae, Hung-Chun Chao, Mikael Eriksson, Joachim Keil, Xavier Nuel Gavaldà, Ralf Röhlsberger, Oliver H. Seeck, Michael Sprung, Markus Tischer, Rainer Wanzenberg, and Edgar Weckert. PETRA IV: The ultralow-emittance source project at DESY. *Journal of Synchrotron Radiation*, 25(5):1277–1290, August 2018.

[36] Pedro Tavares, Simon Leemann, Magnus Sjöström, and A. Andersson. The MAX IV storage ring project. *Journal of Synchrotron Radiation*, 21:862–877, September 2014.

[37] Weckert E. The potential of future light sources to explore the structure and function of matter. *IUCrJ*, 2(2), February 2015.

[38] P. Emma, R. Akre, J. Arthur, R. Bionta, C. Bostedt, J. Bozek, A. Brachmann, P. Bucksbaum, R. Coffee, F. J. Decker, Y. Ding, D. Dowell, S. Edstrom, A. Fisher, J. Frisch, S. Gilevich, J. Hastings, G. Hays, Ph. Hering, Z. Huang, R. Iverson, H. Loos, M. Messerschmidt, A. Miahnahri, S. Moeller, H. D. Nuhn, G. Pile, D. Ratner, J. Rzepiela, D. Schultz, T. Smith, P. Stefan, H. Tompkins, J. Turner, J. Welch, W. White, J. Wu, G. Yocky, and J. Galayda. First lasing and operation of an ångstrom-wavelength free-electron laser. *Nature Photonics*, 4:641–647, September 2010.

[39] V. Ayvazyan, N. Baboi, J. Bähr, Vladimir Balandin, Bolko Beutner, A. I., Ilja Bohnet, A. Bolzmann, R Brinkmann, Oleg Brovko, Jean-Paul Carneiro, Sara Casalbuoni, Michele Castellano, Pablo Castro, L. Catani, Enrica Chiadroni, S. Choroba, Alessandro Cianchi, H. Delsim-Hashemi, and K. Zapfe. First operation of a free-electron laser generating GW power radiation at 32 nm wavelength. *The European Physical Journal D*, 37:297, November 2005.

[40] Tetsuya Ishikawa, Hideki Aoyagi, Takao Asaka, Yoshihiro Asano, Noriyoshi Azumi, Teruhiko Bizen, Hiroyasu Ego, Kenji Fukami, Toru Fukui, Yukito Furukawa, Shunji Goto, Hirofumi Hanaki, Toru Hara, Teruaki Hasegawa, Takaki Hatsui, Atsushi Higashiya, Toko Hirono, Naoyasu Hosoda, Miho Ishii, Takahiro Inagaki, Yuichi Inubushi, Toshiro Itoga, Yasumasa Joti, Masahiro Kago, Takashi Kameshima, Hiroaki Kimura, Yoichi Kirihara, Akio Kiyomichi, Toshiaki Kobayashi, Chikara Kondo, Togo Kudo, Hirokazu Maesaka, Xavier M.

Maréchal, Takemasa Masuda, Shinichi Matsubara, Takahiro Matsumoto, Tomohiro Matsushita, Sakuo Matsui, Mitsuru Nagasono, Nobuteru Nariyama, Haruhiko Ohashi, Toru Ohata, Takashi Ohshima, Shun Ono, Yuji Otake, Choji Saji, Tatsuyuki Sakurai, Takahiro Sato, Kei Sawada, Takamitsu Seike, Katsutoshi Shirasawa, Takashi Sugimoto, Shinsuke Suzuki, Sunao Takahashi, Hideki Takebe, Kunikazu Takeshita, Kenji Tamasaku, Hitoshi Tanaka, Ryotaro Tanaka, Takashi Tanaka, Tadashi Togashi, Kazuaki Togawa, Atsushi Tokuhisa, Hiromitsu Tomizawa, Kensuke Tono, Shukui Wu, Makina Yabashi, Mitsuhiro Yamaga, Akihiro Yamashita, Kenichi Yanagida, Chao Zhang, Tsumoru Shintake, Hideo Kitamura, and Noritaka Kumagai. A compact X-ray free-electron laser emitting in the sub-ångström region. *Nature Photonics*, 6(8):540–544, August 2012.

[41] In Soo Ko, Heung-Sik Kang, Hoon Heo, Changbum Kim, Gyujin Kim, Chang-Ki Min, Haeryong Yang, Soung Youl Baek, Hyo-Jin Choi, Geonyeong Mun, Byoung Ryul Park, Young Jin Suh, Dong Cheol Shin, Jinyul Hu, Juho Hong, Seonghoon Jung, Sang-Hee Kim, KwangHoon Kim, Donghyun Na, Soung Soo Park, Yong Jung Park, Young Gyu Jung, Seong Hun Jeong, Hong Gi Lee, Sangbong Lee, Sojeong Lee, Bonggi Oh, Hyung Suck Suh, Jang-Hui Han, Min Ho Kim, Nam-Suk Jung, Young-Chan Kim, Mong-Soo Lee, Bong-Ho Lee, Chi-Won Sung, Ik-Su Mok, Jung-Moo Yang, Yong Woon Parc, Woul-Woo Lee, Chae-Soon Lee, Hocheol Shin, Ji Hwa Kim, Yongsam Kim, Jae Hyuk Lee, Sang-Youn Park, Jangwoo Kim, Jaeku Park, Intae Eom, Seungyu Rah, Sunam Kim, Ki Hyun Nam, Jaehyun Park, Jaehun Park, Sangsoo Kim, Soonnam Kwon, Ran An, Sang Han Park, Kyung Sook Kim, Hyojung Hyun, Seung Nam Kim, Seonghan Kim, Chung-Jong Yu, Bong-Soo Kim, Tai-Hee Kang, Kwang-Woo Kim, Seung-Hwan Kim, Hee-Seock Lee, Heung-Soo Lee, Ki-Hyeon Park, Tae-Yeong Koo, Dong-Eon Kim, and Ki Bong Lee. Construction and Commissioning of PAL-XFEL Facility. *Applied Sciences*, 7(5):479, May 2017.

[42] Romain Ganter, Rafael Abela, Hans Heinrich Braun, Terry Garvey, Bruce Patterson, Marco Pedrozzi, Luc Patthey, and Sven Reiche. *SwissFEL - Conceptual design report, Paul Scherrer Institute (PSI).* Technical report, Switzerland, 2010.

[43] Rafael Abela, A. Aghababyan, M. Altarelli, Carlo Altucci, Gayane Amatuni, Philip Anfinrud, Patrick Audebert, V. Ayvazyan, N. Baboi, J. Bähr, Vladimir Balandin, R. Bandelmann, Juergen Becker, Bolko Beutner, C. Blome, Ilja

Bohnet, A. Bolzmann, Christoph Bostedt, Y. Bozhko, and Ryszard Romaniuk. *XFEL: The European X-Ray Free-Electron Laser - Technical Design Report*. 2006.

[44] John M. J. Madey. Stimulated Emission of Bremsstrahlung in a Periodic Magnetic Field. *Journal of Applied Physics*, 42(5):1906–1913, April 1971.

[45] D. A. G. Deacon, L. R. Elias, J. M. J. Madey, G. J. Ramian, H. A. Schwettman, and T. I. Smith. First Operation of a Free-Electron Laser. *Physical Review Letters*, 38(16):892–894, April 1977.

[46] Anatolii Mikhailovich Kondratenko and Evgenii Leonidovich Saldin. Generating Of Coherent Radiation By A Relativistic Electron beam In An ondulator. 10:207–216, 1980.

[47] R. Bonifacio and F. Casagrande. The superradiant regime of a free electron laser. *Nuclear Instruments and Methods in Physics Research Section A: Accelerators, Spectrometers, Detectors and Associated Equipment*, 239(1):36–42, August 1985.

[48] Aliaksei Halavanau, Andrei Benediktovitch, Alberto A. Lutman, Daniel DePonte, Daniele Cocco, Nina Rohringer, Uwe Bergmann, and Claudio Pellegrini. Population inversion X-ray laser oscillator. *Proceedings of the National Academy of Sciences*, 117(27):15511–15516, July 2020.

[49] Peter Krogstrup, Henrik Ingerslev Jørgensen, Martin Heiss, Olivier Demichel, Jeppe V. Holm, Martin Aagesen, Jesper Nygard, and Anna Fontcuberta i Morral. Single-nanowire solar cells beyond the Shockley–Queisser limit. *Nature Photonics*, 7(4):306–310, April 2013.

[50] Kelly Gaffney and Henry N Chapman. Imaging atomic structure and dynamics with ultrafast x-ray scattering. *Science*, 316(5830):1444–1448, June 2007.

[51] O. Ciricosta, S. M. Vinko, B. Barbrel, D. S. Rackstraw, T. R. Preston, T. Burian, J. Chalupský, B. I. Cho, H. K. Chung, G. L. Dakovski, K. Engelhorn, V. Hájková, P. Heimann, M. Holmes, L. Juha, J. Krzywinski, R. W. Lee, S. Toleikis, J. J. Turner, U. Zastrau, and J. S. Wark. Measurements of continuum lowering in solid-density plasmas created from elements and compounds. *Nature Communications*, 7:11713, May 2016.

[52] Peter Vester, Ivan A. Zaluzhnyy, Ruslan P. Kurta, Klaus B. Møller, Elisa Biasin, Kristoffer Haldrup, Martin Meedom Nielsen, and Ivan A. Vartanyants.

Ultrafast structural dynamics of photo-reactions observed by time-resolved x-ray cross-correlation analysis. *Structural Dynamics*, 6(2):024301, March 2019.

[53] Kathinka Gerlinger, Bastian Pfau, Felix Büttner, Michael Schneider, Lisa-Marie Kern, Josefin Fuchs, Dieter Engel, Christian Günther, Mantao Huang, Ivan Lemesh, Lucas Caretta, Alexandra Churikova, Piet Hessing, Christopher Klose, Christian Strüber, Clemens Schmising, Siying Huang, Angela Wittmann, Kai Litzius, and Stefan Eisebitt. Application concepts for ultrafast laser-induced skyrmion creation and annihilation. *Applied Physics Letters*, 118:192403, May 2021.

[54] Young Yong Kim, Luca Gelisio, Giuseppe Mercurio, Siarhei Dziarzhytski, Martin Beye, Lars Bocklage, Anton Classen, Christian David, Oleg Yu. Gorobtsov, Ruslan Khubbutdinov, Sergey Lazarev, Nastasia Mukharamova, Yuri N. Obukhov, Benedikt Rösner, Kai Schlage, Ivan A. Zaluzhnyy, Günter Brenner, Ralf Röhlsberger, Joachim von Zanthier, Wilfried Wurth, and Ivan A. Vartanyants. Ghost imaging at an XUV free-electron laser. *Physical Review A*, 101(1):013820, January 2020.

[55] Raimund Schneider, Thomas Mehringer, Giuseppe Mercurio, Lukas Wenthaus, Anton Classen, Günter Brenner, Oleg Gorobtsov, Adrian Benz, Daniel Bhatti, Lars Bocklage, Birgit Fischer, Sergey Lazarev, Yuri Obukhov, Kai Schlage, Petr Skopintsev, Jochen Wagner, Felix Waldmann, Svenja Willing, Ivan Zaluzhnyy, Wilfried Wurth, Ivan A. Vartanyants, Ralf Röhlsberger, and Joachim von Zanthier. Quantum imaging with incoherently scattered light from a free-electron laser. *Nature Physics*, 14(2):126–129, February 2018.

[56] Corinna Thiel, Thierry Bastin, John Martin, Enrique Solano, J. von Zanthier, and Girish S. Agarwal. Quantum Imaging with Incoherent Photons. *Physical Review Letters*, 99(13):133603, September 2007.

[57] A. Singer, F. Sorgenfrei, A. P. Mancuso, N. Gerasimova, O. M. Yefanov, J. Gulden, T. Gorniak, T. Senkbeil, A. Sakdinawat, Y. Liu, D. Attwood, S. Dziarzhytski, D. D. Mai, R. Treusch, E. Weckert, T. Salditt, A. Rosenhahn, W. Wurth, and I. A. Vartanyants. Spatial and temporal coherence properties of single free-electron laser pulses. *Optics Express*, 20(16):17480–17495, July 2012.

[58] O. Yu. Gorobtsov, G. Mercurio, G. Brenner, U. Lorenz, N. Gerasimova, R. P. Kurta, F. Hieke, P. Skopintsev, I. Zaluzhnyy, S. Lazarev, D. Dzhigaev, M. Rose,

A. Singer, W. Wurth, and I. A. Vartanyants. Statistical properties of a free-electron laser revealed by Hanbury Brown–Twiss interferometry. *Physical Review A*, 95(2):023843, February 2017.

[59] A. Singer, U. Lorenz, F. Sorgenfrei, N. Gerasimova, J. Gulden, O. M. Yefanov, R. P. Kurta, A. Shabalin, R. Dronyak, R. Treusch, V. Kocharyan, E. Weckert, W. Wurth, and I. A. Vartanyants. Hanbury Brown–Twiss Interferometry at a Free-Electron Laser. *Physical Review Letters*, 111(3):034802, July 2013.

[60] M. Hollstein, K. Mertens, S. Klumpp, N. Gerken, S. Palutke, I. Baev, G. Brenner, S. Dziarzhytski, M. Meyer, W. Wurth, D. Pfannkuche, and M. Martins. Ultrafast charge redistribution in small iodine containing molecules. *New Journal of Physics*, 21(3):033017, March 2019.

[61] A. Madsen, J. Hallmann, G. Ansaldi, T. Roth, W. Lu, C. Kim, U. Boesenberg, A. Zozulya, J. Möller, R. Shayduk, M. Scholz, A. Bartmann, A. Schmidt, I. Lobato, K. Sukharnikov, M. Reiser, K. Kazarian, and I. Petrov. Materials Imaging and Dynamics (MID) instrument at the European X-ray Free-Electron Laser Facility. *Journal of Synchrotron Radiation*, 28(2):637–649, March 2021.

[62] C. Kim, M. Scholz, and A. Madsen. The influence of strain on image reconstruction in Bragg coherent X-ray diffraction imaging and ptychography. *Journal of Synchrotron Radiation*, 28(4):1159–1165, July 2021.

[63] Felix Lehmkühler, Francesco Dallari, Avni Jain, Marcin Sikorski, Johannes Möller, Lara Frenzel, Irina Lokteva, Grant Mills, Michael Walther, Harald Sinn, Florian Schulz, Michael Dartsch, Verena Markmann, Richard Bean, Yoonhee Kim, Patrik Vagovic, Anders Madsen, Adrian P. Mancuso, and Gerhard Grübel. Emergence of anomalous dynamics in soft matter probed at the European XFEL. *Proceedings of the National Academy of Sciences*, 117(39):24110–24116, September 2020.

[64] Francesco Dallari, Mario Reiser, Irina Lokteva, Avni Jain, Johannes Möller, Markus Scholz, Anders Madsen, Gerhard Grübel, Fivos Perakis, and Felix Lehmkühler. Analysis Strategies for MHz XPCS at the European XFEL. *Applied Sciences*, 11(17):8037, January 2021.

[65] Felix Lehmkühler, Wojciech Roseker, and Gerhard Grübel. From Femtoseconds to Hours—Measuring Dynamics over 18 Orders of Magnitude with Coherent X-rays. *Applied Sciences*, 11(13):6179, January 2021.

[66] Roman Shayduk and Peter Gaal. R. Shayduk, P. Gaal, Transition regime in

the ultrafast laser heating of solids, Journal of Applied Physics, 2020. *Journal of Applied Physics*, 2020.

[67] Juris Purans, Alexey Pavlovich Menushenkov, Stanislav Besedin, Andrey A. Ivanov, Vasily S Minkov, Inga Pudza, Alexei Kuzmin, Konstantin Klementiev, Sakura Pascarelli, O. Mathon, Angelika Rosa, Tetsuo Irifune, and M. I. Eremets. Local electronic structure rearrangements and strong anharmonicity in YH3 under pressures up to 180 GPa. *Nature Communications*, 12(1):1765, March 2021.

[68] H. P. Liermann, Z. Konôpková, K. Appel, C. Prescher, A. Schropp, V. Cerantola, R. J. Husband, J. D. McHardy, M. I. McMahon, R. S. McWilliams, C. M. Pépin, J. Mainberger, M. Roeper, A. Berghäuser, H. Damker, P. Talkovski, M. Foese, N. Kujala, O. B. Ball, M. A. Baron, R. Briggs, M. Bykov, E. Bykova, J. Chantel, A. L. Coleman, H. Cynn, D. Dattelbaum, L. E. Dresselhaus-Marais, J. H. Eggert, L. Ehm, W. J. Evans, G. Fiquet, M. Frost, K. Glazyrin, A. F. Goncharov, H. Hwang, Z. Jenei, J.-Y. Kim, F. Langenhorst, Y. Lee, M. Makita, H. Marquardt, E. E. McBride, S. Merkel, G. Morard, E. F. O'Bannon, C. Otzen, E. J. Pace, A. Pelka, J. S. Pigott, V. B. Prakapenka, R. Redmer, C. Sanchez-Valle, M. Schoelmerich, S. Speziale, G. Spiekermann, B. T. Sturtevant, S. Toleikis, N. Velisavljevic, M. Wilke, C.-S. Yoo, C. Baehtz, U. Zastrau, and C. Strohm. Novel experimental setup for megahertz X-ray diffraction in a diamond anvil cell at the High Energy Density (HED) instrument of the European X-ray Free-Electron Laser (EuXFEL). *Journal of Synchrotron Radiation*, 28(3):688–706, May 2021.

[69] Marija Krstulović, Angelika D. Rosa, Nicole Biedermann, Tetsuo Irifune, and Max Wilke. Structural changes in aluminosilicate glasses up to 164GPa and the role of alkali, alkaline earth cations and alumina in the densification mechanism. *Chemical Geology*, 560:119980, January 2021.

[70] George Serghiou, Hans Josef Reichmann, Nicholas Odling, Kristina Spektor, Anna Pakhomova, Wilson A. Crichton, and Zuzana Konôpková. An Unexpected Cubic Symmetry in Group IV Alloys Prepared Using Pressure and Temperature. *Angewandte Chemie International Edition*, 60(16):9009–9014, 2021.

[71] Felix Büttner, Bastian Pfau, Marie Böttcher, Michael Schneider, Giuseppe Mercurio, Christian M. Günther, Piet Hessing, Christopher Klose, Angela Wittmann, Kathinka Gerlinger, Lisa-Marie Kern, Christian Strüber, Clemens von Korff Schmising, Josefin Fuchs, Dieter Engel, Alexandra Churikova, Siying

Huang, Daniel Suzuki, Ivan Lemesh, Mantao Huang, Lucas Caretta, David Weder, John H. Gaida, Marcel Möller, Tyler R. Harvey, Sergey Zayko, Kai Bagschik, Robert Carley, Laurent Mercadier, Justine Schlappa, Alexander Yaroslavtsev, Loïc Le Guyarder, Natalia Gerasimova, Andreas Scherz, Carsten Deiter, Rafael Gort, David Hickin, Jun Zhu, Monica Turcato, David Lomidze, Florian Erdinger, Andrea Castoldi, Stefano Maffessanti, Matteo Porro, Andrey Samartsev, Jairo Sinova, Claus Ropers, Johan H. Mentink, Bertrand Dupé, Geoffrey S. D. Beach, and Stefan Eisebitt. Observation of fluctuation-mediated picosecond nucleation of a topological phase. *Nature Materials*, 20(1):30–37, January 2021.

[72] Anatoly Shabalin. *Coherent X-ray diffraction studies of mesoscopic materials*, Universität Hamburg, Dissertation, 2015.

[73] W. Friedrich, P. Knipping, and M. Laue. Interferenzerscheinungen bei Röntgenstrahlen. *Annalen der Physik*, 346(10):971–988, 1913.

[74] Michael Eckert. Max von Laue and the discovery of X-ray diffraction in 1912. *Annalen der Physik*, 524(5):A83–A85, 2012.

[75] William Henry Bragg and William Lawrence Bragg. *The Reflection of X-rays by Crystals*. Royal Society of London, July 1913.

[76] Z.G. Pinsker. *Dynamical Scattering of X-Rays in Crystals, Springer Series in Solid-State Sciences*. Berlin, Heidelberg, 1st edition, 1978.

[77] A. Authier. *Dynamical theory of X-ray diffraction*, Oxford University Press. (2nd), 2006.

[78] Carmelo Giacovazzo, Hugo Luis Monaco, Gilberto Artioli, Davide Viterbo, Marco Milanesio, Gastone Gilli, Paola Gilli, Giuseppe Zanotti, Giovanni Ferraris, and and Michele Catti Carmelo Giacovazzo. *Fundamentals of Crystallography*. Oxford University Press, 3rd edition, June 2011.

[79] Peter Wochner, Christian Gutt, Tina Autenrieth, Thomas Demmer, Volodymyr Bugaev, Alejandro Díaz Ortiz, Agnès Duri, Federico Zontone, Gerhard Grübel, and Helmut Dosch. X-ray cross correlation analysis uncovers hidden local symmetries in disordered matter. *Proceedings of the National Academy of Sciences*, 106(28):11511–11514, July 2009.

[80] A. S. Nowick. *X-ray diffraction procedures for polycrystalline and amorphous materials*. H. P. Klug and L. E. Alexander. John Wiley and Sons,. 2(1):140–140,

1956.

[81] H. Formanek and S. Formanek. Protein crystallography by T. L. Blundell and L. N. Johnson. *Acta Crystallographica Section B: Structural Crystallography and Crystal Chemistry*, 33(8):2702–2702, August 1977.

[82] X-Ray Diffraction, Interference Basics: The Double Slit Experiment | https://www.tf.uni-kiel.de/matwis/amat/iss/kap_4/illustr/s4_2_2.html.

[83] Beam Conditioners | http://pd.chem.ucl.ac.uk/pdnn/inst2/condit.html.

[84] Hadis Morko. *Handbook of Nitride Semiconductors and Devices, Materials Properties*, Physics and Growth, Wiley. 1:1311, 2009.

[85] Michael R. Krames, Oleg B. Shchekin, Regina Mueller-Mach, Gerd O. Mueller, Ling Zhou, Gerard Harbers, and M. George Craford. Status and Future of High-Power Light-Emitting Diodes for Solid-State Lighting. *Journal of Display Technology*, 3(2):160–175, June 2007.

[86] Joerg Heber. Akasaki, Amano & Nakamura. *Nature Physics*, 10(11):791, November 2014.

[87] Fang Qian, Silvija Gradecak, Yat Li, Cheng-Yen Wen, and Charles M. Lieber. Core/multishell nanowire heterostructures as multicolor, high-efficiency light-emitting diodes. *Nano Letters*, 5(11):2287–2291, November 2005.

[88] Ruoxue Yan, Daniel Gargas, and Peidong Yang. Nanowire photonics. *Nature Photonics*, 3(10):569–576, October 2009.

[89] Chih Yen Chen, Guang Zhu, Youfan Hu, Jeng Wei Yu, Jinghui Song, Kai Yuan Cheng, Lung Han Peng, Li Jen Chou, and Zhong Lin Wang. Gallium nitride nanowire based nanogenerators and light-emitting diodes. *ACS Nano*, 6(6):5687–5692, June 2012.

[90] Jesper Wallentin, Nicklas Anttu, Damir Asoli, Maria Huffman, Ingvar Åberg, Martin H. Magnusson, Gerald Siefer, Peter Fuss-Kailuweit, Frank Dimroth, Bernd Witzigmann, H. Q. Xu, Lars Samuelson, Knut Deppert, and Magnus T. Borgström. InP Nanowire Array Solar Cells Achieving 13.8% Efficiency by Exceeding the Ray Optics Limit. *Science*, 339(6123):1057–1060, March 2013.

[91] Sanghyun Ju, Antonio Facchetti, Yi Xuan, Jun Liu, Fumiaki Ishikawa, Peide Ye, Chongwu Zhou, Tobin J. Marks, and David B. Janes. Fabrication of fully transparent nanowire transistors for transparent and flexible electronics. *Nature Nanotechnology*, 2(6):378–384, June 2007.

[92] Jean-Pierre Colinge, Chi-Woo Lee, Aryan Afzalian, Nima Dehdashti Akhavan, Ran Yan, Isabelle Ferain, Pedram Razavi, Brendan O'Neill, Alan Blake, Mary White, Anne-Marie Kelleher, Brendan McCarthy, and Richard Murphy. Nanowire transistors without junctions. *Nature Nanotechnology*, 5(3):225–229, March 2010.

[93] Neil P. Dasgupta, Jianwei Sun, Chong Liu, Sarah Brittman, Sean C. Andrews, Jongwoo Lim, Hanwei Gao, Ruoxue Yan, and Peidong Yang. 25th Anniversary Article: Semiconductor Nanowires – Synthesis, Characterization, and Applications. *Advanced Materials*, 26(14):2137–2184, 2014.

[94] Dmitry Dzhigaev. *Characterization of nanowires by coherent x-ray diffractive imaging and ptychography*, Dissertation, University of Hamburg, 2017.

[95] R. S. Wagner and W. C. Ellis. Vapor-liquid-solid mechanism of single crystal growth. *Applied Physics Letters*, 4(5):89–90, 2004.

[96] Sebastian Lehmann, Jesper Wallentin, Daniel Jacobsson, Knut Deppert, and Kimberly A. Dick. A general approach for sharp crystal phase switching in InAs, GaAs, InP, and GaP nanowires using only group V flow. *Nano Letters*, 13(9):4099–4105, September 2013.

[97] Lukas Wittenbecher, Emil Viñas Boström, Jan Vogelsang, Sebastian Lehman, Kimberly A. Dick, Claudio Verdozzi, Donatas Zigmantas, and Anders Mikkelsen. Unraveling the Ultrafast Hot Electron Dynamics in Semiconductor Nanowires. *ACS Nano*, 15(1):1133–1144, January 2021.

[98] Bernhard Mandl, Anil W. Dey, Julian Stangl, Mirco Cantoro, Lars-Erik Wernersson, Günther Bauer, Lars Samuelson, Knut Deppert, and Claes Thelander. Self-seeded, position-controlled InAs nanowire growth on Si: A growth parameter study. *Journal of Crystal Growth*, 334(1):51–56, November 2011.

[99] Jae Cheol Shin, Ari Lee, Parsian Katal Mohseni, Do Yang Kim, Lan Yu, Jae Hun Kim, Hyo Jin Kim, Won Jun Choi, Daniel Wasserman, Kyoung Jin Choi, and Xiuling Li. Wafer-scale production of uniform InAs(y)P(1-y) nanowire array on silicon for heterogeneous integration. *ACS Nano Letters*, 7(6):5463–5471, June 2013.

[100] Qian D Zhuang, Ezekiel A Anyebe, Ana M Sanchez, Mohana K Rajpalke, Tim D Veal, Alexander Zhukov, Benjamin J Robinson, Frazer Anderson, Oleg Kolosov, and Vladimir Fal'ko. Graphitic platform for self-catalysed InAs nanowires growth by molecular beam epitaxy. *Nanoscale Research Letters*,

9(1):321, June 2014.

[101] Yewu Wang, Volker Schmidt, Stephan Senz, and Ulrich Gösele. Epitaxial growth of silicon nanowires using an aluminum catalyst. *Nature Nanotechnology*, 1:186–9, December 2006.

[102] U. P. Gomes, D. Ercolani, V. Zannier, S. Battiato, E. Ubyivovk, V. Mikhailovskii, Y. Murata, S. Heun, F. Beltram, and L. Sorba. Heterogeneous nucleation of catalyst-free InAs nanowires on silicon. *Nanotechnology*, 28(6):065603, January 2017.

[103] Ramesh Kumar Kakkerla, Chih-Jen Hsiao, Deepak Anandan, Sankalp Kumar Singh, Sheng-Po Chang, Krishna P. Pande, and Edward Yi Chang. Growth and Crystal Structure Investigation of InAs/GaSb Heterostructure Nanowires on Si Substrate. *IEEE Transactions on Nanotechnology*, 17(6):1151–1158, November 2018.

[104] Structure - Zinc Blende (ZnS) | https://chem.libretexts.org, October 2013.

[105] Magnus W. Larsson, Jakob B. Wagner, Mathias Wallin, Paul Håkansson, Linus E. Fröberg, Lars Samuelson, and L. Reine Wallenberg. Strain mapping in free-standing heterostructured wurtzite InAs/InP nanowires. *Nanotechnology*, 18(1):015504, December 2006.

[106] Jianing Chen, Gabriela Conache, Mats-Erik Pistol, Struan M. Gray, Magnus T. Borgström, Hongxing Xu, H. Q. Xu, Lars Samuelson, and Ulf Håkanson. Probing strain in bent semiconductor nanowires with Raman spectroscopy. *Nano Letters*, 10(4):1280–1286, April 2010.

[107] S Jimenez-Sandoval. Micro-Raman spectroscopy: a powerful technique for materials research. *Microelectronics Journal*, 31(6):419–427, June 2000.

[108] Ingrid De Wolf, Vincent Senez, Roberto Balboni, A. Armigliato, S. Frabboni, Alessia Cedola, and S. Lagomarsino. Techniques for mechanical strain analysis in submicron structures : TEM/CBED, micro-Raman spectroscopy, *X-RAY micro-diffraction and modelling*. 70:425–435, 2003.

[109] Th Kehagias, G. P. Dimitrakopulos, P. Becker, J. Kioseoglou, F. Furtmayr, T. Koukoula, I. Häusler, A. Chernikov, S. Chatterjee, Th Karakostas, H.-M. Solowan, U. T. Schwarz, M. Eickhoff, and Ph Komninou. Nanostructure and strain in InGaN/GaN superlattices grown in GaN nanowires. *Nanotechnology*, 24(43):435702, September 2013.

[110] T. M. Smeeton, M. J. Kappers, J. S. Barnard, M. E. Vickers, and C. J. Humphreys. Electron-beam-induced strain within InGaN quantum wells: False indium "cluster" detection in the transmission electron microscope. *Applied Physics Letters*, 83(26):5419–5421, December 2003.

[111] Tanja Etzelstorfer, Martin Süess, Gustav Schiefler, Vincent Jacques, Dina Carbone, Daniel Chrastina, Giovanni Isella, Ralph Spolenak, Julian Stangl, Hans Sigg, and Ana Diaz. Scanning X-ray strain microscopy of inhomogeneously strained Ge micro-bridges. *Journal of Synchrotron Radiation*, 21(1):111–118, January 2014.

[112] A. Schropp, R. Hoppe, J. Patommel, D. Samberg, F. Seiboth, S. Stephan, G. Wellenreuther, G. Falkenberg, and C. G. Schroer. Hard x-ray scanning microscopy with coherent radiation: Beyond the resolution of conventional x-ray microscopes. *Applied Physics Letters*, 100(25):253112, June 2012.

[113] Florian Döring, A.L. Robisch, Christian Eberl, Markus Osterhoff, A Ruhlandt, Tobias Liese, F Schlenkrich, Sarah Hoffmann-Urlaub, M Bartels, Tim Salditt, and Hans-Ulrich Krebs. Sub-5 nm hard x-ray point focusing by a combined Kirkpatrick-Baez mirror and multilayer zone plate. *Optics Express*, 21(16):19311–19323, 2013.

[114] C. Mocuta, J. Stangl, K. Mundboth, T. H. Metzger, G. Bauer, I. A. Vartanyants, M. Schmidbauer, and T. Boeck. Beyond the ensemble average: X-ray microdiffraction analysis of single SiGe islands. *Physical Review B*, 77(24):245425, June 2008.

[115] D. Kriegner, J.M. Persson, T. Etzelstorfer, D. Jacobsson, J. Wallentin, J.B. Wagner, K. Deppert, M.T. Borgström, and J. Stangl. Structural investigation of GaInP nanowires using X-ray diffraction. *Thin Solid Films*, 543:100–105, September 2013.

[116] Tomaš Stankevič, Dmitry Dzhigaev, Zhaoxia Bi, Max Rose, Anatoly Shabalin, Juliane Reinhardt, Anders Mikkelsen, Lars Samuelson, Gerald Falkenberg, Ivan A. Vartanyants, and Robert Feidenhans'l. Nanofocused x-ray beams applied for mapping strain in core-shell nanowires. *X-Ray Nanoimaging: Instruments and Methods II*, 9592:26–32, 2015.

[117] Konstantinos Salonitis, John Pandremenos, John Paralikas, and George Chryssolouris. Multifunctional materials: engineering applications and processing challenges. *The International Journal of Advanced Manufacturing Technology*,

49:803–826, 2010.

[118] Jacques Curie and Pierre Curie. Développement par compression de l'électricité polaire dans les cristaux hémièdres à faces inclinées. *Bulletin de Minéralogie*, 3(4):90–93, 1880.

[119] Walter G. Cady. *Piezoelectricity: an introduction to the theory and applications of electromechanical phenomena in crystals*. International series in pure and applied physics. McGraw-Hill Book Company, Inc., New York, 1st edition, 1946.

[120] B. Jaffe, R. S. Roth, and S. Marzullo. Piezoelectric Properties of Lead Zirconate-Lead Titanate Solid-Solution Ceramics. *Journal of Applied Physics*, 25(6):809–810, June 1954.

[121] Jürgen Rödel and Jing-Feng Li. Lead-free piezoceramics: Status and perspectives. *MRS Bulletin*, 43(8):576–580, August 2018.

[122] Jing-Feng Li. *Fundamentals of Piezoelectricity, Lead-Free Piezoelectric Materials*. pages 1–18. John Wiley & Sons, Ltd, 1st edition, 2021.

[123] Standard on Piezoelectricity, Transactions on Sonics and Ultrasonics, *IEEE*, 176-1987. 1988.

[124] Robin Materlik, Christopher Künneth, and Alfred Kersch. The Origin of Ferroelectricity in Hfx Zr(1-x)O2: A Computational Investigation and a Surface Energy Model. *Journal of Applied Physics*, 117:134109, April 2015.

[125] Johannes Müller, Tim S. Böscke, Uwe Schröder, Stefan Mueller, Dennis Bräuhaus, Ulrich Böttger, Lothar Frey, and Thomas Mikolajick. Ferroelectricity in Simple Binary ZrO2 and HfO2. *Nano Letters*, 12(8):4318–4323, August 2012.

[126] Sebastian E. Reyes-Lillo, Kevin F. Garrity, and Karin M. Rabe. Antiferroelectricity in thin-film ZrO2 from first principles. *Physical Review B*, 90(14):140103, October 2014.

[127] Clemens Mart, Thomas Kämpfe, Raik Hoffmann, Sophia Eßlinger, Sven Kirbach, Kati Kühnel, Malte Czernohorsky, Lukas Eng, and Wenke Weinreich. Piezoelectric Response of Polycrystalline Silicon-Doped Hafnium Oxide Thin Films Determined by Rapid Temperature Cycles. *Advanced Electronic Materials*, 6, January 2020.

[128] Sergej Starschich and Ulrich Böttger. Doped ZrO2 for future lead free piezo-

electric devices. *Journal of Applied Physics*, 123(4):044101, January 2018.

[129] Mariana Fraga, Humber Furlan, Rodrigo Pessoa, and Marcos Massi. Wide bandgap semiconductor thin films for piezoelectric and piezoresistive MEMS sensors applied at high temperatures: An overview. *Microsystem Technologies*, 20:9–21, December 2013.

[130] Gennadiy P. Nikishkov, *Introduction to the Finite Element Method*, University of Aizu, Aizu-Wakamatsu, Japan, 2009.

[131] Ahmad Jafari, Pooyan Broumand, Mohammad Vahab, and Nasser Khalili. An extended Finite Element Method Implementation in COMSOL Multiphysics: Solid Mechanics, Finite Elements in Analysis and Design. *Elsevier*, 202:103707, 2022.

[132] Zvi Kam. Determination of Macromolecular Structure in Solution by Spatial Correlation of Scattering Fluctuations, *Macromolecules*. 10(5):927–934, 1977.

[133] R. P. Kurta, R. Dronyak, M. Altarelli, E. Weckert, and I. A. Vartanyants. Solution of the phase problem for coherent scattering from a disordered system of identical particles. *New Journal of Physics*, 15(1):013059, January 2013.

[134] I R Peake, J C Giddings, and A L Bloom. Proceedings: An abnormality of factor-VIII-related protein (FVIIIRP)–possible variants of von Willebrand's disease. *British Journal of Haematology*, 28(1):143–144, September 1974.

[135] Richard Kirian. Structure determination through correlated fluctuations in X-ray scattering. *Journal of Physics B: Atomic, Molecular and Optical Physics*, 45:223001, November 2012.

[136] Kanupriya Pande, Jeffrey J. Donatelli, Erik Malmerberg, Lutz Foucar, Christoph Bostedt, Ilme Schlichting, and Petrus H. Zwart. Ab initio structure determination from experimental fluctuation X-ray scattering data. *Proceedings of the National Academy of Sciences*, 115(46):11772–11777, November 2018.

[137] Dmitrii Lapkin. *Structural investigation of nanoparticle superlattices by advanced X-ray scattering methods*. Doctoral Thesis, Staats- und Universitätsbibliothek Hamburg Carl von Ossietzky, 2022.

[138] Dmitry Lapkin, Anatoly Shabalin, Janne-Mieke Meijer, Ruslan Kurta, Michael Sprung, Andrei V Petukhov, and Ivan A. Vartanyants. Angular X-ray cross-correlation analysis applied to the scattering data in 3D reciprocal space from a single crystal. *International Union of Crystallography*, 9(4):425–438, July

2022.

[139] Anjan P. Gantapara, Joost de Graaf, René van Roij, and Marjolein Dijkstra. Phase Diagram and Structural Diversity of a Family of Truncated Cubes: Degenerate Close-Packed Structures and Vacancy-Rich States. *Physical Review Letters*, 111(1):015501, July 2013.

[140] Ran Ni, Anjan Prasad Gantapara, Joost de Graaf, René van Roij, and Marjolein Dijkstra. Phase diagram of colloidal hard superballs: from cubes via spheres to octahedra. *Soft Matter*, 8(34):8826–8834, August 2012.